DEVELOPMENT AND APPLICATION OF GENETICALLY ENCODED BIOSENSORS FOR STUDYING COMPARTMENTALIZED SIGNALING

by
Brian Tenner

A dissertation submitted to Johns Hopkins University in conformity with the requirements for the degree of Doctor of Philosophy

Baltimore, Maryland
July, 2019

Abstract

Cell signaling is essential for all living systems to sense the environment, process information, and maintain homeostasis. Biological assemblies composed of enzymes, scaffold proteins, and chemical messengers organize signaling networks in both space and time in order to integrate and transduce diverse inputs. However, the mechanistic underpinnings of these processes in many pathways remain poorly characterized.

Genetically encoded biosensors incorporating fluorescent proteins have revolutionized our study of signaling networks by illuminating the communication and regulatory processes between important pathway components in live cells (reviewed in Chapter 1). In this dissertation, biosensors were applied to study compartmentalized signaling within the Ca^{2+}-cAMP-PKA oscillatory circuit in pancreatic beta cells (Chapter 2). Significantly, this work uncovered nanoscale spatial regulation of the circuit's phase between oscillatory Ca^{2+} and cAMP/PKA and suggests that the phase, in addition to the frequency and amplitude, can be utilized as an additional scheme for informational encoding within a signaling circuit. Measuring such compartmentalized signals can be fraught with complications due to the artificial expression of biosensors fused to proteins-of-interest. In Chapter 3, a novel platform is introduced in which genetic knock-in of a tag can be used to recruit a suite of biosensors to an endogenous protein-of-interest for compartmentalized signaling interrogation. These FluoSTEPs (Fluorescent Sensors Targeted to Endogenous Proteins) are employed to study differential cAMP signaling at a variety of important regulatory microdomains. Uncovering the dynamic interplay and coordination between several signaling components within individual cells with genetically encoded biosensors can be difficult due to finite spectral space. Thus, in Chapter 4, two families of biosensors are introduced to address this limitation: 1) FLAREs (FLuorescence Anisotropy REporters) utilize changes in polarization during homo-FRET to produce single-color, ratiometric readouts of biochemical activities and 2) single-color biosensors based on a single fluorescent protein can report sensitive changes in signaling dynamics with a reduced spectral footprint. Design and optimization of such sensors benefited from high-throughput screening for favorable mutations, and so various screening platforms are also covered here. These genetically encoded biosensors add to the ever-growing repertoire of tools researchers can employ for dissecting signaling pathways in live cells.

Primary Reader: Jin Zhang
Secondary Reader: Kalina Hristova

Acknowledgements

As will be evident in the transition from Chapter 2 to Chapter 4, my interests and passions within the laboratory and research-wise shifted from the application of biosensors to the development of new, better ones. I would like to thank, first and foremost, Jin for cultivating creativity within the lab and helping facilitate this transition for me. Her unwavering support and excellent mentorship has shaped me into a stronger scientist. I would also like to thank my committee (K. Hristova, M. Amzel, and J. Xiao) who have been there since the very beginning and have always offered invaluable input for my projects.

A special thanks are due to all the Zhang lab members that relocated with me from Johns Hopkins to University of California San Diego in 2015. This dissertation would not have been possible without the humor and inspiration of Brian Ross, the ever-helpful and electrifying Eric Greenwald, the friendship of Terri Clister, the support of Sohum Mehta, the generosity of Fabian Hertel, the helpful advice from Xin Zhou, and the comradery of Chris Booth.

I also want to thank all my family and friends, on both coasts, for their love and support. A special thanks go to: Erica Losito, Linda Joosen, Jesse Yoder, Emily Baltz & Brian Taylor, Andrew Richards, Suzanne Rohrback, The Corner, Kaisa Hanley and Alberto Carreno, Eileen Moreno, Gina Powers, Jennifer MacFarland, Valerie Sapp, Daphne Bindels, Dagan Marx, and everyone else that never stopped believing that I would make it to where I am today.

Contents

List of Figures

Chapter 1

“Optical sensors to gain mechanistic insights into signaling assemblies”

Reproduced from:

B. Tenner, S. Mehta, J. Zhang. (2016). “Optical sensors to gain mechanistic insights into signaling assemblies.” Current Opinion in Structural Biology. 203-210.

Abstract

Protein complexes play a major role in transducing information from outside the cell into instructions for growth and survival, and understanding how these complexes relay and shape intracellular signals has been a central question in signaling biology. Fluorescent proteins have proven paramount in opening windows for researchers to peer into the architecture and inner workings of signaling assemblies within the living cell and in real-time. In this review, we will provide readers with a current perspective on the development and use of genetically encoded optical probes to dissect the function of signaling complexes.

Introduction

Signaling networks are essential for cells to sense their environment and rapidly translate external information into decisions that promote growth and sustainability. Due to the complexity of the intracellular space, these networks have evolved multimolecular assemblies to facilitate signal transduction by specifically positioning enzymes and substrates for interaction [1]. Extensive biochemical characterization over the last few decades has provided researchers a glimpse into the assembly of signaling complexes and the mechanisms through which they shape signals. However, obtaining a more complete understanding of intracellular communication requires tools that are capable of capturing the spatiotemporal dynamics of these processes within individual living cells.

Recent technological advances in live-cell imaging and the landmark discovery of fluorescent proteins (FPs) have revolutionized the signaling field and led to the development of genetically encoded biosensors for interrogating signaling in the native biological context as opposed to in the test tube [2]. In addition, these tools have opened up the possibility of monitoring individual cells at the time scale at which signaling events occur, whereas bulk measurement techniques often fall short of accurately describing the cell-to-cell heterogeneity of signaling, i.e., an average response can mask important dynamics, such as oscillations and transient spiking [3]. Further adaptations of these tools over the last ten years have promoted the design of fluorescence-based biosensors that can actually provide mechanistic descriptions of signaling assemblies by measuring localized protein-protein interactions (PPIs), second messenger concentrations, and enzymatic activities [4].

In this chapter, we will briefly cover some of the optical-based tools that are currently utilized to probe multiprotein signaling complexes. The technologies covered here are not exhaustive, but will rather focus on a few important techniques and the present state of probe and sensor development.

Assembly architecture

Signaling complexes can be assembled from many different enzymes, adaptors, and scaffolds, forming a localized, information-rich protein interaction network. The components within the assembly can exist in many physiologically relevant molecular states, such as being bound to the complex, being chemically modified, or adopting a specific conformation [1]. Perturbations to the composition of an assembly, for example, by mutations, often transform signaling pathways and can cause detrimental effects such as cancer and Alzheimer's disease [5,6]. To understand the signal-shaping mechanisms of these multiprotein machines, it is important to characterize the dynamic PPIs in the local context of the living cell. Below, we outline a few technologies that have assisted researchers in dissecting the architecture of signaling complexes and highlight current developments that push the limits of measurement.

From revealing the composition of a signaling complex to measuring the dynamic changes within a signaling complex, Förster Resonance Energy Transfer (FRET) is a powerful tool for probing PPIs. FRET involves the non-radiative transfer of energy from an excited donor fluorophore to an acceptor fluorophore. This photophysical process is immediate and functions effectively in the 1-10 nm regime with an inverse $(\text{distance})^6$ dependence, making FRET a sensitive method to study interactions at the scale of macromolecules in situ (Figure 1a) [7]. Advancements in imaging/detection techniques and the discovery of spectral FP variants have led to the routine utilization of FRET in signaling research.

Many signaling interactions occur quickly and reversibly, and thus require dynamic, reversible probes. Non-covalent interactions can be effectively coupled to the distance-dependent FRET signal by directly fusing or tagging the proteins of interest to fluorescent proteins [8]. This methodology has been utilized to build signaling network models. For example, the G-protein signaling pathway comprises many PPI events, including receptor activation, G-protein dissociation, and receptor recycling; almost every ligand-induced event in this pathway has been monitored using FRET [9,10]. In addition, many of the players undergo conformational changes upon binding or unbinding, and FRET can be used to the measure these changes in an intramolecular fashion. For example, ligand-inducible changes of GPCRs can be monitored by inserting CFP into an intracellular loop and placing YFP at the C-terminus [11]. The G-protein pathway has also benefitted from BRET, another resonance energy transfer-based method that utilizes a bioluminescent luciferase as the energy donor, obviating the need for potentially damaging exogenous illumination and leading to less photobleaching and lower background [12].

The finite range of the visible spectrum and the broad excitation and emission spectra of FPs can make FRET a spectrally expensive technique [13]. Fortunately, alternative single-color methods can also be employed. The EGF receptor is known to dimerize and oligomerize upon stimulation, but only recently has a method for monitoring real-time changes in multimerization been reported [14]. This technique, known as homo-FRET, involves FRET between identical fluorophores and can be quantified by measuring the polarization of emitted light at a single wavelength relative to the excitation light [15,16]. Homo-FRET has been successfully applied to measure receptor clustering by labeling the EGF receptor with a single, monomeric GFP and measuring the loss of fluorescence anisotropy [17]. Live-cell imaging using this single-color technique led the authors to conclude that EGFR dimerization is the result of receptor activation instead of the converse [14].

Signaling complexes typically contain several physiologically important PPIs that are also incredibly dynamic. To monitor multiple interactions within a complex simultaneously, researchers are extending hetero-FRET for use with multiple donors and acceptors. For example, T-cell activation and subsequent cytoskeletal rearrangement is initiated by a multiprotein assembly comprised of the GEF Vav1 and adaptor proteins Nck and SLP-76 [18]. Immunoblotting revealed the identities of the key components, but the specific PPIs and the dynamics governing complex formation remained elusive. Utilizing the distance dependence of

FRET to monitor extremely local interactions in real-time, Pauker *et al.* fused three spectrally distinct FPs to the three components [18]. In order to detect all interactions after T-cell activation, an imaging scheme was needed to subtract spectral bleed-through and account for indirect FRET through an intermediate acceptor/donor. This study demonstrated that Nck and Vav1 exist as a constitutive heterodimer and that activation triggers the binding of SLP-76 to Nck on the timescale of seconds. This powerful multi-color FRET imaging approach to monitor many interactions simultaneously has been proposed to work with *N* spectrally distinct FPs, provided the appropriate corrections and controls are applied [19,20].

Despite its sensitivity to small changes in distances, FRET can be limited by poor signal-to-noise ratios and the requirement that a large subset of FPs must associate to produce a detectable signal [21,22]. These restrictions tend to hamper the study of very weak/transient and/or rare interactions [23,24]. For example, the binding of effectors to tyrosine kinases via SH3 domains regulates many important cell processes; however, these interactions tend to be short-lived, making FRET a less-than-optimal detection method [23,24]. An alternative technique involves the creation of a fluorescent signal when two proteins are in close proximity. By splitting a fluorescent protein into two non-fluorescent fragments and fusing each to an SH3 domain and a binding effector, heterodimerization can be measured and imaged by the reconstitution of the FP and the gain of fluorescence (Figure 1b) [27,28,29]. Although the irreversibility of this process and the time required for fluorophore maturation (minutes to potentially hours) prevent detailed dynamic measurements, bimolecular fluorescence complementation (BiFC) is well-suited for visualizing weak interactions within the cell [29]. Multiple BiFC-capable FP variants are also available and have been successfully utilized to image many PPIs, including homo- and hetero-dimers of the adenosine and dopamine receptors simultaneously [30].

Increasing evidence suggests that signaling assemblies are spatially organized at the nanometer scale; however, the spatial resolution of the above methods is limited by the diffraction of light (~250nm) [31,32,33]. In order to map PPIs at a resolution commensurate to their molecular scale, BiFC has been extended to incorporate photo-activatable FPs for super-resolution imaging. For example, the GTPase Ras has been shown to exist in functionally-important 'nanoclusters,' but the organization of Ras-binding effectors, such as Raf, is poorly understood [34]. Recently, a BiFC-compatible split version of photo-activatable mCherry was generated, and each end was fused to either Ras or Raf [35]. Both standard Photo-activated Localization Microscopy (PALM) imaging and single-particle tracking were used to map the clustered heterodimers and their collective motion. However, the inherent tradeoff between spatial and temporal resolution prohibited the extraction of meaningful dynamic information using BiFC-PALM. A recently reported super-resolution BiFC technique sought to strike a balance and permit live-cell detection of PPIs. Utilizing a split photoblinking Venus, the functionally-relevant association between the calcium store sensor Stim1 and the store-operated calcium channel Orai1 was mapped using reconstituted fluorescence-based stochastic optical fluctuation imaging (refSOFI) [36].

In certain applications, the only pertinent information for researchers is the inclusion or absence of specific effectors within an assembly. The high signal-to-noise ratio of BiFC thus permits cellular screening to probe assembly architecture [37]. For example, the important regulatory kinase PKB/Akt functions in cell growth, proliferation, and apoptosis; however, not all of the bound effectors of PKB have been characterized [38]. In a first-of-its-kind experiment, a split-GFP screen to identify novel effectors of PKB was performed by fusing one GFP fragment to a cDNA library of ‘prey’ proteins, and fusing the other fragment to PKB. By screening thousands of ‘prey’ proteins, researchers found one, Ft1, that binds to and promotes the association of PKB with PDK1 [39]. Due to the involvement of PPIs in many diseases, there has also been a large push to develop high-throughput assays for drug development. A recently described high-content screen to find inhibitors of the activity-dependent dimerization of an HIV-1 accessory factor using split YFP identified several hit compounds [40]. Improvements in BiFC for screening continue and include a tripartite fluorescence complementation assay to both study ternary complexes and reduce background complementation, as well as a split near-infrared FP to allow deep-tissue detection [41,42,43].

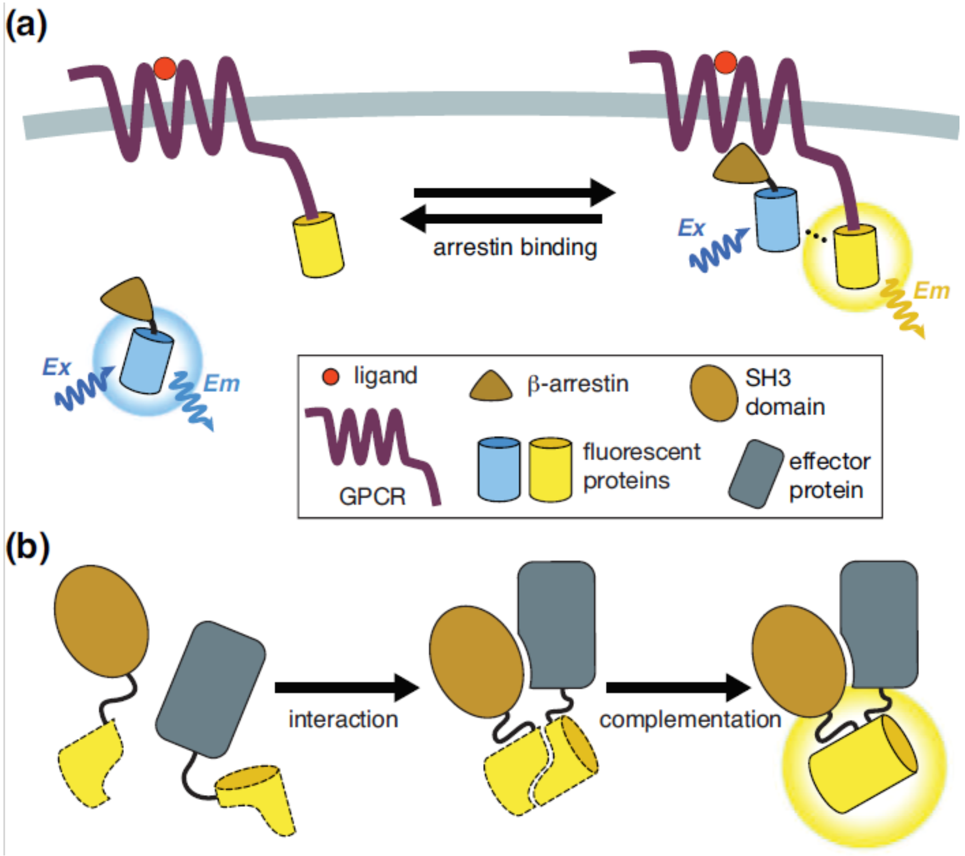

Figure 1.1 Assembly architecture

A signaling complex's internal architecture can be probed by tagging components with fluorescent proteins (FPs). As schematically shown in **(a)**, two interacting proteins, such as a GPCR and β-arrestin, are tagged with FPs capable of FRET. BiFC can also be utilized to detect PPIs, as shown in **(b)**. Two nonfluorescent FP fragments are fused to an interacting protein pair, such as an SH3 domain and an effector, and complex formation triggers the reconstitution of the fluorescent signal.

Assembly-based signaling functions

Many signaling networks rely on the formation of signalosomes, kinetically-distinct nanodomains comprised of key signaling players and effectors, in order to ‘reshape,’ or modify, downstream dynamics and optimize specific enzymatic reactions [1]. In the previous section, we looked at methods to dissect the components and interactions within an assembly. In this section, we will focus on methods, primarily using biosensors, to study the mechanisms by which signalosomes regulate signaling pathways.

Genetically encoded biosensors

Genetically encoded biosensors have become a valuable tool in allowing researchers to measure the spatiotemporal dynamics of intracellular signals within living cells. Their strength lies in their ability to specifically monitor changes in biochemical activities in real-time and with minimal invasiveness to the cell [44,45]. Biosensors generally comprise two parts: a sensing component and a reporting component [46,47]. The sensing component is responsible for detecting the relevant biochemical change through either a binding/unbinding event or protein modification, leading to a conformational change. The reporting component translates the conformational change into a detectable signal, most often via fluorescence or bioluminescence. For example, the genetically encoded calcium sensor Cameleon utilizes a calcium-dependent conformational switch composed of calmodulin and a fragment of myosin light-chain kinase sandwiched between a CFP/YFP FRET pair (Figure 2a) [48]. This same sensing unit has also been used to generate a collection of high-contrast, single-color probes that have gained in popularity (Figure 2b) [49,50]. In addition, an entire suite of kinase activity biosensors have been engineered by fusing a kinase-specific substrate domain to a phosphoaminoacid binding domain and flanking this switch between a FRET pair (Figure 2c) [51]. Phosphorylation of the substrate domain triggers a conformational change that induces a FRET change.

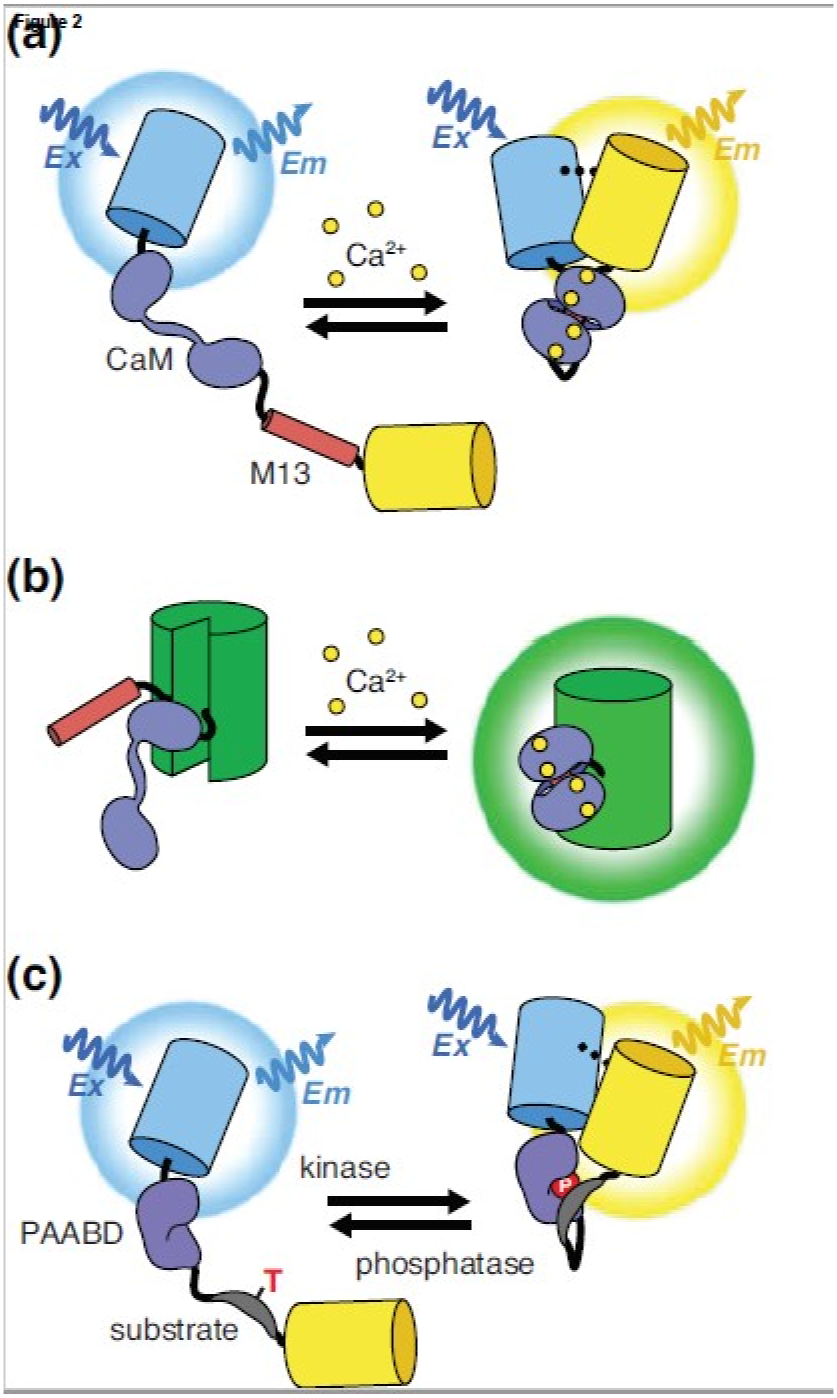

Figure 1.2 Genetically encoded biosensors

FP-based, genetically encoded biosensors are used to measure changes in signaling activities and concentrations. In **(a)**, the FRET-based calcium reporter Cameleon works by binding calcium via a calmodulin domain (CaM) and triggering binding to a domain derived from myosin light chain kinase (M13). This conformational change then elicits FRET by bringing two fused FPs into proximity. As shown in **(b)**, a suite a single-color calcium reporters, known as GCaMPs, have been developed that utilize the same CaM and M13 domains but fused to different parts of a circularly-permuted GFP. Calcium binding modulates the GFP's fluorophore, leading to increased fluorescent emission. Kinase activity can also be sensed using similar design principles as Cameleon, as seen in **(c)**. The sensing unit is comprised of a kinase-specific substrate domain that, once phosphorylated, binds to a general phosphoaminoacid binding domain (PAABD), and triggers a change in FRET.

Biosensors to study signalosome functions

To directly probe localized signaling within a signalosome, biosensors are frequently fused to a component of the multiprotein complex. Many signaling networks include scaffold and/or adaptor proteins that organize PPIs within an assembly, and biosensors have helped uncover a set of design principles complexes utilize to modify signal behavior. For example, fusing a FRET-based reporter for PKA activity (AKAR) to a class of A-kinase anchoring proteins (AKAPs) revealed accelerated activity kinetics ($t_{1/2} \approx 2s$, representing approx.. two orders of magnitude difference) and increased activity amplitude upon PKA stimulation, demonstrating that scaffolds can create kinetically distinct nanodomains (Figure 3) [52,53]. Furthermore, a recent AKAP-fused biosensor study revealed that the activity of AKAP-bound protein kinase C (PKC) is not only accelerated and amplified but is also 'insulated' from competitive inhibitors, as compared with general PKC activity at the plasma membrane. AKAPs and other scaffold proteins have also been shown to interact with many additional signaling proteins, such as adenylyl cyclases, phosphodiesterases (PDEs), and phosphatases, and can increase the specificity of certain signals [53]. For example, deletion of the PDE-binding domain in a particular AKAP was shown to reshape the stimulated PKA activity from a transient response into a more sustained response [52]. Biosensors are indispensable tools in dissecting the mechanisms that complexes use to modify intracellular signaling and precisely control the spatiotemporal dynamics of signaling cascades.

Many groups are continuously pushing the boundaries of genetically encoded biosensor design. Due to their reliance on fluorescence or bioluminescence, the challenges facing biosensors are similar to the limitations of tools for probing assembly architecture, namely, limits of spectral space and signal intensity. As mentioned previously, a set of new near-IR FPs have been optimized and shown to be suitable as FRET acceptors for *in vivo* reporting [54,55]. Despite finite spectral space, other groups have pushed the limits of multiplexing by co-expressing many biosensors and using innovative multi-dimensional unmixing methods [56]. The use of single-color biosensors frees much of the visible spectrum but often at the cost of losing a ratiometric measurement. However, a new class of biosensors utilizing homo-FRET permits a single-color, ratiometric readout by measuring changes in the steady-state fluorescence anisotropy [57]. Bottlenecks for biosensor development typically reside in the initial design and optimization stages of a new reporter; however, many groups have turned to higher-throughput screening procedures to rapidly test thousands of sensor/FP variants and evolve these mutants into better sensors. Lysate and bacterial colony screens, as well as microfluidic-based approaches, are becoming a mainstay in the development pipeline, resulting in probes with increased dynamic range and enhanced sensitivity [58,59].

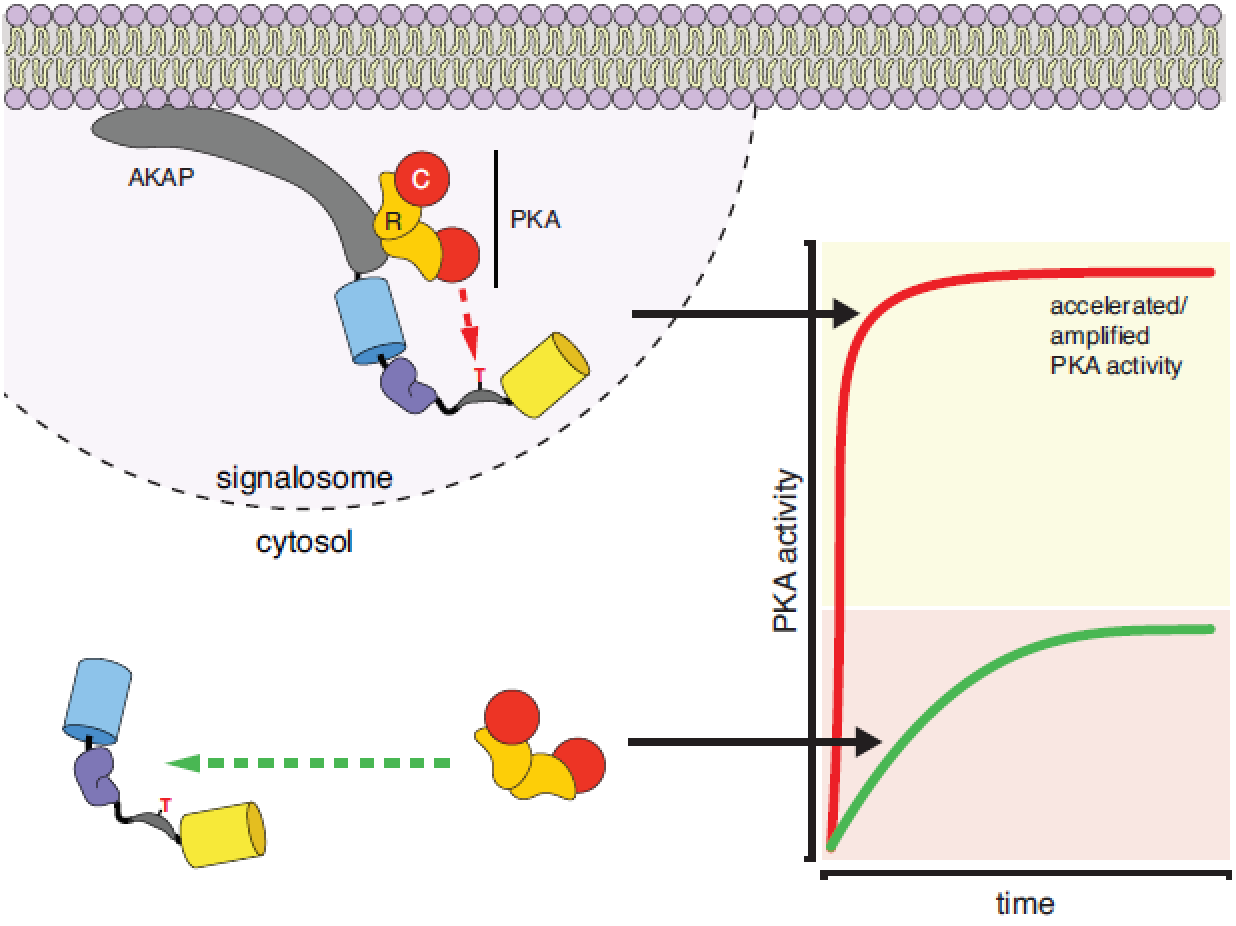

Figure 1.3 Macromolecular assemblies tune signaling
Signaling complexes tend to fundamentally alter dynamics within a signalosome. Many important signaling enzymes, such as the cAMP dependent kinase PKA, are localized throughout the cell by interacting with scaffold proteins as well as with a variety of additional effectors. Genetically encoded biosensors can measure signaling dynamics both within these signalosomes and in the cytosol. In the case of PKA, it has been shown that stimulated PKA activity is both accelerated and amplified within a PKA anchoring protein (AKAP)-centric signalosome, as compared to outside this complex.

Conclusions and future perspectives

Although far from exhaustive, this review highlights a few optical methods for probing signaling assemblies. From monitoring PPIs to interrogating the functional roles of multiprotein complexes, genetically encoded tools allow researchers to measure the spatiotemporal signatures of specific signaling networks in living cells and tissues.

Despite the high sensitivity and specificity of biosensors, the ability to report biological changes is sometimes hampered by overexpression, and thus requires a number of control experiments. Stably expressing cell lines and/or endogenously-fused sensors could alleviate such concerns. Recent progress in employing CRISPR/Cas9 for gene knockin has spurred interest in the development of endogenously expressed sensors for PPIs and activity [60].

The boundaries for attaining higher-resolution maps of interactions and activities within the cell are constantly being pushed. As mentioned previously, new methods such as BiFC-PALM and refSOFI allow researchers to image PPIs below the diffraction limit. In addition, the heterogeneity in the composition and mechanistic function of multiprotein assemblies suggests the need to study complexes at the single-molecule level instead of adopting ensemble approaches. Newer techniques such as single-molecule pull-down (SiMPull) provide a platform for extracting individual protein complexes from cells and tissues for single-molecule investigation [61]. The advent of brighter organic fluorophores and protein-tagging systems such as SNAP and Halo could also offer the possibility to utilize single-molecule FRET to directly probe individual signaling complexes [62]. In addition to improvements in spatial resolution and single-molecule detection, progress in attaining higher temporal resolution for biosensors have afforded researchers the ability to measure extremely rapid signals such as calcium spikes and action potentials with millisecond to submillisecond accuracy [63,64].

Fluorescence and bioluminescence-based tools for studying macromolecular complexes and signalosomes have contributed greatly to our understanding of intracellular signaling. Persistent innovation, including better fluorophores and robust tool design, will continue to allow researchers to design comprehensive and detailed experiments to probe the spatiotemporal dynamics of assembly-based signaling.

References

1. Cebecauer M, Spitaler M, Sergé A, Magee AI: **Signalling complexes and clusters: functional advantages and methodological hurdles.** *J. Cell Sci.* 2010, **123**:309–20.
2. Dean KM, Palmer AE: **Advances in fluorescence labeling strategies for dynamic cellular imaging.** *Nat. Chem. Biol.* 2014, **10**:512–23.
3. Altschuler SJ, Wu LF: **Cellular Heterogeneity: Do Differences Make a Difference?** *Cell* 2010, **141**:559–563.
4. DiPilato LM, Zhang J: **Fluorescent protein-based biosensors: resolving spatiotemporal dynamics of signaling**. *Curr. Opin. Chem. Biol.* 2010, **14**:37–42.
5. Cheng S, Li Y, Yang Y, Feng D, Yang L, Ma Q, Zheng S, Meng R, Wang S, Wang S, et al.: **Breast cancer-derived K172N, D301V mutations abolish Na+/H + exchanger regulatory factor 1 inhibition of platelet-derived growth factor receptor signaling**. *FEBS Lett.* 2013, **587**:3289–3295.
6. Selkoe DJ: **Cell biology of protein misfolding: The examples of Alzheimer’s and Parkinson's diseases**. *Nat. Cell Biol.* 2004, **6**:1054–1061.
7. Stryer L, Haugland RP: **Energy transfer: a spectroscopic ruler.** *Proc. Natl. Acad. Sci. U. S. A.* 1967, **58**:719–726.
8. Tsien RY: **The Green Fluorescent Protein.** *Proteins* 1998, **67**:509–44.
9. Clister T, Mehta S, Zhang J: **Single-cell analysis of G-protein signal transduction**. *J. Biol. Chem.* 2015, **290**:6681–6688.
10. Lohse MJ, Nuber S, Hoffmann C: **Fluorescence / Bioluminescence Resonance Energy Transfer Techniques to Study G-Protein-Coupled Receptor Activation and Signaling**. *Pharmacol. Rev.* 2012, **64**:299–336.
11. Vilardaga J-P, Bünemann M, Krasel C, Castro M, Lohse MJ: **Measurement of the millisecond activation switch of G protein-coupled receptors in living cells.** *Nat. Biotechnol.* 2003, **21**:807–812.
12. Salahpour A, Espinoza S, Masri B, Lam V, Barak LS, Gainetdinov RR: **BRET biosensors to study GPCR biology, pharmacology, and signal transduction**. *Front. Endocrinol. (Lausanne).* 2012, **3**:1–9.
13. Chen H, Puhl HL, Koushik S V, Vogel SS, Ikeda SR: **Measurement of FRET efficiency and ratio of donor to acceptor concentration in living cells.** *Biophys. J.* 2006, **91**:L39–41.
14. Hofman EG, Bader AN, Voortman J, Van Den Heuvel DJ, Sigismund S, Verkleij AJ, Gerritsen HC, Van Bergen en Henegouwen PMP: **Ligand-induced EGF receptor oligomerization is kinase-dependent and enhances internalization**. *J. Biol. Chem.*

2010, **285**:39481–39489.

15. Bader AN, Hofman EG, Voortman J, Van Bergen En Henegouwen PMP, Gerritsen HC: **Homo-FRET imaging enables quantification of protein cluster sizes with subcellular resolution.** *Biophys. J.* 2009, **97**:2613–2622.

16. Bader AN, Hoetzl S, Hofman EG, Voortman J, Van Bergen En Henegouwen PMP, Van Meer G, Gerritsen HC: **Homo-FRET imaging as a tool to quantify protein and lipid clustering**. *ChemPhysChem* 2011, **12**:475–483.

17. De Heus C, Kagie N, Heukers R, Van Bergen En Henegouwen PMP, Gerritsen HC: **Analysis of EGF Receptor Oligomerization by Homo-FRET.** Elsevier Inc.; 2013.

18. Pauker MH, Hassan N, Noy E, Reicher B, Barda-Saad M: **Studying the Dynamics of SLP-76, Nck, and Vav1 Multimolecular Complex Formation in Live Human Cells with Triple-Color FRET**. *Sci. Signal.* 2012, **5**:rs3–rs3.

19. Hoppe AD, Scott BL, Welliver TP, Straight SW, Swanson JA: **N-Way FRET Microscopy of Multiple Protein-Protein Interactions in Live Cells**. *PLoS One* 2013, **8**.

20. Sun Y, Wallrabe H, Booker CF, Day RN, Periasamy A: **Three-color spectral FRET microscopy localizes three interacting proteins in living cells**. *Biophys. J.* 2010, **99**:1274–1283.

21. Woehler A, Wlodarczyk J, Neher E: **Signal/noise analysis of FRET-based sensors.** *Biophys. J.* 2010, **99**:2344–2354.

22. Berney C, Danuser G: **FRET or no FRET: A quantitative comparison.** *Biophys. J.* 2003, **84**:3992–4010.

23. Piston DWDW, Kremers G-JGJ: **Fluorescent protein FRET: the good, the bad and the ugly.** *Trends Biochem. Sci.* 2007, **32**:407–414.

24. Grünberg R, Burnier J V, Ferrar T, Beltran-Sastre V, Stricher F, van der Sloot AM, Garcia-Olivas R, Mallabiabarrena A, Sanjuan X, Zimmermann T, et al.: **Engineering of weak helper interactions for high-efficiency FRET probes.** *Nat. Methods* 2013, **10**:1021–7.

25. Barilá D, Superti-Furga G: **An intramolecular SH3-domain interaction regulates c-Abl activity.** *Nat. Genet.* 1998, **18**:280–282.

26. Morell M, Espargaró A, Avilés FX, Ventura S: **Detection of transient protein-protein interactions by bimolecular fluorescence complementation: The Abl-SH3 case**. *Proteomics* 2007, **7**:1023–1036.

27. Michnick SW: **Detection of Protein-Protein Interactions by Protein Fragment Complementation Strategies.** *Methods Enzymol.* 2015, **4**:615–624.

28. Kerppola TK: **Design and implementation of bimolecular fluorescence complementation (BiFC) assays for the visualization of protein interactions in living**

cells. *Nat. Protoc.* 2006, **1**:1278–1286.

29. Kodama Y, Hu CD: **Bimolecular fluorescence complementation (BiFC): A 5-year update and future perspectives**. *Biotechniques* 2012, **53**:285–298.

30. Vidi P, Chemel BR, Hu C, Watts VJ: **Ligand-Dependent Oligomerization of Dopamine D 2 and Adenosine A 2A Receptors in Living Neuronal Cells**. *Mol. Pharmacol.* 2008, **74**:544–551.

31. Hancock JF, Parton RG: **Ras plasma membrane signalling platforms.** *Biochem. J.* 2005, **389**:1–11.

32. Kholodenko BN, Hancock JF, Kolch W: **Signalling ballet in space and time.** *Nat. Rev. Mol. Cell Biol.* 2010, **11**:414–426.

33. Cambi A, Lidke DS: **Nanoscale membrane organization: Where biochemistry meets advanced microscopy**. *ACS Chem. Biol.* 2012, **7**:139–149.

34. Harding A, Hancock JF: **Ras nanoclusters: Combining digital and analog signaling**. *Cell Cycle* 2008, **7**:127–134.

35. Nickerson A, Huang T, Lin LJ, Nan X: **Photoactivated localization microscopy with Bimolecular Fluorescence Complementation (BiFC-PALM) for nanoscale imaging of protein-protein interactions in cells. *PLoS One* 2014, **9**. The authors successfully split a photoactivatable FP and used the system to map fixed PPIs below the spatial resolution of traditional imaging methods.

*36. Hertel F, Mo GCH, Duwe S, Dedecker P, Zhang J: **RefSOFI for Mapping Nanoscale Organization of Protein-Protein Interactions in Living Cells**. *Cell Rep.* 2016, **14**:390–400. The authors utilized a BiFC approach and SOFI analysis to obtain a super-resolved map of PPIs in living cells.

37. Miller KE, Kim Y, Huh WK, Park HO: **Bimolecular Fluorescence Complementation (BiFC) Analysis: Advances and Recent Applications for Genome-Wide Interaction Studies**. *J. Mol. Biol.* 2015, **427**:2039–2055.

38. Manning BD, Cantley LC: **AKT/PKB Signaling: Navigating Downstream**. *Cell* 2007, **129**:1261–1274.

39. Remy I, Michnick SW: **Regulation of apoptosis by the Ft1 protein, a new modulator of protein kinase B/Akt.** *Mol. Cell. Biol.* 2004, **24**:1493–504.

40. Poe JA, Vollmer L, Vogt A, Smithgall TE: **Development and validation of a high-content bimolecular fluorescence complementation assay for small-molecule inhibitors of HIV-1 Nef dimerization.** *J. Biomol. Screen.* 2014, **19**:556–65.

*41. Cabantous S, Nguyen HB, Pedelacq J-D, Koraïchi F, Chaudhary A, Ganguly K, Lockard MA, Favre G, Terwilliger TC, Waldo GS: **A new protein-protein interaction sensor based on tripartite split-GFP association.** *Sci. Rep.* 2013, **3**:2854. By splitting GFP into three non-fluorescent fragments, the authors were able to decrease non-specific reconstitution and monitor the interaction between three proteins.

42. Kerppola TK: **Multicolor bimolecular fluorescence complementation (BiFC) analysis of protein interactions with alternative partners**. *Cold Spring Harb. Protoc.* 2013, **2013**:798–803.

*43. Filonov GS, Verkhusha V V.: **A near-infrared bifc reporter for in vivo imaging of protein-protein interactions**. *Chem. Biol.* 2013, **20**:1078–1086. The authors were able to split a near-infrared FP from bacteria and use the probe to detect PPIs in deep tissue where other wavelengths of light cannot reach.

44. VanEngelenburg SB, Palmer AE: **Fluorescent biosensors of protein function**. *Curr. Opin. Chem. Biol.* 2008, **12**:60–65.

45. Herbst KJ, Ni Q, Zhang J: **Dynamic visualization of signal transduction in living cells: From second messengers to kinases**. *IUBMB Life* 2009, **61**:902–908.

46. Newman RH, Fosbrink MD, Zhang J: **Genetically-encodable Fluorescent Biosensors for Tracking Signalling Dynamics in Livivng Cells**. *Chem Rev.* 2011, **111**:3614–3666.

47. Mehta S, Zhang J: **Reporting from the field: genetically encoded fluorescent reporters uncover signaling dynamics in living biological systems.** *Annu. Rev. Biochem.* 2011, **80**:375–401.

48. Miyawaki a, Llopis J, Heim R, McCaffery JM, Adams J a, Ikura M, Tsien RY: **Fluorescent indicators for Ca2+ based on green fluorescent proteins and calmodulin.** *Nature* 1997, **388**:882–887.

49. Tian L, Hires SA, Mao T, Huber D, Chiappe ME, Chalasani SH, Petreanu L, Akerboom J, McKinney SA, Schreiter ER, et al.: **Imaging neural activity in worms, flies and mice with improved GCaMP calcium indicators.** *Nat. Methods* 2009, **6**:875–881.

50. Akerboom J, Carreras Calderón N, Tian L, Wabnig S, Prigge M, Tolö J, Gordus A, Orger MB, Severi KE, Macklin JJ, et al.: **Genetically encoded calcium indicators for multi-color neural activity imaging and combination with optogenetics. *Front. Mol. Neurosci.* 2013, **6**:2. The authors extended the color palette of single-color calcium reporters based on the GCaMP design by making blue, yellow, and red variants.

51. Zhang J, Ma Y, Taylor SS, Tsien RY: **Genetically encoded reporters of protein kinase A activity reveal impact of substrate tethering.** *Proc. Natl. Acad. Sci. U. S. A.* 2001, **98**:14997–15002.

*52. Koçer SS, Wang H-Y, Malbon CC: **“Shaping” of cell signaling via AKAP-tethered PDE4D: Probing with AKAR2-AKAP5 biosensor.** *J. Mol. Signal.* 2012, **7**:4. By fusing the PKA activity sensor AKAR to a PKA anchoring protein, the authors demonstrated that PKA signaling around the protein is both accelerated and amplified.

*53. Greenwald EC, M. Redden J, Dodge-Kafka KL, Saucerman JJ: **Scaffold state switching amplifies, accelerates, and insulates protein kinase c signaling**. *J. Biol. Chem.* 2014, **289**:2353–2360. The authors determined that scaffolded PKC "insulates" PKC from certain competitive inhibitors using a fused biosensor.

*54. Zlobovskaya OA, Sarkisyan KS, Lukyanov KA: **Infrared Fluorescent Protein iRFP as an Acceptor for Forster Resonance Energy Transfer.** *Bioorg. Khim.* 2015, **41**:299–304. An infrared FP was paired with far-red FPs in order to measure FRET in tissues and multiplex with other FRET-based sensors.

55. Zlobovskaya OA, Sergeeva TF, Shirmanova M V., Dudenkova V V., Sharonov G V., Zagaynova E V., Lukyanov KA: **Genetically encoded far-red fluorescent sensors for caspase-3 activity**. *Biotechniques* 2016, **60**:62–68.

56. Woehler A: **Simultaneous Quantitative Live Cell Imaging of Multiple FRET-Based Biosensors**. *PLoS One* 2013, **8**.

57. Cameron WD, Bui C V, Hutchinson A, Loppnau P, Gräslund S, Rocheleau J V: **Apollo-NADP+: a spectrally tunable family of genetically encoded sensors for NADP+.** *Nat. Methods* 2016, **13**:352–358.

*58. Belal ASF, Sell BR, Hoi H, Davidson MW, Campbell RE: **Optimization of a genetically encoded biosensor for cyclin B1-cyclin dependent kinase 1.** *Mol. Biosyst.* 2014, **10**:191–5. By simultaneously expressing biosensors and an upstream activator for the biosensor within E.coli colonies, the authors were able to rapidly optimize the biosensor's dynamic range 4.5 fold.

*59. Davis LML, Lubbeck JLJ, Dean KKM, Palmer AE, Jimenez R: **Microfluidic cell sorter for use in developing red fluorescent proteins with improved photostability**. *Lab Chip* 2013, **13**:2320–2327. The authors built a microfluidic device that interfaces with a fluorescence microscope in order to quickly measure the dark-state conversion of many FP variants and sort these variants for further analysis.

*60. Ratz M, Testa I, Hell SW, Jakobs S: **CRISPR/Cas9-mediated endogenous protein tagging for RESOLFT super-resolution microscopy of living human cells.** *Sci. Rep.* 2015, **5**:9592. By using the CRISPR/Cas9 for knock-ins, the authors successfully tagged many endogenous proteins with reversible switching EGFP for superresolution imaging.

61. Jain A, Liu R, Xiang YK, Ha T: **Single-molecule pull-down for studying protein interactions**. *Nat. Protoc.* 2012, **7**:445–452.

62. Ishitsuka Y, Azadfar N, Kobitski AY, Nienhaus K, Johnsson N, Nienhaus GU: **Evaluation of genetically encoded chemical tags as orthogonal fluorophore labeling tools for single-molecule fret applications**. *J. Phys. Chem. B* 2015, **119**:6611–6619.

*63. Chen T-W, Wardill TJ, Sun Y, Pulver SR, Renninger SL, Baohan A, Schreiter ER, Kerr RA, Orger MB, Jayaraman V, et al.: **Ultrasensitive fluorescent proteins for imaging neuronal activity.** *Nature* 2013, **499**:295–300. The authors optimized the single-color calcium reporter GCaMP in order to respond faster to measure transient calcium spikes in neurons.

*64. St-Pierre F, Marshall JD, Yang Y, Gong Y, Schnitzer MJ, Lin MZ: **High-fidelity optical**

reporting of neuronal electrical activity with an ultrafast fluorescent voltage sensor. *Nat. Neurosci.* 2014, **17**:884–9. The authors created a single-color voltage sensor that is sensitive and responds quickly in order to detect individual action potentials.

Chapter 2

"Spatially compartmentalized phase regulation in the Ca^{2+}-cAMP-PKA oscillatory circuit"

Parts of this chapter will appear in:

B. Tenner, M. Getz, B. Ross, Y. Zhong, D. Ohadi, S. Mehta, P. Rangamani, J. Zhang, Spatially compartmentalized phase regulation in an oscillatory, signaling circuit. *In preparation for submission*

Abstract

Signaling networks are spatiotemporally organized in order to sense diverse inputs, process information, and carry out specific tasks. In pancreatic beta cells, calcium, cyclic adenosine monophosphate (cAMP), and Protein Kinase A (PKA) exist in an oscillatory circuit characterized by a high degree of feedback, and this circuit is instrumental in mediating and potentiating pulsatile insulin secretion. Here we describe a novel mode of regulation within this circuit involving the spatial compartmentalization of the relative phase between cAMP, PKA, and calcium. We show that nanodomain clustering of calcium-dependent adenylyl cyclases drives oscillations of local cAMP levels within the membrane nanodomain to be precisely in phase with calcium oscillations, whereas a shifted balance towards calcium-dependent phosphodiesterases allows out of phase oscillations to occur within the general plasma membrane, providing a striking example and novel mechanism of cAMP compartmentation. Disruption of this precise in-phase relationship leads to irregular calcium oscillations, suggesting that the relative phase within an oscillatory circuit can encode specific functional information. This example of a signaling nanodomain utilized for localized tuning of an oscillatory circuit has broad implications for the spatiotemporal coordination of many biological networks.

Introduction

Cyclic adenosine monophosphate (cAMP) and Ca^{2+} act as essential second messengers in almost every cell type and regulate many functional pathways within a cell, such as hormonal signal transduction, metabolism, and secretion (Sassone-Corsi 2012; Clapham 2007). In some cell types, like neurons, cardiomyocytes, and pancreatic beta cells, these messengers' concentrations oscillate intracellularly (Dupont et al. 2011; Dyachok et al. 2006.), and the oscillations encode dynamic signaling information (eg. signal strength, duration, target diversity) into parameters such as frequency and amplitude (Berridge et al. 1998; De Pitta et al. 2008). In beta cells, Ca^{2+}, cAMP, and the cAMP dependent kinase, Protein Kinase A (PKA), constitute a highly-coordinated oscillatory circuit with key components instrumental in integrating different signals to regulate diverse functions including insulin secretion (Ni et al. 2011; Draznin 1988). Although much attention has been directed towards understanding the temporal control of key players within this circuit in the beta cell, the spatial organization of this oscillatory circuit remains poorly characterized.

While Ca^{2+} is transported from one location to another (eg. extracellular to intracellular, internal stores to cytoplasm, or vice versa), cAMP is synthesized from ATP by adenylyl cyclases (ACs) and degraded into AMP by phosphodiesterases (PDEs) throughout the cell (Hanoune et al. 2001; Bender et al. 2006). cAMP signaling, due to its potency, target diversity, and functional specificity, is spatiotemporally controlled by compartmentalization of ACs and PDEs via macromolecular interactions and organelle localization (Calebiro et al. 2014). In the beta cell, the plasma membrane (PM)-localized scaffold protein AKAP79 (AKAP150 rodent orthologue) associates with various regulators of cAMP, as well as with Ca^{2+} channels, PKA, and secretory machinery, and global knock-out correlates with impaired Ca^{2+} influx, defective glucose-stimulated insulin secretion (GSIS), and reduced cAMP fluctuations (Hinke et al. 2012).

In this study, we investigated the spatiotemporal regulation of the Ca^{2+}-cAMP-PKA oscillatory circuit within the signaling microdomain assembled by AKAP79/150 in MIN6 beta cells. We found that the relative, oscillatory phase between cAMP/PKA and Ca^{2+} is shifted in the immediate vicinity of the AKAP79/150 scaffold, compared to the general plasma membrane compartment. We also examined the nanoscale organization of key circuit regulators at the plasma membrane and probed the spatial regulation and functional consequences of the phase relationship.

Results

The phase of oscillatory cAMP relative to Ca^{2+} is compartmentalized

AKAP79/150 organizes a macromolecular complex with binding partners that include PKA, voltage-gated Ca^{2+} channel $Ca_V1.2$, Protein Kinase C (PKC), Ca^{2+}/calmodulin-dependent protein phosphatase calcineurin, Ca^{2+}-regulated ACs, AMPA receptors, and many others (Gold et al. 2011). Due to the extensive, multivalent nature of AKAP79/150 and the functional impairment of GSIS in beta cells upon knock-out (Hinke et al. 2012), we hypothesized that the AKAP79/150 scaffold might play a role in the spatiotemporal regulation of the Ca^{2+}-cAMP-PKA oscillatory circuit. Specifically, we proposed that AKAP79/150 might be able to create a kinetically-distinct, regulatory nanodomain that is able to finely-tune and shape signaling within the circuit (Tenner 2016) In order to test this hypothesis, we fused full-length AKAP79 to the FRET-based biosensor (Ci/Ce)Epac2-camps (Everett et al. 2013) to monitor cAMP dynamics in the immediate vicinity of AKAP79/150 (Figure 2.1a), and transiently transfected the targeted sensor and the red Ca^{2+} reporter RCaMP (Akerboom et al. 2013), in MIN6 beta cells. The cAMP sensor was clearly membrane-localized via palmitoylation and polybasic domains of AKAP79 (Delint-Ramirez et al. 2011) (Figure 2.1a). Upon treatment with tetraethylammonium chloride (TEA, 20mM), a potent K^+ channel blocker, to trigger the oscillatory circuit, we observed synchronized, oscillatory cAMP/Ca^{2+} responses. Despite the cell-to-cell heterogeneity of the oscillating Ca^{2+} signal (ie. variations in frequency, amplitude, and regularity), significant subpopulations of cells displayed cAMP oscillations that were either in phase (approx. 36%) or completely out of phase (approx. 32%) with their Ca^{2+} signal (approx. 32% were unresponsive/indeterminate) (Figure 2.1b). Explicitly, each transient spike in intracellular Ca^{2+} was associated with either a transient increase in cAMP (“in-phase”) or a transient decrease in cAMP (“out-of-phase”), in responding cells. To quantify the cAMP-Ca^{2+} phase relationship, we measured the lag time by calculating the cross-correlation between the two normalized, oscillatory signals and finding the absolute value of the shortest delay yielding the maximum correlation (Figure 1d,e). In-phase cAMP oscillations corresponded to short lag times (typically < 20sec) while out-of-phase oscillations mostly possessed longer lag times. The observed in-phase cAMP oscillations within AKAP79/150 microdomains (avg. time lag 13sec ± 3sec, n=60) is striking (Figure 2.1b), especially compared to previous measurements of cytoplasmic cAMP using untargeted sensors that yielded only out-of-phase oscillations (Ni et al. 2011; Landa et al. 2005). Importantly, we also found that the lag time for AKAP79/150-centric cAMP correlated strongly with sensor expression with cells with low levels of sensor present displaying predominantly in-phase cAMP oscillations and cells with high levels of the AKAP79/150-fused biosensor exhibiting out-of-phase oscillations. Overexpression of AKAP79/150 likely changed the stoichiometry of signaling complexes and resulted in unsuccessful targeting of the biosensor to functional AKAP79/150 microdomains, and so in all subsequent analysis except where noted (eg. “highly-expressed” sensor) we considered only responding cells below an empirically-determined AKAP79-sensor expression threshold (Figure 2.2a,b).

The in-phase Ca^{2+}/cAMP oscillations within the AKAP79/150 microdomains are in sharp contrast to the out of phase oscillations in the cytosol. To determine if the in-phase Ca^{2+}/cAMP oscillations is a feature of membrane compartments and specific to the AKAP79/150 microdomains, we examined the cAMP dynamics within the general plasma membrane (PM) compartment. We fused the lyn kinase palmitoylation sequence to the Epac2-camps probe, expressed the plasma membrane targeted biosensor in MIN6 cells and stimulated the circuit (Wachten et al. 2010). Interestingly, we also observed unanimous, robust out-of-phase cAMP oscillations (lag time 47sec +/- 4sec, n=24) (Figure 2.1c). Each local peak of intracellular Ca^{2+} (approx.. 2–4x RFP increase) corresponded to a local trough in cAMP (-5-25% FRET ratio change), followed by a slower reversal of both signals to a pre-stimulated baseline, suggesting that increasing Ca^{2+} levels are coupled with decreasing cAMP in this compartment. The stark contrast between cAMP dynamics at the AKAP79/150 scaffold and the general PM hints at a differential, spatiotemporal regulation of the oscillatory circuit and suggests that the cAMP-Ca^{2+} phase relationship is compartmentalized.

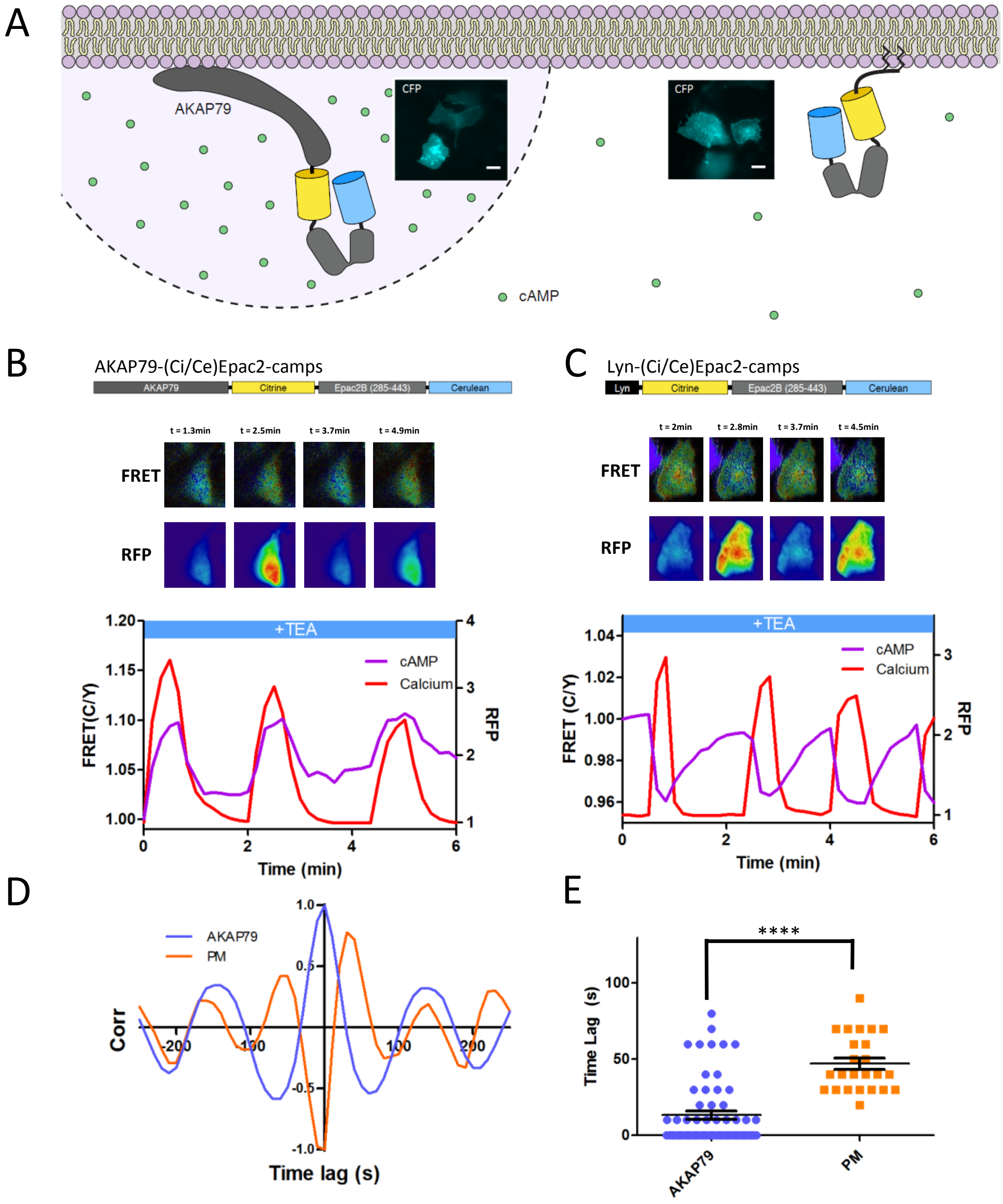

Figure 2.1 The phase of oscillating cAMP is shifted between the AKAP79/150 compartment and the general plasma membrane compartment, relative to Ca^{2+}. (A) Depiction of the AKAP79 compartment and plasma membrane compartment, including targeted cAMP biosensor (Ci/Ce)Epac2-camps to measure the compartment-specific cAMP signaling. Image insets show CFP fluorescence at plasma membrane for AKAP79-(Ci/Ce)Epac2-camps (left) and lyn-(Ci/Ce)Epac2-camps (right). (scale 10um) (B) Schematic of the AKAP79-(Ci/Ce)Epac2-camps sensor. Pseudocolor images of a representative TEA-induced oscillating MIN6 beta cell expressing the AKAP79-(Ci/Ce)Epac2-camps and RCaMP probes to measure AKAP-specific cAMP and cytosolic Ca^{2+}, respectively. The cyan over yellow emission ratio is proportional to cAMP concentration and the RFP signal is proportional to Ca^{2+} concentration. Representative single cell traces of an in-phase oscillating beta cell, whole-cell fluorescence measured. Purple trace is cAMP and red trace is Ca^{2+}. (C) Schematic of the Lyn-(Ci/Ce)Epac2-camps sensor.

Pseudocolor images of a representative TEA-induced oscillating MIN6 beta cell expressing the Lyn-(Ci/Ce)Epac2-camps and RCaMP probes to measure PM-cAMP and cytosolic Ca^{2+}, respectively. The cyan over yellow emission ratio is proportional to cAMP concentration and the RFP signal is proportional to Ca^{2+} concentration. Representative single cell trace of an out-of-phase oscillating beta cell, whole-cell fluorescence measured. Purple trace is cAMP and red trace is Ca^{2+}. (D) Cross-correlation between the oscillatory Ca^{2+} and cAMP signals from the representative in-phase AKAP79 (blue) and out-of-phase PM (orange) beta cells from B, C. (E) Time lag (sec) between the cAMP and Ca^{2+} signals for the two compartments (AKAP79 blue, PM orange). Found by the taking the absolute value of the shortest delay yielding the maximum cross-correlation. (time lag for AKAP79/150 is 13sec ± 3sec, time lag for general PM is 47sec ± 4sec) ($p<0.05$)

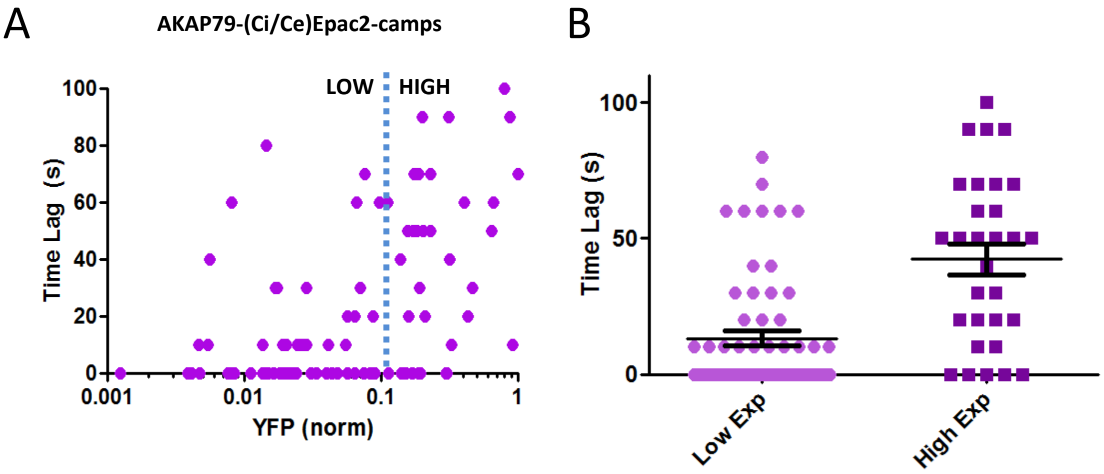

Figure 2.2 The time lag, and thus cAMP phase, depends on the expression level of AKAP79-(Ci/Ce)Epac2-camps (A) Time lag vs. normalized YFP fluorescence (measure of relative expression of the AKAP79-targeted sensor by YFP acceptor) shows a positive correlation between the amount of sensor expressed and the length of time lag. We stratified the cells into "low" and "high" expressers by empirically defining an intensity threshold. (B) The observed expression dependence can be clearly seen here, were low-expressing cells displayed mostly in-phase cAMP oscillations (avg time lag 13s ± 3s) at AKAP79/150 while high-expressing cells tended to have longer time lag (more cells exhibited out-of-phase cAMP oscillations) (avg time lag 42s ± 6s).

The oscillation phase is regulated by balanced activities of Ca^{2+} sensitive ACs and PDEs

Since TEA induces continuous Ca^{2+} oscillations, to determine more precisely the temporal relationship between Ca^{2+} and cAMP at the general PM, we measured the impulse response of the circuit to a short membrane depolarization stimulus. KCl (15mM) addition and washout was used to elicit a transient influx of Ca^{2+} (cite) and we observed a synchronous cAMP decrease (avg. -7.6% ± 0.6%, n=20) followed by a return to baseline (Figure 2.3a). This suggested to us that increasing cytosolic Ca^{2+} was coupled to a decrease in PM-cAMP via Ca^{2+}-sensitive AC or PDE activities. Ca^{2+}-inhibited ACs (AC5,6) have low specific activity both in the presence and absence of physiological Ca^{2+} as well as a lower distribution in the pancreas (Defer et al. 2000), so we turned our focus to PDEs. Expression of the Ca^{2+}-dependent PDE1 family in MIN6, specifically PDE1C, has been implicated in modulating GSIS (Han et al. 1999). Acute addition of 8MM-IBMX (100uM), a relatively selective PDE1 inhibitor, effectively decoupled oscillatory cAMP from Ca^{2+} oscillations (n=18) (Figure 2.4a), suggesting that Ca^{2+}-triggered PDE1 activation might be mediating the transient cAMP drops. Of note, the overall increase of cAMP (avg. 9.8% ± 0.1%) on the slower timescale also led to an increase in the Ca^{2+} frequency, consistent with the previously identified role of cAMP/PKA in regulating the Ca^{2+} oscillation frequency (Ni et al. 2011). We also tested the role of two families of abundant PDEs in pancreatic beta cells, PDE3 and PDE4, on Ca^{2+}-mediated cAMP coupling by acute pharmacologic inhibition after initiating the oscillatory circuit. Treating cells with milrinone (PDE3 inhibitor, 10uM, n=12) or rolipram (PDE4 inhibitor, 1μM, n=15) slightly increased cAMP levels on a slow timescale but failed to have an effect on the cAMP-Ca^{2+} coupling or the phase (Figure 2.5a,b).

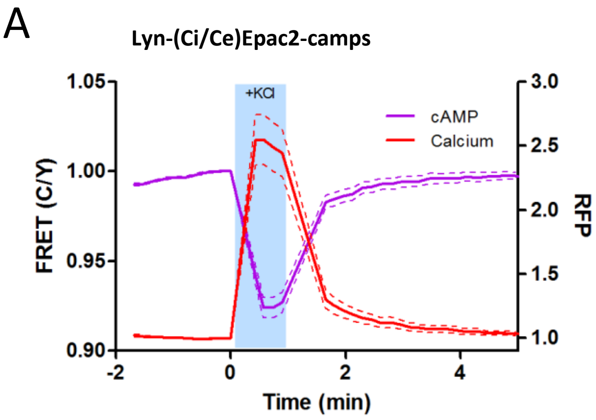

Figure 2.3 Impulse response of plasma membrane cAMP to a spike in Ca^{2+} (A) KCl-mediated depolarization triggers sharp Ca^{2+} entry which is coupled to a transient cAMP decrease (-7%). Purple trace is cAMP, red is Ca^{2+}.

Figure 2.4 Inhibition of the Ca^{2+}-sensitive PDE1 decouples plasma membrane cAMP from Ca^{2+} oscillations (A) Representative single cell trace of oscillating PM-cAMP. Acute inhibition of PDE1 family (8MM-IBMX) decouples the out-of-phase cAMP oscillations, leading to an abolishment of the cAMP oscillations. Purple trace is cAMP, red is Ca^{2+}.

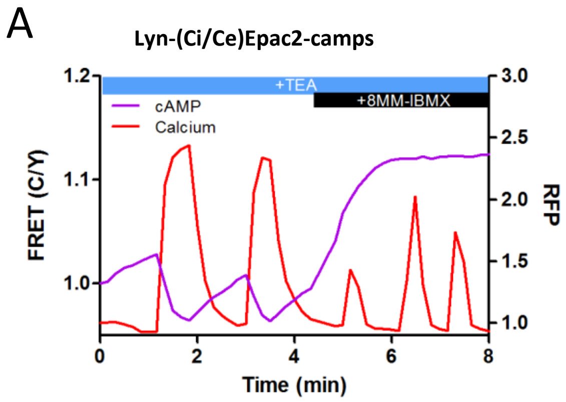

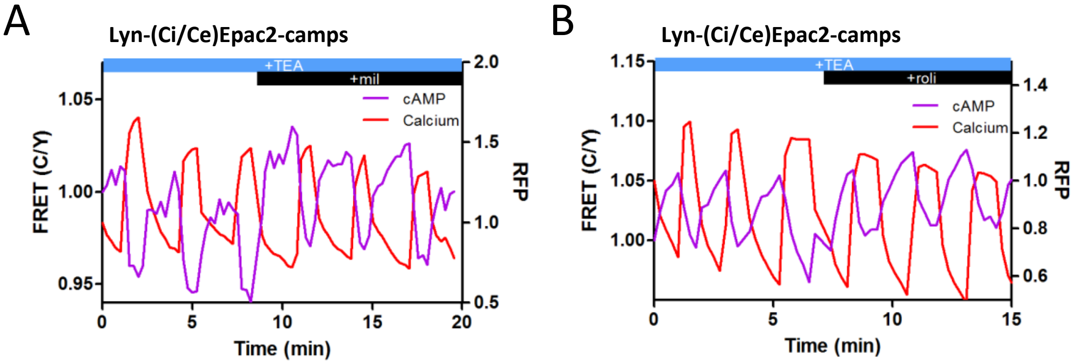

Figure 2.5 Inhibition of PDE3 and PDE4 does not decouple plasma membrane cAMP oscillations from Ca^{2+} (A) Representative trace depicting out-of-phase PM-cAMP oscillations. Acute inhibition of PDE3 (milrinone 10uM) did not affect cAMP oscillations apart from a small increase on a longer time scale. Purple trace is cAMP, red is Ca^{2+}. (B) Representative trace depicting out-of-phase PM-cAMP oscillations. Similar to A, inhibition of PDE4 (rolipram 1uM) did not affect cAMP oscillations, relative to Ca^{2+}.

In order to gain a more quantitative understanding of the regulation of the cAMP-Ca^{2+} phase relationship, we extended our previous mathematical model of the beta cell circuit (Ni et al. 2011) to include well-mixed, Ca^{2+}-driven PDE and AC activity components. Kinetic parameters for each opposing arm were taken from the Ca^{2+}-activatable PDEs and ACs including PDE1 and AC8, an abundant Ca^{2+}-activatable transmembrane AC isoform in beta cells that has been shown to mediate sustained insulin secretion and associate with the AKAP79/150 scaffold (Dou et al. 2014). By computationally manipulating the activity of each, the cAMP phase can exist as either out-of-phase or in-phase with respect to Ca^{2+}, indicating that the phase relationship can be represented as a function of the relative strength between such Ca^{2+}-sensitive players, echoing previous work (Figure 2.6a) (Peercy et al. 2015; Fridlyand et al. 2007). According to the model, increasing the relative contribution of AC8, for example by increasing the concentration of AC8, can change the cAMP-Ca^{2+} phase relationship from out-of-phase to in-phase.

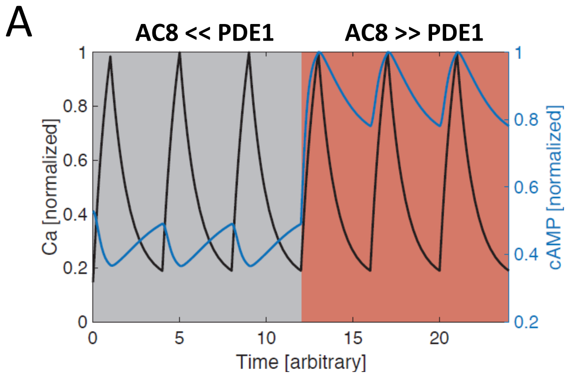

Figure 2.6 Manipulation of the relative strength between Ca^{2+}-activatable AC8 and PDE1 is sufficient to describe both cAMP-Ca^{2+} phase relationships (A) By manipulating a parameter describing the relative strength of AC8 vs. PDE1 (Supp.), cAMP oscillations can exist as either out-of-phase or in-phase (blue trace is cAMP, black is Ca^{2+}), in a simple well-mixed model of the beta cell.

To test this prediction, we first turned our attention to oscillatory cAMP at the general PM and overexpressed full-length AC8. Interestingly, we found that AC8 overexpression reversed the cAMP-Ca^{2+} phase relationship in a titratable regime where the percentage of in-phase oscillating cells correlated with increasing amounts of the cotransfected AC8 (0 – 1000ng AC8 transfected, n=56) (Figure 2.7a,b). This demonstrates that higher AC8 levels are sufficient to reverse the cAMP phase at the PM in the presence of TEA-stimulated, global Ca^{2+} oscillations. Furthermore, overexpression of extremely low amounts of AC8 (50ng transfected) was also sufficient to reverse the cAMP phase at highly-expressed AKAP79/150 (500ng transfected) compartments (out-of-phase to in-phase, monitored by highly-expressed AKAP79-Epac2-camps), hinting at a unique AKAP79/150-centric sensitivity to AC8 perhaps due to their interaction (Figure 2.8a).

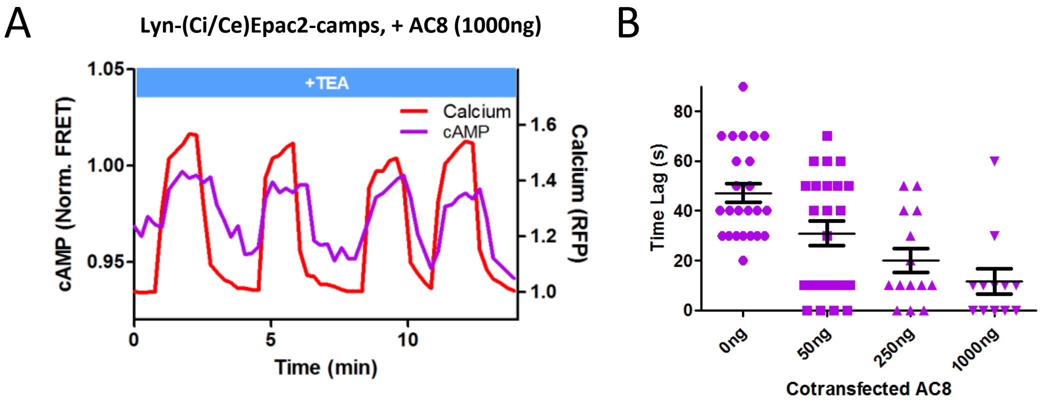

Figure 2.7 Supplementing beta cells with AC8 is sufficient to reverse the plasma membrane cAMP phase (A) Representative trace from oscillating beta cell depicting PM-cAMP in the presence of co-transfected AC8 (1000ng). Overexpression of AC8 is sufficient to elicit in-phase cAMP oscillations at the PM. Purple trace is cAMP, red is Ca^{2+}. (B) A dose-dependent relationship was observed where more AC8 transfected corresponded to responding cells exhibiting shorter time lag (more cells exhibited in-phase cAMP).

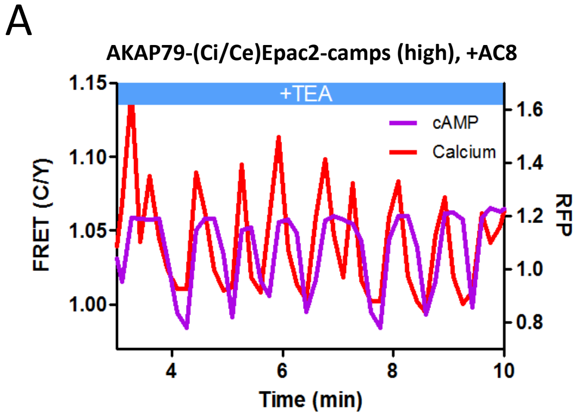

Figure 2.8 cAMP oscillations are in-phase around high-expressing AKAP79 cells when minimal amounts of AC8 are cotransfected (A) In cells highly expressing the AKAP79-cAMP sensor (500ng transfected), all cells oscillate with in-phase cAMP upon the cotransfection of a minimal amount of AC8 (50ng) (n=7). Purple is cAMP and red is Ca^{2+}.

To elucidate the role of the Ca^{2+}-activatable AC/PDE balance and cAMP-Ca^{2+} phase relationship within the AKAP79/150 compartment, we measured the KCl-induced impulse response here as we had done previously for PM-cAMP, and observed a synchronous, small rise in cAMP (3.0% ± 1.8%, n=12) upon the sharp influx of Ca^{2+} (Figure 2.9a). This striking difference compared to the PM-cAMP impulse response further highlights the AKAP79/150 compartment as kinetically distinct from the general PM. According to the math model, decreasing the relative contribution of AC8 would shift the cAMP-Ca^{2+} phase relationship from in-phase to out-of-phase, as the relative contribution from Ca^{2+}-triggered PDE1 increases. To test this prediction, we first knocked-down endogenous AC8 in the MIN6 cells (Raoux et al. 2015) and observed most cells exhibited out-of-phase cAMP oscillations at the AKAP79/150 compartment (n=11) (Figure 2.10a), indicating an AC8-specific role in mediating the cAMP-Ca^{2+} phase signature. Additionally, we overexpressed full-length PDE1C to tilt the AC8/PDE1 balance and found this perturbation was also sufficient to drive more cells to elicit out-of-phase cAMP at AKAP79/150 (n=7) (Figure 2.10b). Taken together, these phase manipulation experiments suggest that the cAMP-Ca^{2+} phase relationship is representative of a sensitive, compartmentalized balance between the Ca^{2+}-activatable activities of PDE1 and AC8.

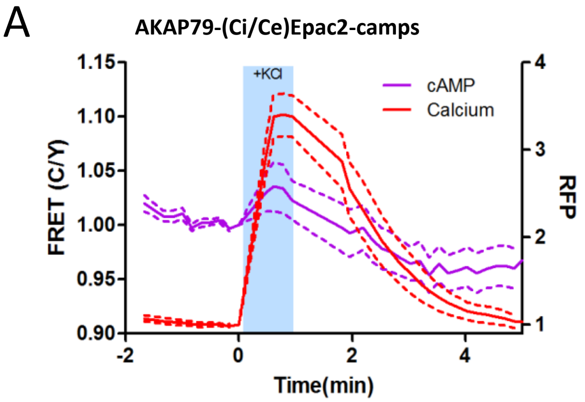

Figure 2.9 Impulse response of AKAP79 cAMP to a spike in Ca^{2+} (A) KCl-mediated depolarization triggers sharp Ca^{2+} entry which is coupled to a transient cAMP increase (+4%). Purple trace is cAMP, red is Ca^{2+}.

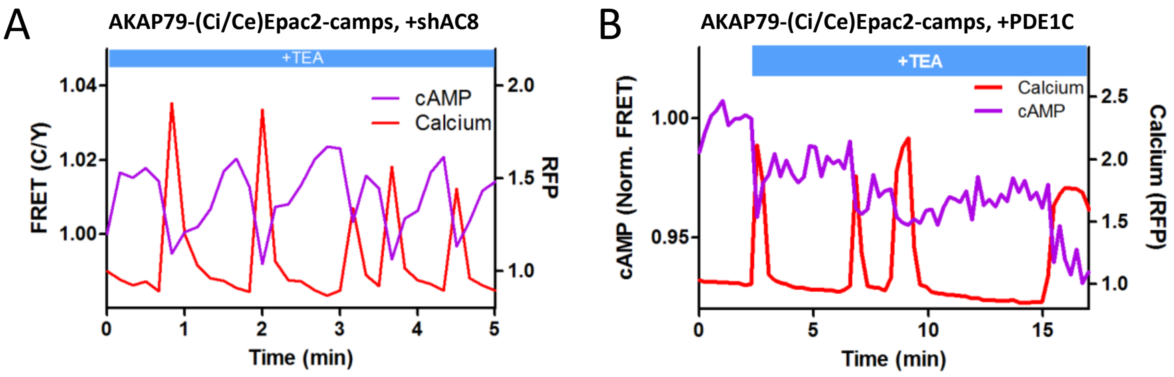

Figure 2.10 cAMP phase reversal at AKAP79/150 compartment by knocking down AC8 or overexpressing PDE1C (A) By knocking-down AC8, the cAMP phase at AKAP79/150 is reversed from mostly in-phase cells to out-of-phase, as seen in this representative cell trace. Purple is cAMP, red is Ca^{2+}. (B) Phase reversal at AKAP79/150 can also be seen if PDE1C is overexpressed, further illustrating the connection between the cAMP-Ca^{2+} phase relationship and the fine balance between Ca^{2+}-sensitive components.

AC8 and the AKAP150 scaffold are localized in nanoclusters at the membrane

Both AC8 and AKAP79/150 are membrane-localized and associate with each other in beta cells (Willoughby et al. 2010) while PDE1 isoforms are found in the cytoplasm (Bender et al. 2006; Goraya et al. 2008). We sought to better understand the role of this differential localization of Ca^{2+}-driven cAMP sources and sinks in the context of the cAMP-Ca^{2+} phase relationship. The close spatial juxtaposition between the AKAP79/150 and general PM compartments presents a significant challenge for cAMP compartmentation where cAMP oscillations are distinctly regulated within these adjacent microdomains. Indeed how is cAMP, as a rapidly diffusing small molecule, spatially compartmentalized in cells is not clearly understood (ref), especially given the low catalytic efficiency of single cAMP producing and degrading enzymes. Based on our previous finding that AKAP79 form nanoclusters on the plasma membrane, we hypothesize that AC8, possibly with the help of AKAP150, form nanoclusters on the plasma membrane of MIN6 cells to compartmentalize cAMP. To test this hypothesis, we took a closer look at the spatial organization of AC8 and AKAP150 at the membrane. In order to investigate the nanoscale architecture at the PM, we utilized STORM microscopy in TIRF to obtain a super-resolved view of each protein. We found the AKAP150 scaffold was organized in clusters with a mean diameter of 148nm ± 8nm (n=9) (Figure 2.11a-c), consistent with many recent reports demonstrating AKAP79/150's tendency to cluster/multimerize in other cell types (Zhang et al. 2016; Tajada et al. 2017, Mo et al. 2017, Purkey et al. 2018). This suggested to us that the AKAP79/150 compartment-specific cAMP phase is representative of the balanced cAMP generation and degradation within these AKAP clusters. Due to the known interaction between AKAP79 and AC8, next we probed the spatial organization of AC8. We found AC8 also distributes non-uniformly at the PM and clusters more strongly than AKAP150, with a tighter mean diameter of 106nm ± 2nm and an average nearest-neighbor spacing of 296nm between cluster centers (n=7) (Figure 2.11b,c). This difference in cluster size might be due to a higher-order structure of the co-organized AKAP150 and AC8, and more work will need to be done to probe this. With the evidence of the nanoscale organization of AKAP150 and AC8 on the plasma membrane, we further hypothesized that the increased spatial density of Ca^{2+}-driven cAMP sources within the AKAP150 clusters is important in compartmentalizing cAMP production and mediating the in-phase cAMP signal at the AKAP79/150 scaffold.

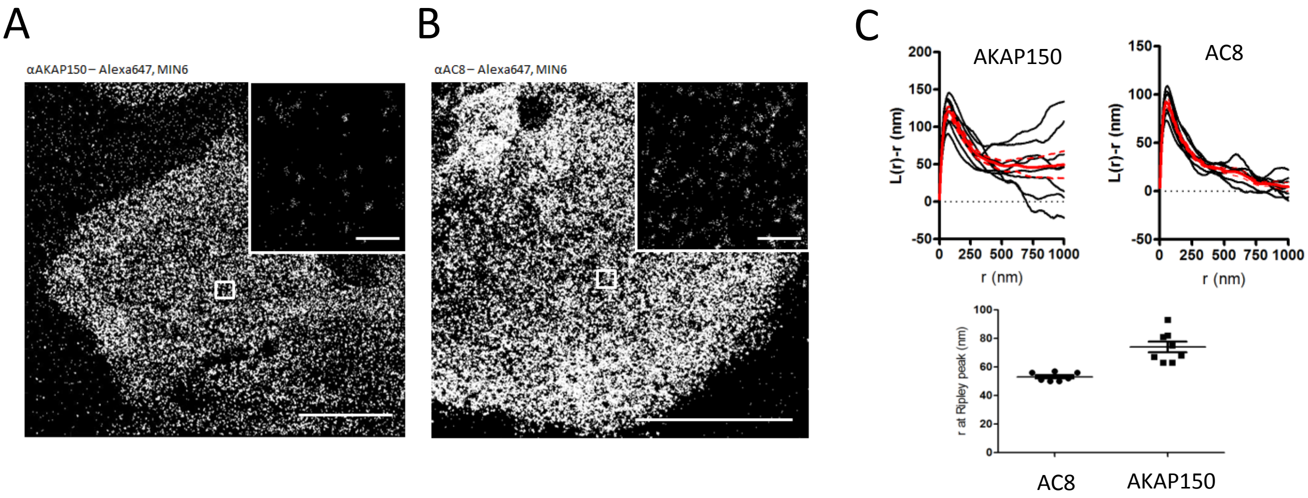

Figure 2.11 Super-resolution STORM images of AKAP150 and AC8 at the surface of MIN6 beta cells indicate both proteins cluster (A) Super-resolved image of AKAP150 (Alexa647) showing clustering of the scaffold. Scale 10µm, inset 500nm. (B) Super-resolved image of AC8 (Alexa647) showing clustering of the Ca^{2+}-sensitive AC. Scale 10µm, inset 500nm. (C) Ripley-K analysis measures the average radii of clusters, and indicates AC8 clusters (53nm) are "tighter" than AKAP150 clusters (76nm).

cAMP-Ca^{2+} phase relationship is modulated by AKAP150:AC8 clustering

In order to probe the role of AKAP79/150:AC8 clustering in the cAMP-Ca^{2+} phase relationship, we sought to build a mathematical framework to describe the compartmentalization. We adapted a 2D reaction-diffusion model (Haselwandter et al. 2015) to construct a minimal experimental system with AKAP79/150 and AC8 at the PM. Briefly, the attractive interactions between AKAP79/150, itself, and AC8, coupled with diffusion, can create a positive feedforward loop and stabilize spatial patterning of AKAP79/150:AC8 within clusters at the membrane (Supp.). We then tuned the model and optimized parameters using the AC8 STORM cluster measurements (106nm diameter, 296nm nearest-neighbor distance). To connect the clustering with the Ca^{2+}-cAMP-PKA oscillatory circuit, we used the 2D steady-state AKAP79/150:AC8 pattern (Figure 2.12a) as the upper boundary in a model volume and selected a simple prism domain (400nm x 400nm x 600nm) centered about one AKAP79/150:AC8 cluster for our simulations. We extended the previous well-mixed beta cell model to include a 3D spatial component with cAMP diffusion (60μm^2/s). By having AC8 within the AKAP79/150:AC8 clusters on the PM face and PDE1 well-mixed throughout the volume, we could describe Ca^{2+}-driven cAMP oscillations that were in-phase within the immediate vicinity of a cluster, but sharply transitioned out-of-phase outside the cluster (>250nm from center) (Figure 2.12b). Unsurprisingly, the regime that recapitulates this phase relationship is sensitive to the spatially-restricted AC8/PDE1 balance and the diffusivity of cAMP (data not shown).

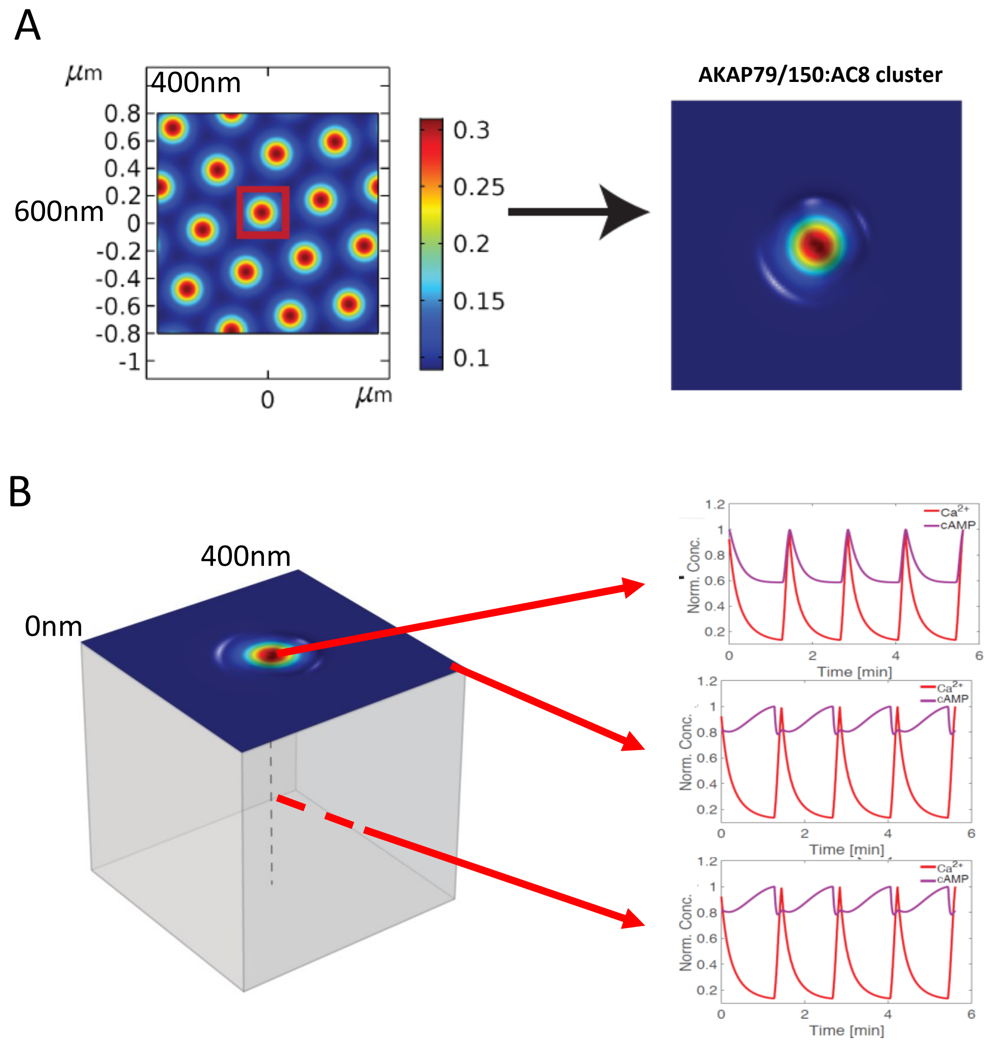

Figure 2.12 cAMP-Ca^{2+} phase relationship can be described by a 3D reaction-diffusion model involving co-clusters of AKAP79/150 and AC8 (A) 2D Reaction-diffusion steady state depicting co-clustering of AKAP79/150 and AC8. (B) 3D reaction-diffusion model of a single co-cluster positioned at the PM in the beta cell, taken from the 2D steady state, in a 400nm cubic volume. cAMP oscillates in-phase immediately within an AKAP79/150:AC8 co-cluster due to the high effective concentration of AC8, but out-of-phase at the PM or cytosol due to the presence of PDE1. Purple trace is cAMP, red is Ca^{2+}.

According to the model, weakening the interaction between AC8 and AKAP79/150 diminishes the reinforcing loop and impairs cluster stabilization. Without the high local concentration of AC8 driving a net positive cAMP production within an AKAP79/150 cluster, cAMP is predicted to oscillate out-of-phase with Ca^{2+} regardless of PM location (Figure 2.13). To test this prediction, we overexpressed the amino terminus of AC8 ($AC8^{1-106}$) required for interaction with AKAP79/150 (Willoughby et al. 2010) in order to compete off endogenous AC8 from the endogenous AKAP150 scaffold. The disruption of the AC8-AKAP150 interaction was validated by transiently transfecting EGFP-tagged $AC8^{1-106}$ in MIN6 and performing proximity ligation assay (PLA). Compared to non-transfected cells, cells expressing the $AC8^{1-106}$ peptide had a 39% ± 4% reduction in the number of PLA signals, indicating a decrease in the number of AKAP150:AC8 interactions (Figure 2.14a). By measuring AKAP79/150-localized cAMP in the presence of $AC8^{1-106}$, we observed a significant increase in the average lag time (43sec ± 6sec, n=33) due to a higher percentage of cells exhibiting out-of-phase cAMP oscillations, indicating that the AKAP79/150:AC8 competitor peptide was sufficient in reversing the phase relationship in the AKAP79/150 compartment. In addition, this nanoscale perturbation establishes the regulatory role of the AKAP79/150:AC8 interaction in mediating the compartmentalized cAMP-Ca^{2+} phase relationship.

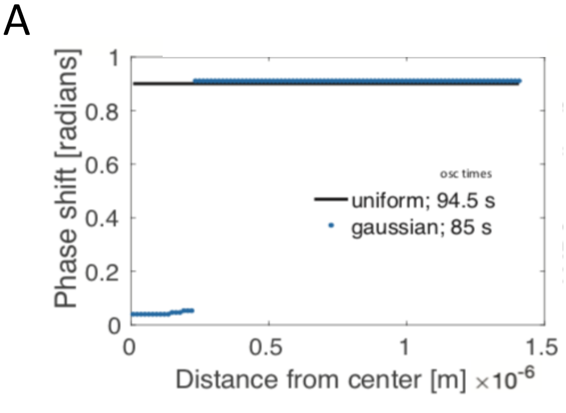

Figure 2.13 Disturbance of the AKAP150:AC8 interaction is predicted to reverse the cAMP phase relationship at AKAP79/150 nanodomain (A) The spatial transition from in-phase to out-of-phase cAMP (in-phase oscillations have a lower phase shift, as measured by a period-normalized time lag) is sharp due to cAMP diffusion and the difference in AC8/PDE1 distributions (blue trace). Disruption of the interaction between AKAP150 and AC8 promotes a loss of in-phase cAMP at AKAP79/150 due to a lower co-localized effective concentration of AC8.

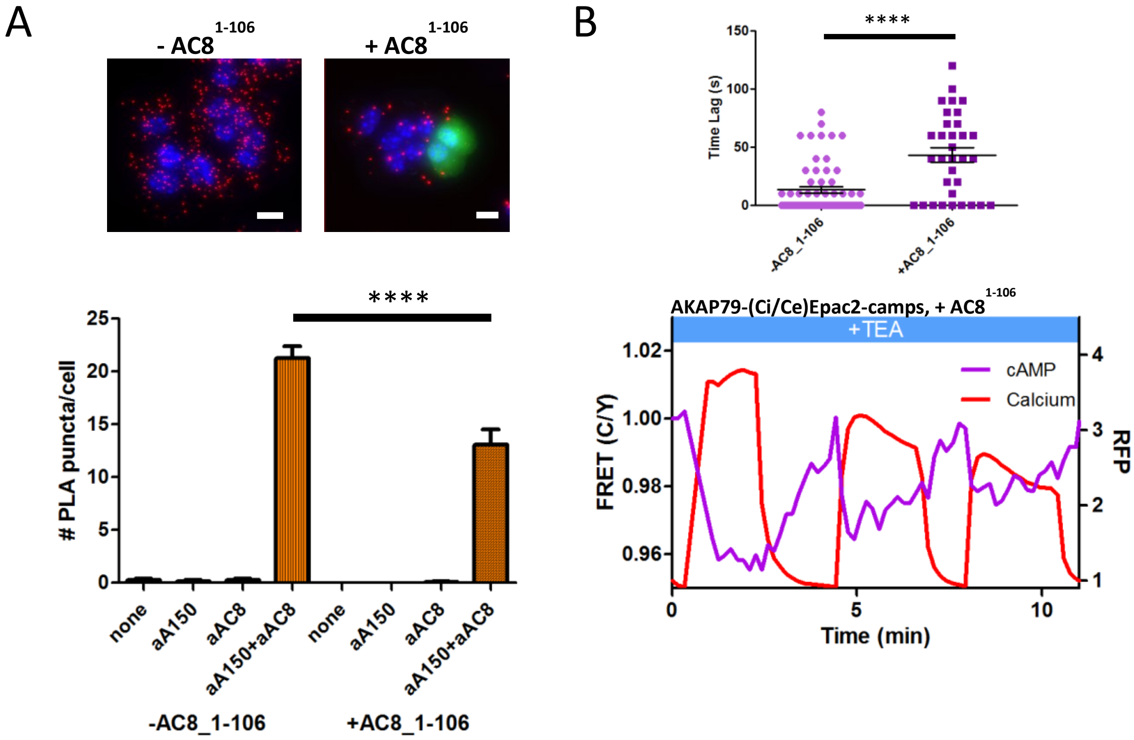

Figure 2.14 Disrupting AKAP79/150:AC8 interaction reverses the cAMP phase in the AKAP79/150 compartment (A) PLA on MIN6 in the presence and absence of EGFP-tagged AC8$^{1-106}$. Representative images, showing less PLA puncta signal in cells expressing the AC8$^{1-106}$ disruptor peptide (scale 10µm). In cells expressing the peptide, there's on average 38% less puncta per cell compared no non-expressing ($p<0.05$). Negative controls where one antibody is used shows minimal signal per cell. (B) Disruption of the AKAP79/150:AC8 interaction lengthens the time lag between the cAMP and Ca^{2+} signals at the AKAP79/150 compartment (avg time lag in absence of disruptor is 13sec ± 3sec, and presence of disruptor 43sec ± 6sec) ($p<0.05$). This is due to more cells displaying out-of-phase cAMP oscillations here, as evidenced in the shown representative cell trace. Purple is cAMP, red is Ca^{2+}.

AKAP79/150-mediated phase relationship modulates oscillatory Ca^{2+}

Oscillatory Ca^{2+} influx lies upstream of many important processes of the pancreatic beta cells such as pulsatile insulin secretion, transcriptional regulation, and metabolic homeostasis (Bertram et al. 2011). Multiple feedback mechanisms whereby cAMP modulates Ca^{2+} have been identified (Gromada et al. 2004), and so we wished to take a closer look at these connections in the context of the spatial compartmentalization of the phase relationship at AKAP79/150. Due to the modulatory role of PKA in the Ca^{2+}-cAMP-PKA oscillatory circuit and the presence of PKA at AKAP79/150, we wanted to know how in phase cAMP oscillations with respect to Ca^{2+} are translated into PKA activities and if spatial compartmentalization of the phase relationship is also maintained at the PKA activity level. To this end, we fused our biosensor for PKA activity (AKAR4) (Depry et al. 2011) to either full-length AKAP79 or the PM-targeting motif and expressed the sensors in MIN6 cells. Upon TEA stimulation, PKA activity was observed to oscillate in-phase at the AKAP79/150 compartment (n=6) but out-of-phase at the general PM (n=23) (Figure 2.15a,b), indicating that the compartmentalized phase relationship is preserved from cAMP to PKA.

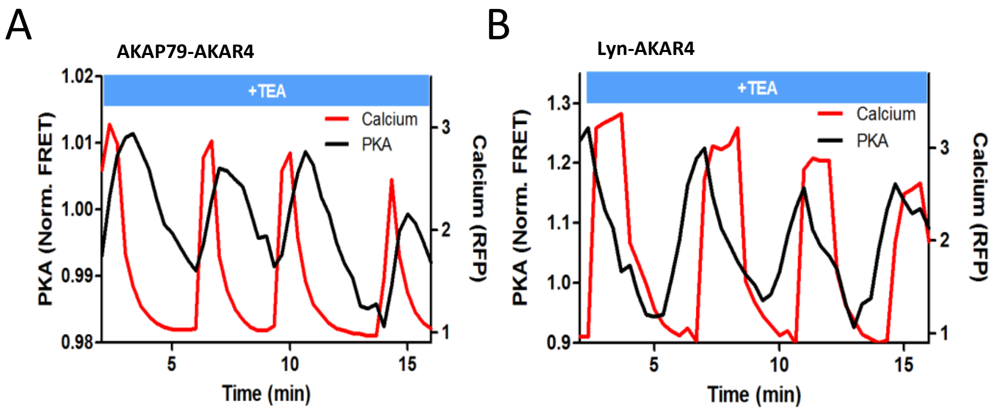

Figure 2.15 The phase of PKA activity is also compartmentalized between AKAP79/150 and the general plasma membrane (A) By fusing full-length AKAP79 to the genetically encoded reporter of PKA activity, AKAR4, we found PKA activity also oscillated in-phase at the AKAP79/150 nanodomain, echoing the in-phase cAMP dynamic with perhaps a slightly longer time lag. Shown here is a representative trace, black is PKA activity and red is Ca^{2+}. (B) PKA activity at the general PM oscillates out-of-phase, as does PM-cAMP, as measured by targeting AKAR4 to the PM with the lyn sequence. Shown here is a representative trace, black is PKA activity, red is Ca^{2+}.

Spatiotemporal organization of PKA signaling and its phosphorylation targets via AKAPs have been implicated in regulating several important pathways. For example, PKA has been shown to phosphorylate $Ca_V1.2$ in an AKAP79/150-dependent manner and this modification can influence the open probability of the channel (Murphy et al. 2014), suggesting a mechanistic link between local cAMP/PKA activity and global oscillatory Ca^{2+}. Thus, we sought to study the functional role of the spatially-compartmentalized cAMP-Ca^{2+} phase relationship in regulating intracellular Ca^{2+} dynamics. Ca^{2+} oscillations (monitored by RCaMP) were stimulated either in the presence of the EGFP-tagged AKAP79/150:AC8 disruptor peptide, $AC8^{1-106}$, to reverse the phase at the AKAP79/150 compartment, or EGFP alone as a control. Interestingly, we found that the expression of the disruptor peptide was correlated with a significant decrease in the peak ratio between the second Ca^{2+} peak and the first Ca^{2+} peak (control avg. -1.6%, n=270; $AC8^{1-108}$ avg. -10.8%, n=562), post TEA addition, hinting at impaired Ca^{2+} entry for sustained oscillations (Figure 2.16a). In addition to intracellular Ca^{2+} concentration, the precise timing of internal oscillatory events is theorized to be under the control of a master "pacemaker" circuit critical for modulating the cell's functions, such as glucose homeostasis and pulsatile insulin secretion (Fridlyand et al. 2010). In the presence of the disruptor peptide, cells exhibited a longer elapsed time between oscillatory Ca^{2+} peaks (control avg. 3.9min ± 0.1min, n=270; $AC8^{1-108}$ avg. 4.6min ± 0.1min, n=562), suggesting that the timing of the pacemaker circuit was disturbed (Figure 2.16b). In addition to the precise timing, the regularity of cytoplasmic Ca^{2+} in beta cells is crucial in mediating pulsatile insulin secretion from the pancreas (Gilon et al. 2002). By stratifying the disruptor peptide-expressing cell population into "low" and "high" expressers, and performing a blinded classification of responding cells based on the regularity of the Ca^{2+} oscillation, we found a positive correlation between the percentage of cells exhibiting irregular oscillations and the expression level of the disruptor peptide (42% for EGFP "none" control vs. 68% for high-expressing AC8$^{1-108}$ disruptor) (Figure 2.16c). Taken together, these data signifies that the compartmentalized cAMP-Ca^{2+} phase relationship regulates the oscillatory Ca^{2+} signal and plays an important role in determining the pace, regularity and sustainability of the Ca^{2+} oscillations.

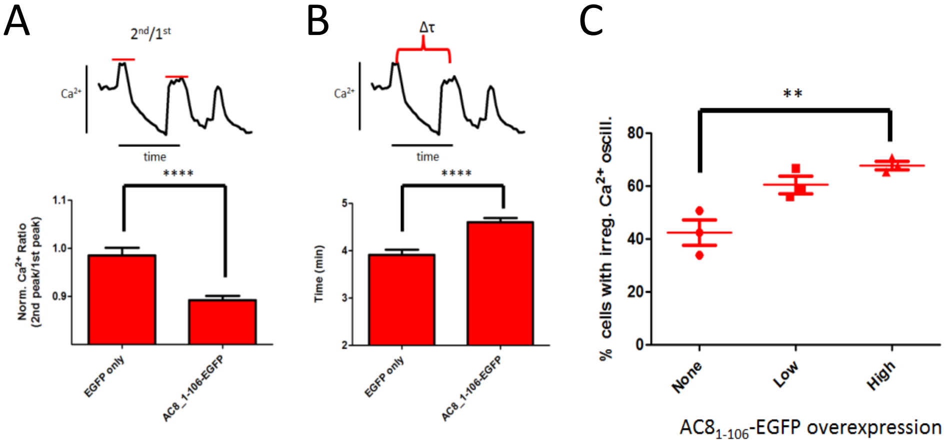

Figure 2.16 Ca^{2+} oscillatory dynamics are affected by expression of the disruptor peptide in beta cells (A) The ratio between the second and first Ca^{2+} peaks in a TEA-stimulated beta cell is reduced (~90%) in the presence of the AKAP79/150 disruptor peptide, a hallmark of transient oscillations. (B) The time between the Ca^{2+} oscillatory peaks is also lengthened (avg. ~30sec) when the disruptor peptide is expressed. (C) Higher expression of the disruptor peptide correlates with a greater percentage of cells exhibiting irregular Ca^{2+} oscillations.

Discussion

The phase in an oscillatory signaling circuit, like the amplitude and frequency, represents yet another mode of informational encoding which itself can be regulated spatially. Pancreatic beta cells provides a striking example of this regulation for the Ca^{2+}-cAMP-PKA circuit where the oscillatory cAMP/PKA phase relative to Ca^{2+} is distinctly regulated within plasma membrane compartments through intracellular organization of scaffolds and signaling effectors. Localized perturbation of this spatial phase signature disrupts global Ca^{2+} oscillations and thus has far-reaching consequences on the functional landscape of the beta cell.

Despite the enhanced understanding gained by the utilization of genetically encoded biosensors, careful consideration must be taken when monitoring compartmentalized signals. Expressing sensors fused to a protein-of-interest for localized signaling interrogation can disrupt native signaling pathways, both globally and locally, and thus such experiments require proper controls. For example, we observed that the AKAP79/150-centric cAMP phase not only differed from the cAMP phase at the general PM, but also depended on the absolute amount of the fused sensor present in each cell (cells with more expressed fused sensor correlated with AKAP-localized out-of-phase cAMP). Although AKAP79/150 has not been found to possess intrinsic enzymatic activity (Gold et al. 2011), we still checked for such an overexpression effect of the scaffold protein alone by monitoring PM-cAMP in cells overexpressing AKAP79 and found all cells exhibited out-of-phase cAMP (data not shown). More than likely, the sensor expression dependence was due to an over-abundance of the AKAP79/150 scaffold relative to other key assembly constituents such as AC8, and thus the stoichiometry of the signaling complex was not preserved (Levchenko et al. 2000). This was conveyed by the sensitivity of the cAMP phase to the balance between AC8/PDE1, as well as how “reconstitution” of the signaling complex at the highly-expressed AKAP79/150 scaffold by cotransfection of a minimal amount of AC8 retrieved the AKAP79/150-localized in-phase cAMP-Ca^{2+} phase relationship (Figure 2.8a). Along these same lines, compartmentalized kinetics of signaling complexes depend on the presence or absence of key interaction partners, and thus signaling roles may differ depending on the context or cell type. For example, AKAP79/150 has been shown to locally potentiate PKA signaling differently in neurons, neonatal rat ventricular myocytes, and pancreatic beta cells here, all using a similar AKAP79-AKAR construct to highlight the compartmentalized activity (Oliveria et al. 2003; Musheshe et al. 2018).

Compartmentalization of cAMP/PKA signaling is instrumental in processing a diverse set of inputs and mediating specific cellular functions; however, the mechanistic details of compartmentalization are still largely unresolved (Mesheshe et al. 2018). Given the measured kinetic rates of most ACs and PDEs, coupled with fast diffusion of the small cAMP molecule, the generation of local cAMP gradients around single enzymes is unmaintainable (Conti et al. 2014). Context-dependent discrepancies in some of the kinetics (ie. differences of *in vitro* versus *in vivo* measurements) or slower cAMP diffusion due to buffering have been proposed as potential compartmentalizing mechanisms (Agarwal et al. 2016). Here we propose that the nanoscale organization of key cAMP effectors and regulators, specifically the relative spatial arrangement of ACs and PDEs, coupled to a global stimulus, might also play an important role in the localization of cAMP signaling. Despite the slow rates measured for individual ACs, we computationally and experimentally describe conditions in which the generation of compartmentalized cAMP can emerge from the clustering of many AC8 enzymes at the membrane and bulk distribution of PDE1 in the cytoplasm. Although clustering of PDEs have been proposed as a potential localization mechanism for cAMP (Lohse et al. 2017), this is the first demonstration of AC clustering and a functional importance in maintaining this organization, to the best of our knowledge. Additionally, this system also serves as a general demonstration of how a cell can translate a diffuse, global signal (Ca^{2+}) into a compartmentalized signal (cAMP) by local activation and global inhibition, a strategy that is likely utilized in many other cellular contexts.

The functional consequences of reversing the compartmentalized cAMP phase at AKAP79/150 on intracellular Ca^{2+} oscillations suggests a possible mechanism of the Ca^{2+}-cAMP-PKA oscillatory circuit as a modulator of the pacemaker circuit in beta cells (Fridlyand et al. 2010), disruption of which is a hallmark of type 2 diabetes (Schmitz et al. 2002). AKAPs have been shown to compartmentalize and enrich cAMP/PKA signaling in many other cellular processes (Dell'Acqua et al. 2006, Mo et al. 2017) and several AKAP79/150-associated signaling effectors and pathways are sensitive to AKAP79-anchored PKA and potentiate Ca^{2+} dynamics, such as regulation of voltage-mediated Ca^{2+} entry via PKA-dependent phosphorylation of $Ca_V1.2$, the modulation of store-operated Ca^{2+} entry by both PKA-dependent STIM1 and Orai1 phosphorylation (Murphy et al. 2014; Thompson et al. 2015; Zhang et al. 2019). Additional levels of regulatory feedback within the oscillatory circuit have also been proposed, such as a negative feedback loop between PKA and AC8 (Willoughby et al. 2012). Future research will further dissect which PKA targets are involved in decoding the information embedded in the local phase control. Aside from AKAP79/150-dependent regulation of the global Ca^{2+} signal, localized cAMP/PKA signaling at the AKAP79/150 scaffold might also play a role in regulating downstream insulin secretion due to close interactions between AKAP79/150 and the insulin secretory granules via $Ca_V1.2$ (Barg et al. 2001). Several important components and processes of the secretory machinery have been identified as targets of cAMP/PKA signaling here, such as PKA-dependent mobilization of granules (Renstrom et al. 2004) and modulation of synaptosomal protein SNAP25 (Gao et al. 2016), as well as control of fusion pore formation by cAMP-dependent Epac (Gucek et al. 2018). As we have shown, compartmentalized cAMP/PKA signaling at the AKAP79/150 macromolecular complex is exquisitely-tuned and disruption of this spatiotemporal coordination is associated with functional repercussions.

The Ca^{2+}-cAMP-PKA oscillatory circuit in pancreatic beta cells integrates many important regulators of cellular function, and the precise coordination of each is required for proper signaling control. Here we have uncovered a spatiotemporal organization of the circuit where the oscillatory phase between cAMP/PKA and Ca^{2+} depend on the spatial proximity of the AKAP79/150 scaffold protein. The construction principles of this signaling nanodomain, including the dependence on spatial clustering of sinks and sources, are likely generalizable to many other compartmentalized signals.

Supplemental – Modeling (from M. Getz)

Well mixed system

Let us then consider the network shown in Figure 2.17. This network has been shown to exhibit oscillations due to the action of PKA on IP3 receptors and K_{ATP} plasma membrane channels. But this network is not easily solved analytically due to its various feedback. We therefore propose a simple model to allow discerning of solutions that allow in- and out-of-state solutions.

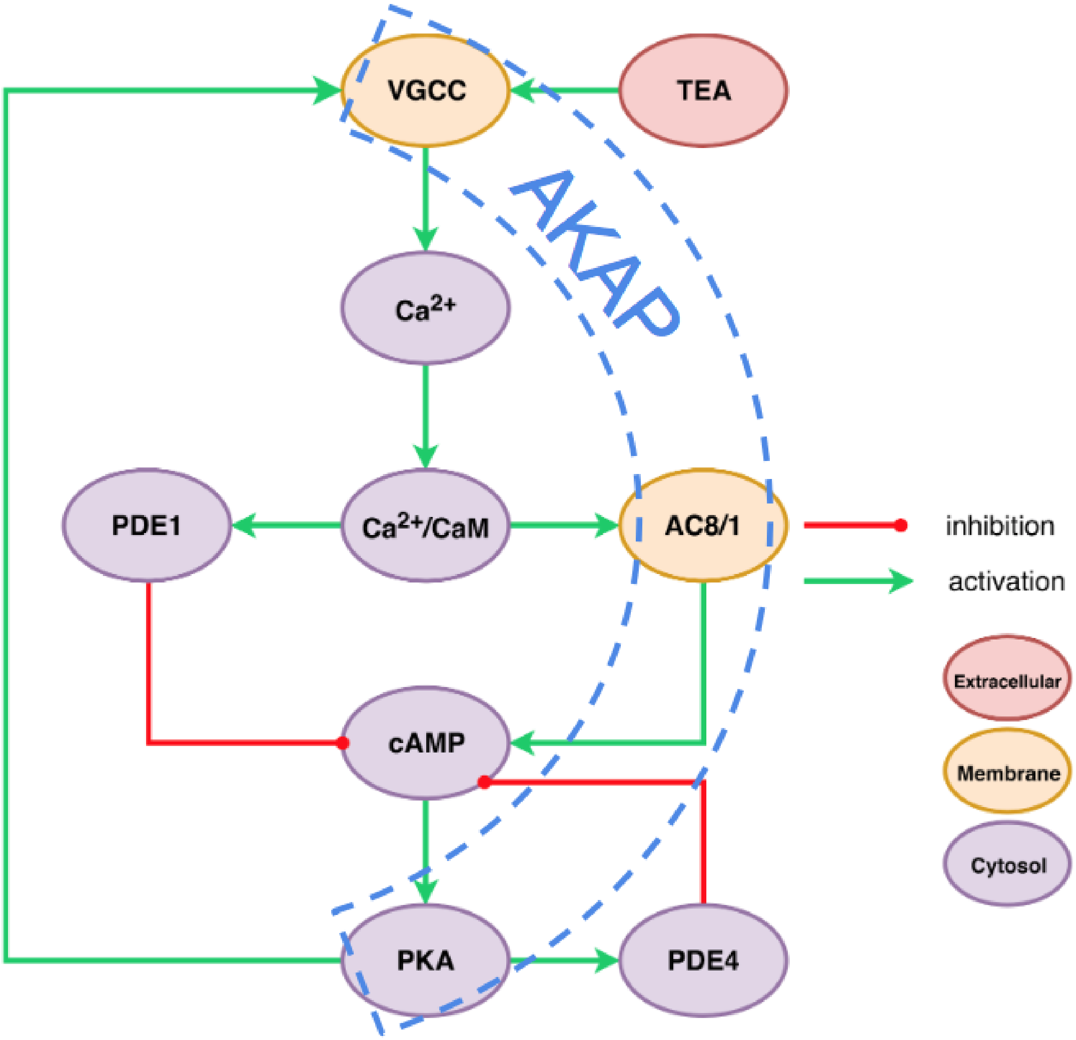

Figure 2.17 The full system network for PKA mediated Ca-cAMP oscillations.

Simplified model

Consider the following system, where S is the stimulus (Ca^{2+}), A is an activator (AC), B is an inhibitor (PDE1C), and R is the response element (cAMP).

Assumptions

The system is in a state that the change in R allows for S influx in a semi predictable manner. Therefore for this system is deemed to be stable there exists an S_0 that give the stable solution R_0. All constants must be positive to remain physical. There exists a constant independent source and sink within the system. The S dependent source is localized heterogeneously on the membrane, the independent source is located homogeneously, and both sinks are located uniformly in the cytosol.

Governing Equations

For simplicity, let both A and B be linear functions of S of the linear form $aS + b$. The well-mixed function of R is then,

$$\frac{dR}{dt} = v_1(a_1S + b_1) - v_2(a_2S + b_2)R + v_{ip} - v_{id}R$$

Numerical implementation

Well mixed system results were solved and analyzed in MATLAB. FEM simulations were performed in COMSOL and analyzed in MATLAB.

Well-mixed/analytic solutions

To analyze if the system lies in an in- or out-of-phase state we find the direction of the system change after initialization to S_0 (*i.e.* the basal stimulus). First we must solve for R_0, we find:

$$R_0 = \frac{v_1(a_1S_0 + b_1) + v_{ip}}{v_2(a_2S_0 + b_2) + v_{id}}$$

We then allow a pulse of S from S_0 to S_h, akin to VGCC opening allowing Ca flux. Therefore solving for the sign of R we see:

$$\frac{dR}{dt} = v_1(a_1S_h + b_1) + v_{ip} - (v_2(a_2S_h + b_2) + v_{id})\frac{v_1(a_1S_0 + b_1) + v_{ip}}{v_2(a_2S_0 + b_2) + v_{id}}$$

$$\frac{dR}{dt} = \frac{\big(v_1a_1(v_2b_2 + v_{id}) - v_2a_2(v_1b_1 + v_{ip})\big)(S_h - S_0)}{v_2(a_2S_0 + b_2) + v_{id}}$$

Since we only care about the sign we can then characterize the solution by

$$\frac{v_1a_1(v_2b_2 + v_{id})}{v_2a_2(v_1b_1 + v_{ip})} > 1 \qquad \text{in phase}$$

$$\frac{v_1a_1(v_2b_2 + v_{id})}{v_2a_2(v_1b_1 + v_{ip})} = 1 \qquad \text{transition}$$

$$\frac{v_1a_1(v_2b_2 + v_{id})}{v_2a_2(v_1b_1 + v_{ip})} < 1 \qquad \text{out of phase}$$

A simple model was then run to confirm the results with arbitrary parameters.

Spatial patterns

Although our system does show the ability to oscillate in and out of phase in a well behaved manner, this will not help if a uniform system is present. Therefore when moving to a 3D spatial map we must consider how two solution regimes can be recovered. Experimental data suggests that AKAP oligomerizes [Gao2011,Gold2010] forming up to tetrameric structures. This should allow spatial instabilities like those seen in [Haselwandter et al.] used to describe post synaptic domains.

Methods

Construction of reaction network

A biochemical network was constructed to allow previously shown interactions within β-cells, after the depolarization event. The computational model took into consideration of multiple channels; calcium, potassium, Leaky, and calcium sensitive potassium (Table [table:V]). Most importantly were the included feedback of PKA with KATP channels and inclusion of Ca^{2+}-sensitive ACs and PDEs. The model contains X parameters with Y free parameters, values are constrained through both previously peer reviewed publication results and new experimental results using FRET. AC and PDE data was collected from related isoforms.

We assumed signaling components were present in large enough quantities such that concentration changes were smooth and in a deterministic fashion. The well mixed model is comprised of only one compartment in which the conversion factors are assumed to be absorbed into the kinetic rate constants.

The network of interactions was constructed using COPASI (http://www.nrcam.uchc.edu, http://copasi.org/). The model was built in COPASI to leverage the inbuilt fitting techniques for initial guesses. The COPASI platform has built-in capabilities to conduct dynamic sensitivity analysis, which is an important aspect of dynamic systems modeling.

Turing patterns for generation of heterogeneity

A biochemical network showcased in [Christoff] was recreated using a finite element solver, COMSOL Multiphysics5.4 (Build:295), on a 1.6μmx1.6μm domain under the assumption of an independent time scale from the reaction kinetics after depolarization. We then modified the system to allow two receptor contributions (AC and VGCCs) and tuned connectivity (mostly parameters β and μ) such that similar patterns arose to what is observed in STORM imaging. For accuracy an extra fine mesh was used and periodic boundary conditions allowed for an assumption of a larger field of values existing.

Simulations of the full spatial systems

The well mixed network was imported into COMSOL Multiphysics5.4 (Build:295), to solve with in-homogenous boundary conditions. For computational simplification variations were performed with a Gaussian profile on the top boundary, the size of the domain and gaussian profile were informed by STORM images. The system is a 0.4x0.4x0.6 μm rectangle with periodic boundary conditions in the z planes. The top plane is assumed to be the membrane and the bottom is a no flux condition. For the membrane plane a Gaussian profile normalized such that the average value is 1μM (conversion to plane coord). The Ca^{2+} sensitive AC initial conditions (Gaussian profile) is fixed by setting diffusion to $\approx$0. This assumption is made through the statement that the patterns generated are pre-existing and not effected by the signaling event.

Comparisons to experimental data

Raw FRET data was used for model refinement. The data is compared for oscillation time and phase, with expected concentration change falling in the sensors sensitive range of$\approx$0.1-1μM of cAMP. Voltage gated channel sensitivities were not tuned, and only connection strengths between CaM to ACs and PDEs, which are largely less constrained in comparison, were varied.

Model validation and predictions

The model was validated on predictions to concentration perturbations (AC, PDE, etc.) and disruption of patterning (AC binding disruption) and their changes to the phase of the signal.

Reaction tables

LLLL # & Expression & Parameters & Reference

1 & $\frac{dV}{dt} = \frac{-I_{Ca}-I_K-I_L-I_{KCa}}{C_m}$ & C_m=5.3 pF & Ni,NatCellBio
2 & $I_{Ca} = g_{Ca}m_\infty(V-E_{Ca})$ & g_{Ca}=600 pS, E_{Ca}=100 mV & Ni,NatCellBio
3 & $m_\infty = \frac{1}{2}\left(1+tanh\left(\frac{V-v_1}{v_2}\right)\right)$ & v_1=-20 mV, v_2=24 mV & Ni,NatCellBio
4 & $I_K = g_K w(V-E_K)$ & g_K=240 pS, E_{Ca}=-75 mV & Ni,NatCellBio
5 & $\frac{dw}{dt} = \frac{\phi(w_\infty-w)}{\tau}$ & ϕ=35 $\frac{1}{s}$ & Ni,NatCellBio
6 & $\tau = \frac{1}{cosh\left(\frac{V-v_3}{2v_4}\right)}$ & v_3=-16 mV v_4=11.2 mV & Ni,NatCellBio
7 & $I_L = g_L(V-E_L)$ & g_L=150 pS, E_L=-75 mV & Zhang
8 & $I_{KCa} = g_{KCa}\frac{Ca}{Ca+K_{KCa}}(V-E_K)$ & g_{KCa}=2000 pS, E_{Ca}=-75 mV, K_{KCa}=5 μM & Ni,NatCellBio

[table:V]

LLLLL # & Reaction & Reaction flux & Kinetic Parameters & Ref.

9 & → Ca & $j_{\mathrm{Ca}_V}(1+k_{\mathrm{PKA}_V}[\mathrm{PKA}])+j_{\mathrm{Ca}_I}$ & C_m=5.3 pF & Ni,NatCellBio
10 & 2Ca + CaM ↔ Ca^{2}CaM & $k_f[\mathrm{Ca}][\mathrm{CaM}]-k_r[\mathrm{Ca^2CaM}]$ & k_f=3.6 $s^{-1}\cdot\mu M^{-1}$, k_r=8 s^{-1}

11 & Ca + Ca^{2}CaM ↔ Ca^{3}CaM & k_f[Ca][Ca^{2}CaM] $-$ k_r[Ca^{3}CaM] & k_f=11 $s^{-1} \cdot \mu M^{-1}$, k_r=195 s^{-1}

12 & Ca + Ca^{3}CaM ↔ Ca^{4}CaM & k_f[Ca][Ca^{3}CaM] $-$ k_r[Ca^{4}CaM] & k_f=59 $s^{-1} \cdot \mu M^{-1}$, k_r=500 s^{-1}

13 & AC + Ca^{2}CaM ↔ CaM·AC & k_f[AC][Ca^{2}CaM] $-$ k_r[CaM $\cdot$ AC] & k_f=1.7 $s^{-1} \cdot \mu M^{-1}$, k_r=10 s^{-1}

14 & CaM·AC + 2Ca ↔ AC* & $K_{cat}\,\frac{\text{[Ca][CaM·AC]}}{\text{Ca}+K_m}$ $-$ k_r[AC*] & K_{cat}=59.5 s^{-1}, K_m=0.1 μM, k_r=10 s^{-1}

15 & PDE + Ca^{2}CaM ↔ CaM·PDE & k_f[PDE][Ca^{2}CaM] $-$ k_r[CaM $\cdot$ PDE] & k_f=435 $s^{-1} \cdot \mu M^{-1}$, k_r=1 s^{-1}

16 & CaM·PDE + 2Ca ↔ PDE* & $K_{cat}\,\frac{\text{[Ca][CaM·PDE]}}{\text{Ca}+K_m}$ $-$ k_r[PDE*] & K_{cat}=1.81 s^{-1}, K_m=0.18 μM, k_r=1 s^{-1}

17 & PDE + Ca^{4}CaM ↔ PDE* & k_f[PDE][Ca^{4}CaM] $-$ k_r[PDE*] & k_f=435 $s^{-1} \cdot \mu M^{-1}$, k_r=1 s^{-1}

[table:Carxn]

LLLLL # & Reaction & Reaction flux & Kinetic Parameters & Ref.

18 & → cAMP & k_{base}([CaM $\cdot$ AC] + [AC]) + k_{act}[AC*] & k_{base}=0.1 s^{-1}, k_{act}=0.785 s^{-1}

19 & cAMP→ & k_{base}[cAMP] $\frac{\text{[CaM·PDE]+[PDE]}}{\text{[cAMP]}+K_m}$ + $k_{act}\,\frac{\text{[cAMP][PDE*]}}{\text{[cAMP]}+K_m}$ & k_{base}=2 s^{-1}, K_m= 0.6 μM k_{act}=20 s^{-1}

20 & cAMP→ & $V_{ind}\,\frac{\text{[cAMP]}}{\text{[cAMP]}+K_m}$ & V_{ind}=2.5 $\mu M \cdot s^{-1}$, K_m= 1.4 μM

21 & cAMP + R2 → R2$_b$ & k_f[cAMP][R2] $-$ k_r[R2$_b$] & k_f=1 $s^{-1} \cdot \mu M^{-1}$, k_r=0.00033 s^{-1} & McCulloch

22 & cAMP + R2$_b$ → R2$_{ba}$ & k_f[cAMP][R2$_b$] $-$ k_r[R2$_{ba}$] & k_f=1 $s^{-1} \cdot \mu M^{-1}$, k_r=0.00105 s^{-1} & McCulloch

23 & cAMP + R2$_b$ → R2$_{bb}$ & k_f[cAMP][R2$_b$] $-$ k_r[R2$_{bb}$] & k_f=1 $s^{-1} \cdot \mu M^{-1}$, k_r=0.00132 s^{-1} & McCulloch

24 & cAMP + R2$_{ba}$ → R2$_{bba}$ & k_f[cAMP][R2$_{ba}$] $-$ k_r[R2$_{bba}$] & k_f=1 $s^{-1} \cdot \mu M^{-1}$, k_r=0.0013 s^{-1} & McCulloch

25 & cAMP + R2$_{bb}$ → R2$_{bba}$ & k_f[cAMP][R2$_{bb}$] $-$ k_r[R2$_{bba}$] & k_f=1 $s^{-1} \cdot \mu M^{-1}$, k_r=0.00103 s^{-1} & McCulloch

26 & cAMP + R2$_{bba}$ → R2$_{bbaa}$ & k_f[cAMP][R2$_{bba}$] $-$ k_r[R2$_{bbaa}$] & k_f=1 $s^{-1} \cdot \mu M^{-1}$, k_r=0.0114 s^{-1} & McCulloch

27 & PKA + R2 → R2C & k_f[PKA][R2] $-$ k_r[R2C] & k_f=1 $s^{-1} \cdot \mu M^{-1}$, k_r=1.26E-7 s^{-1} & McCulloch

28 & PKA + R2$_b$ → R2$_b$C & k_f[PKA][R2$_b$] $-$ k_r[R2$_b$C] & k_f=1 $s^{-1} \cdot \mu M^{-1}$, k_r=2.52E-7 s^{-1} & McCulloch

[table:cAMPrxn]

LLLLL # & Reaction & Reaction flux & Kinetic Parameters & Ref.

29 & PKA + R2$_{ba}$ → R2$_{ba}$C & k_f[PKA][R2$_{ba}$] $-$ k_r[R2$_{ba}$C] & k_f=1 $s^{-1} \cdot \mu M^{-1}$, k_r=3.4E-6 s^{-1} & McCulloch
30 & PKA + R2$_{bba}$ → R2$_{bba}$C & k_f[PKA][R2$_{bba}$] $-$ k_r[R2$_{bba}$C] & k_f=1 $s^{-1} \cdot \mu M^{-1}$, k_r=0.000936 s^{-1} & McCulloch
31 & PKA + R2$_{bbaa}$ → R2$_{bbaa}$C & k_f[PKA][R2$_{bbaa}$] $-$ k_r[R2$_{bbaa}$C] & k_f=1 $s^{-1} \cdot \mu M^{-1}$, k_r=0.645 s^{-1} & McCulloch
32 & cAMP + R2C → R2$_b$C & k_f[cAMP][R2C] $-$ k_r[R2$_b$C] & k_f=1 $s^{-1} \cdot \mu M^{-1}$, k_r=0.000659s^{-1} & McCulloch
33 & cAMP + R2$_b$C → R2$_{ba}$C & k_f[cAMP][R2$_b$C] $-$ k_r[R2$_{ba}$C] & k_f=1 $s^{-1} \cdot \mu M^{-1}$, k_r=0.0142s^{-1} & McCulloch
34 & cAMP + R2$_{ba}$C → R2$_{bba}$C & k_f[cAMP][R2$_{ba}$C] $-$ k_r[R2$_{bba}$C] & k_f=1 $s^{-1} \cdot \mu M^{-1}$, k_r=0.358s^{-1} & McCulloch
35 & cAMP + R2$_{bba}$C → R2$_{bbaa}$C & k_f[cAMP][R2$_{bba}$C] $-$ k_r[R2$_{bbaa}$C] & k_f=1 $s^{-1} \cdot \mu M^{-1}$, k_r=7.84s^{-1} & McCulloch
36 & PKA + R2$_b$C → R2$_b$C$_2$C & k_f[PKA][R2$_b$C] $-$ k_r[R2$_b$C$_2$] & k_f=1 $s^{-1} \cdot \mu M^{-1}$, k_r=0.00324 s^{-1} & McCulloch
37 & PKA + R2C → R2C$_2$ & k_f[PKA][R2C] $-$ k_r[R2C$_2$] & k_f=1 $s^{-1} \cdot \mu M^{-1}$, k_r=2.81E-6 s^{-1} & McCulloch
38 & PKA + R2$_{ba}$C → R2$_{ba}$C$_2$ & k_f[PKA][R2$_{ba}$C] $-$ k_r[R2$_{ba}$C$_2$] & k_f=1 $s^{-1} \cdot \mu M^{-1}$, k_r=0.666 s^{-1} & McCulloch
39 & cAMP + R2C$_2$ → R2$_b$C$_2$ & k_f[cAMP][R2C$_2$] $-$ k_r[R2$_b$C$_2$] & k_f=1 $s^{-1} \cdot \mu M^{-1}$, k_r=0.762s^{-1} & McCulloch
40 & cAMP + R2$_b$C$_2$ → R2$_{ba}$C$_2$ & k_f[cAMP][R2$_b$C$_2$] $-$ k_r[R2$_{ba}$C$_2$] & k_f=1 $s^{-1} \cdot \mu M^{-1}$, k_r=2.91s^{-1} & McCulloch

[table:cAMPrxn2]

Variations on spatial pattern and model parameters

LLLL # & Expression & Parameters & Notes

E & $E = \frac{1-r-r_2-s}{1-\overline{r}-\overline{r_2}-\overline{s}}$ & &
v1 & $-b * R$ & &
v2 & $m_1 * E * \overline{r}$& &
v3 & $b * E * \frac{\overline{r}}{\overline{s}} * s$ & &
v4 & $-(m_1 + m_2 * \frac{\overline{s}}{\overline{r}}) * E * r$ & &

v5 & $\frac{m2}{\overline{r}} * E * r * s$ & &
v6 & $-\beta * s$ & &
v7 & $\beta * E * \overline{s}$ & &
v8 & $-\mu * E * s$ & &
v9 & $\frac{\mu}{\overline{s}} * E * s^2$ & &
$\frac{dr}{dt}$ & $-v_r(1-s)\nabla r - r\nabla s + v_1 + v_2 + v_3 + v_4 + v_5$ & &
$\frac{dr_2}{dt}$ & $-v_r(1-s)\nabla r_2 - r_2\nabla s + v_1 + v_2 + v_3 + v_4 + v_5$ & &
$\frac{ds}{dt}$ &$-v_s(1-r-r_2)\nabla s - s\nabla(r+r_2) + v_6 + v_7 + v_8 + v_9$ & &

[table:Pattern]

Materials and Methods

Gene Construction

For AKAP79-(Ci/Ce)Epac2-camps, AKAP79 (from Dr. John D. Scott) was PCR amplified to have HindIII/BamHI digestion sites and (Ci/Ce)Epac2-camps (from Dr. D. Cooper) was PCR amplified to have BamHI/EcoRI digestions sites. Both fragments were inserted into pcDNA3 (Invitrogen) backbone for mammalian expression (cAMP sensor is C terminal to AKAP79). For AKAP79-AKAR4, a similar approach was taken where AKAR4 was dropped between BamHI/EcoRI. For AC8 (from Dr. D. Cooper), $AC8^{1\text{-}108}$, and PDE1C (cDNA from Dr. Yan Chen), Gibson Assembly was used to insert the genes into the pcDNA3 mammalian expression vector. The shAC8 construct for AC8 knockdown was previously verified and a gift from Dr. Jochen Lang. RCaMP was a gift from Dr. Loren Looger.

Cell Culture

MIN6 cells (a mouse insulinoma beta cell line) were plated onto sterilized glass coverslips in 35-mm dishes and grown to 50–90% confluency in DMEM (10% FBS) at 37°C with 5% CO2. Cells were transfected using Lipofactamine 2000 (Invitrogen) and grown 20–48 h before imaging.

Imaging

Cells were washed twice with Hanks' balanced salt solution buffer and maintained in the dark at room temperature. Cells were imaged on a Zeiss Axiovert 200M microscope with a cooled charge-coupled device camera (MicroMAX BFT512, Roper Scientific, Trenton, NJ) controlled by METAFLUOR 6.2 software (Universal Imaging, Downingtown, PA). Dual red/cyan emission ratio imaging used a 420DF20 excitation filter, a 450DRLP dichroic mirror, and two emission filters [475DF40 for CFP and 653DF95 for RFP]. Dual yellow/red emission ratio imaging used a 495DF10 excitation filter, a 515DRLP dichroic mirror, and two emission filters [535DF25 for YFP and 653DF95 for RFP]. Dual cyan/yellow emission ratio imaging used a 420DF20 excitation filter, a 450DRLP dichroic mirror, and two emission filters [475DF40 for CFP and 535DF25 for YFP]. These filters were alternated by a filter-changer Lambda 10–2(Sutter Instruments, Novato, CA). Exposure time was 50–500 ms, and images were taken every 10–30 s. Fluorescence images were background-corrected by subtracting the fluorescence intensity of background with no cells from the emission intensities of cells expressing fluorescent reporters. The ratios of red/cyan, yellow/red, or yellow/cyan emissions were then calculated at different time points. The values of all time courses were normalized by dividing each by the average basal value before drug addition. Custom Java code and MATLAB scripts were written to segment cells, select ROIs, and analyze traces.

Super-resolution Imaging (STORM)

For fixed-cell stochastic optical reconstruction microscopy (STORM) imaging, cells were fixed with 4% paraformaldehyde (PFA) for 20 min and then washed with 100 mM glycine in Hanks' balanced salt solution (HBSS) to quench the free PFA. Cells were permeabilized and blocked in a permeabilization solution with 0.1% Triton X-100, 0.2% bovine serum albumin, 5% goat serum, and 0.01% sodium azide in HBSS. The cells were then incubated overnight at 4°C with an anti-AC8 antibody (Abcam, ab196686) at a 1:500 dilution or an anti- AKAP150 (Millipore Sigma 07-210) antibody at a 1:1000 dilution, followed by 1 to 2 hours with goat anti-rabbit Alexa 647–conjugated antibodies at 1:1000 dilution. The cells were then post-fixed again in 4% PFA, quenched with 100 mM glycine in HBSS, and washed with HBSS to prepare for imaging.

Immediately before imaging, the medium was changed to STORM-compatible buffer [50 mM tris-HCl (pH 8.0), 10 mM NaCl, and 10% glucose) with glucose oxidase (560 μg/ml), catalase (170 μg/ml), and mercapto-ethylamide (7.7 mg/ml). STORM images were obtained using a Nikon Ti total internal reflection fluorescence (TIRF) microscope with N-STORM, an Andor IXON3 Ultra DU897 EMCCD, and a 100× oil immersion TIRF objective. Photoactivation was driven by a Coherent 405-nm laser, while excitation was driven with a Coherent 647-nm laser. Illumination was done in a "near-TIRF" format, in which the TIRF angle was adjusted so that molecules in the nucleus were illuminated. All image analysis and image reconstruction were performed using both Nikon Elements analysis software and custom-written MATLAB scripts. Cluster measurements were performed using Ripley-K analysis and custom mean-shift code for segmentation.

Proximity Ligation Assay

Antibodies for AC8 and AKAP150, mentioned in STORM section, were buffer exchanged into DPBS and conjugated with MINUS or PLUS oligos, following the Sigma DuoLink *in situ* Probemaker kits. PLA experiments were performed using the Duolink® *in situ* red kit for proximity ligation assays according to the provided protocol. The only protocol modification was to extend the amplification time by 50 min. Briefly, cells were fixed and permeabilized as in the STORM experiments before incubation with PLUS and MINUS oligo-conjugated primary antibodies for 30 min at 37°C each with washes after each step. Ligation of the nucleotides and amplification of the strand occurred sequentially by incubating cells with first ligase then polymerase and detection solution. PLA experiments with AKAP95 antibodies from different species were used as positive controls in HEK293T cells, and experiments with just one oligolabeled primary antibody or the other were our negative control. Images were acquired on a Nikon Ti Eclipse epifluorescence scope with z-control. A cross section of the nucleus (3.6-5 µm) was acquired and the number of dots per cell was counted using the nucleus as reference.

Computational Modeling

See Supplementary section.

References

Agarwal, SR. et al. (2016). "Mechanisms restricting diffusion of intracellular camp." Sci. Rep. 6: 19577.

Akerboom, J. et al. (2013). "Genetically encoded calcium indicators for multi-color neural activity imaging and combination with optogenetics." Front. Mol. Neurosci. 6:2.

Barg, S. et al. (2001). "Fast Exocytosis with Few Ca^{2+} Channels in Insulin-secreting Mouse Pancreatic Beta Cells." Biophysical Journal. **81**(6): 3308-3323.

Bender, AT. et al. (2006). "Cyclic nucleotide phosphodiesterases: molecular regulation to clinical use." Pharmacol Rev. **58**(3): 488-520.

Berridge, M. et al. (1998). "Calcium – a life and death signal." Nature **395** 645-648.

Bertram, R. et al. (2011). "Electrical Bursting, Calcium Oscillations, and Synchronization of Pancreatic Islets." Adv Exp Med Biol. 654: 261-279.

Calebiro, D. et al. (2014). "cAMP signaling microdomains and their observation by optical methods." Front. Cell. Neurosci.

Clapham, D. (2007). "Calcium Signaling." Cell **131**(6): 1047-1058.

Conti, M. et al. (2014). "Cyclic AMP compartments and signaling specificity: role of cyclic nucleotide phophodiesterases." J. Gen. Physiol. 143: 29-38.

De Pitta, M. et al. (2008). "Coexistence of amplitutde and frequency modulations in intracellular calcium dynamics." Physical Review E **77**, 030903(R).

Defer, N. et al. (2000). "Tissue specificity and physiological relevance of various isoforms of adenylyl cyclase." American Journal of Physiology – Renal Physiology. **279**(3): F400-F416.

Delint-Ramirez, I. et al. (2011). "Palmitoylation targets AKAP79 protein to lipid rafts and promotes its regulation of calcium-sensitive adenylyl cyclase type 8." J. Biol. Chem. **286**(38): 32962-75.

Dell'Acqua, ML. et al. (2006). "Regulation of neuronal PKA signaling through AKAP targeting dynamics." Eur J Cell Biol. **85**(7):627-33.

Depry, C. et al. (2011). "Visualization of PKA activity in plasma membrane microdomains." Mol Biosyst. **7**(1): 52-8.

Dou, H. et al. (2015). "Calcium influx activates adenylyl cyclase 8 for sustained insulin secretion in rat pancreatic beta cells." Diabetologia. **58**(2): 324-333.

Draznin, B. (1988) “Intracellular calcium, insulin secretion, and action.” Am J Med. **85**(5A): 44-58.

Dupont, G. et al. (2011). “Calcium Oscillations.” Cold Spring Harb Perspect Biol 3(3).

Dyachok, O. et al. (2006). “Oscillations of cyclic AMP in hormone-stimulated insulin-secreting beta-cells.” Nature **439**(7074): 349-52.

Everett, E. et al. (2013). “An Improved Targeted cAMP Sensor to Study the Regulation of Adenylyl Cyclase 8 by Ca^{2+} Entry through Voltage-Gated Channels.” PLoS One. **8**(9): e75942.

Fridlyand, LE. et al. (2007). “Regulation of cAMP dynamics by Ca^{2+} and G protein-coupled receptors in the pancreatic beta cell: a computational approach.” Am J Physiol Cell Physiol. **293**(6):C1924-33.

Fridlyand, LE. et al. (2010). “Bursting and calcium oscillations in pancreatic beta-cells: specific pacemakers for specific mechanisms.” Am J Physiol Endocrinol Metab. **299**(4): E517-32.

Gao, J. et al. (2016). “Differential role of SNAP-25 phosphorylation by protein kinases A and C in the regulation of SNARE complex formation and exocytosis in PC12 cells.” Cell Signaling. **28**(5): 425-437.

Gilon, P. et al. (2002). “Control Mechanisms of the Oscillations of Insulin Secretion In Vitro and In Vivo.” Diabetes. **51**:S144-S151.

Gold, M. et al. (2011). “Architecture and dynamics of an A-kinase anchoring protein 79 (AKAP79) signaling complex.” PNAS. **108**(16): 6426-6431.

Goraya, TA. et al. (2008). “Kinetic properties of Ca^{2+}/calmodulin-dependent phosphodiesterase isoforms dictate intracellular cAMP dynamics in response to elecation of cytosolic Ca^{2+}.” Cell Signaling. **20**(2): 359-74.

Gromada, J. et al. (2004). “Glucagon-Like Peptide-1: Regulation of Insulin Secretion and Therapeutic Potential.” Basic and Clinical Pharmacology and Toxicology. **95**(6).

Gucek, A. et al. (2018). “Fusion pore regulation by Epac2/cAMP controls cargo release during insulin exocytosis.” bioRxiv.

Han, P. et al. (1999). “The calcium/calmodulin-dependent phosphodiesterase PDE1C down-regulates glucose-induced insulin secretion.” J. Biol. Chem. **273**(32): 22337-44.

Hanoune, J. et al. (2001). “Regulation and Role of Adenylyl Cyclase Isoforms.” Annual Review of Pharmacology and Toxicology. **41**: 145-174.

Haselwandter, C. et al. (2015). “Self-assembly and plasticity of synaptic domains through a reaction-diffusion mechanism.” Phys. Rev. E. **92**, 032705.

Hinke, S. et al. (2012). “Anchored phosphatases modulate glucose homeostasis.” EMBO Journal. **31**(20): 3991-4004.

Landa, L. et al. (2005). “Interplay of Ca^{2+} and cAMP Signaling in the Inulin-secreting MIN6 Beta-Cell Line.” JBC. 280, 31294-31302.

Levchenko, A. et al. (2000). “Scaffold proteins may biphasically affect the levels of mitogen-activated protein kinase signaling and reduce its threshold properties.” PNAS. **97**(11): 5818-5823.

Lohse, C. et al. (2017). “Experimental and mathematical analysis of cAMP nanodomains.” PLoS One.

Mo, GC. et al. (2017). “Genetically encoded biosensors for visualizing live-cell biochemical activity at super-resolution.” Nature Methods. **14**(4): 427-434.

Murphy, J. et al. (2014). “AKAP-Anchored PKA Maintains Neuronal L-type Calcium Channel Activity and NFAT Transcriptional Signaling.” Cell Rep. **7**(5): 1577-1588.

Musheshe, N. et al. (2018). “cAMP: From Long-Range Second Messenger to Nanodomain Signalling.” Trends in Pharmacological Sciences. **39**(2): 209-222.

Musheshe, N. et al. (2018). “Targeting FRET-Based Reporters for cAMP and PKA Activity Using AKAP79.” Sensors (Basel). **18**(7): pii: E2164.

Ni, Q. et al. (2011) “Signaling Diversity of PKA Achieved Bia a Ca^{2+}-cAMP-PKA Oscillatory Circuit.” Nat Chem Biol. **7**(1): 34-40.

Oliveria, S. et al. (2003). “Imaging kinase-AKAP79-phoshpatase scaffold complexes at the plasma membrane in living cells using FRET microscopy.” J Cell Biol. **160**(1): 101-112.

Peercy, B. et al. (2015). “Modeling of Glucose-Induced cAMP Oscillations in Pancreatic Beta Cells: camp Rocks when Metabolism Rolls.” Biophysical Journal. **109**(2): 439-449.

Purkey, AM. et al. (2018). “AKAP150 Palmitoylation Regulates Synaptic Incorporation of Ca^{2+}-Permeable AMPA Receptors to Control LTP.” Cell Rep. **25**(4): 974-987.

Raoux, M. et al. (2015). “Multilevel control of glucose homeostasis by adenylyl cyclase 8.” Diabetologia. **58**(4): 749-757.

Renstrom, E. et al. (2004). “Protein kinase A-dependent and –independent stimulation of exocytosis by cAMP in mouse pancreatic beta-cells.” Journal of Physiology. **502**(1).

Sassone-Corsi, P. (2012). “The Cyclic AMP Pathway.” Cold Spring Harb Perspect Biol 4(12).

Schmitz, O. et al. (2002). “High-frequency insulin pulsatility and type 2 diabetes: from physiology and pathophysiology to clinical pharmacology.” Diabetes Matabolism. **28**(6 Suppl): 4S14-20.

Tajada, S. et al. (2017). “Distance constraints on activation of TRPV4 channels by AKAP150-bound PKCalpha in arterial myocytes.” JGP. **149**(6): 639.

Tenner, B. et al. (2016). “Optical sensors to gain mechanistic insights into signaling assemblies.” Current Opinion in Structural Biology. 203-210.

Thompson, JL. et al. (2015). “Anchoring protein AKAP79-mediated PKA phosphorylation of STIM1 determines selective activation of the ARC channel, a store-independent Orai channel.” J Physiol. **593**(3): 559-72.

Wachten, S. et al. (2010). “Distinct pools of cAMP centre on different isoforms of adenylyl cyclase in pituitary-derived GH_3B_6 cells.” J Cell Sci. 123: 95-106.

Willoughby, D. et al. (2010). “AKAP79/150 Interacts with AC8 and Regulates Ca^{2+}-dependent cAMP Synthesis in Pancreatic and Neuronal Systems.” J Biol Chem. **285**(26): 20328-20342.

Willoughby, D. et al. (2012). “A key phosphorylation site in AC8 mediates regulation of Ca^{2+}-dependent cAMP dynamics by an AC8-AKAP79-PKA signaling complex.” J Cell Sci. **125**(23): 5850-5859.

Zhang, J. et al. (2016). “Clustering and Functional Coupling of Diverse Ion Channels and Signaling Proteins Revealed by Super-resolution STORM Microscopy in Neurons.” Neuron. **92**(2): 461-478.

Zhang, X. et al. (2019). “A calcium/cAMP signaling loop at the ORAI1 mouth drives channel inactivation to shape NFAT induction.” Nature Communications. **10**: 1971.

Chapter 3

“FluoSTEPs – A versatile platform for monitoring endogenous compartmentalized signaling”

Parts of this chapter will appear in:

B. Tenner*, JZ. Zhang*, S. Mehta, B. Huang, J. Zhang, FluoSTEPs – A versatile platform for monitoring endogenous compartmentalized signaling. *In preparation for submission*

Abstract

Growing evidence suggests many essential intracellular signaling events are compartmentalized within kinetically-distinct microdomains in cells. However, current tools used to dissect the spatiotemporal dynamics within these domains typically rely on fusion proteins and overexpression of critical regulatory elements. Here we present a novel class of FRET-based biosensors FluoSTEPs (Fluorescent Sensors Targeted to Endogenous Proteins) to study compartmentalized signaling dynamics *in situ* using a split biosensor approach. By utilizing a self-complementing split GFP, CRISPR-mediated knock-in, and FRET imaging, our FluoSTEPs can simultaneously highlight endogenous microdomains and report domain-specific, real-time signaling events in live cells. We demonstrate the application of FluoSTEPs by probing cAMP signaling within clathrin microdomains and PKA activity at organization centers of PKA regulatory subunits. FluoSTEPs represent a novel toolset for studying spatiotemporal regulation within endogenous signaling architectures.

Introduction

Compartmentalization of intracellular signals by macromolecular complexes can reshape the kinetics of cellular processes and provide diversity in signaling pathways while simultaneously preserving specificity. Our understanding of such microdomain architecture of signaling networks has greatly benefited from the design of optically-based, genetically encoded biosensors (Greenwald et al. 2018). By attaching such sensors to organizational proteins of interest (POI) and introducing these fusions to living cells, researchers can monitor compartmentalized signals in real time (Tenner et al. 2016).

Despite the utility of such biosensors, this fusion strategy has drawbacks primarily stemming from unintended effects from the concomitant expression of the POI. Overexpression of enzymes or scaffolds can disrupt native signaling pathways by causing mislocalization, artificially enhancing/weakening certain fluxes, and/or affecting the stoichiometry of macromolecular interactions. This can perhaps best be illustrated in the previous chapter where overexpression of the PKA-anchoring scaffold altered signaling dynamics within the scaffold's microcompartment. Additionally, some biosensor architectures themselves include enzymatic components known to affect global signaling within the cell. For example, the Raichu-Ras sensor for measuring activity of the G-protein Ras contains active Ras within a conformational switch; however, overexpression of Ras is a hallmark of several cancers with associated, downstream signaling effects (Mochizuki et al. 2001; Fernandez-Medarde et al. 2011). Strategies have attempted to address overexpression concerns, for example, by utilizing nanobodies for highlighting endogenous, active receptors, or intrabodies to recruit biosensors to endogenous compartments (Irannejad et al. 2013; Perez-Alvarez et al. 2019). However, perturbations in trafficking and signaling due to nanobody binding, as well as issues of compartment specificity are still ever-present. Ideally, an approach that combined the strength of quantitative biosensing, specificity of genetic fusions, and minimally-invasive probing of endogenous POIs, would be valuable for dissecting compartmentalized signaling within living cells.

Here we present a versatile platform for probing endogenous microdomains termed FluoSTEPs: Fluorescent Sensors Targeted to Endogenous Proteins. By utilizing a self-complementing split GFP as a FRET donor, we designed a suite of ratiometric sensors that can be recruited and reconstituted at tagged POIs (Cabantous et al. 2005; Pedelacq et al. 2006). Generation of the functional biosensors only at a POI ensures compartment specificity, and the small size of GFP_{11}

facilitates endogenous mobilization. Efficient knock-in of GFP_{11} at a specific genomic locus via CRISPR-mediated homology-directed repair (Kamiyama et al. 2016) precludes overexpression of the POI as well as bypasses the need for knocking in an entire FRET-based sensor. We showcase FluoSTEPs by deploying the new sensors to uncover mechanisms governing sustained cyclic adenosine monophosphate (cAMP) dynamics at clathrin and differential Protein Kinase A (PKA) activity at the regulatory subunit isoform RIα.

Results and Discussion

FluoSTEP-AKAR is reconstituted and functional at microdomains of interest

In order to evaluate the design of the FluoSTEP strategy, we first sought to build a prototype sensor. We chose the well-characterized, FRET-based biosensor for Protein Kinase A (PKA) activity, AKAR4 (Depry et al. 2011), as a template for our initial design and testing. In AKAR4, PKA-specific phosphorylation on a substrate domain causes its binding with the phospho-amino acid binding domain FHA1 fused to the substrate domain, which results in a conformational change between the CFP (Cerulean) donor and YFP (cpVenus) acceptor, leading to an increase in FRET. For a FluoSTEP version of the AKAR4 reporter, we wished to design a logic-gated sensor for PKA activity in which most of the sensor exists in a nonfunctional state and would only become functional at a POI. Although an intrabody-based approach could be utilized for effective sensor recruitment, it would still be sensitive to overexpression due to the sensor existing only in a functional state. In order to install the PKA sensor with such control logic, we adopted a split super-folder GFP (sfGFP) as a FRET donor and an RFP as a FRET acceptor (Figure 3.1). The split sfGFP separates sfGFP between the 10th and 11th beta strands ($GFP_{1\text{-}10}$ and GFP_{11}), and when both nonfluorescent parts are present, efficient self-complementation occurs and GFP fluorescence is reconstituted (Pedelacq et al. 2006). We hypothesized that the small GFP_{11} fragment (16 amino acids) could easily be fused to a POI and when the $GFP_{1\text{-}10}$ fragment is present, reconstitution of a donor fluorophore occurs and gives rise to a functional FRET-based sensor only at the POI (Figure 3.1a). This domain-specific logic control could then promote ratiometric imaging for measuring compartmentalized PKA activity at endogenous protein loci.

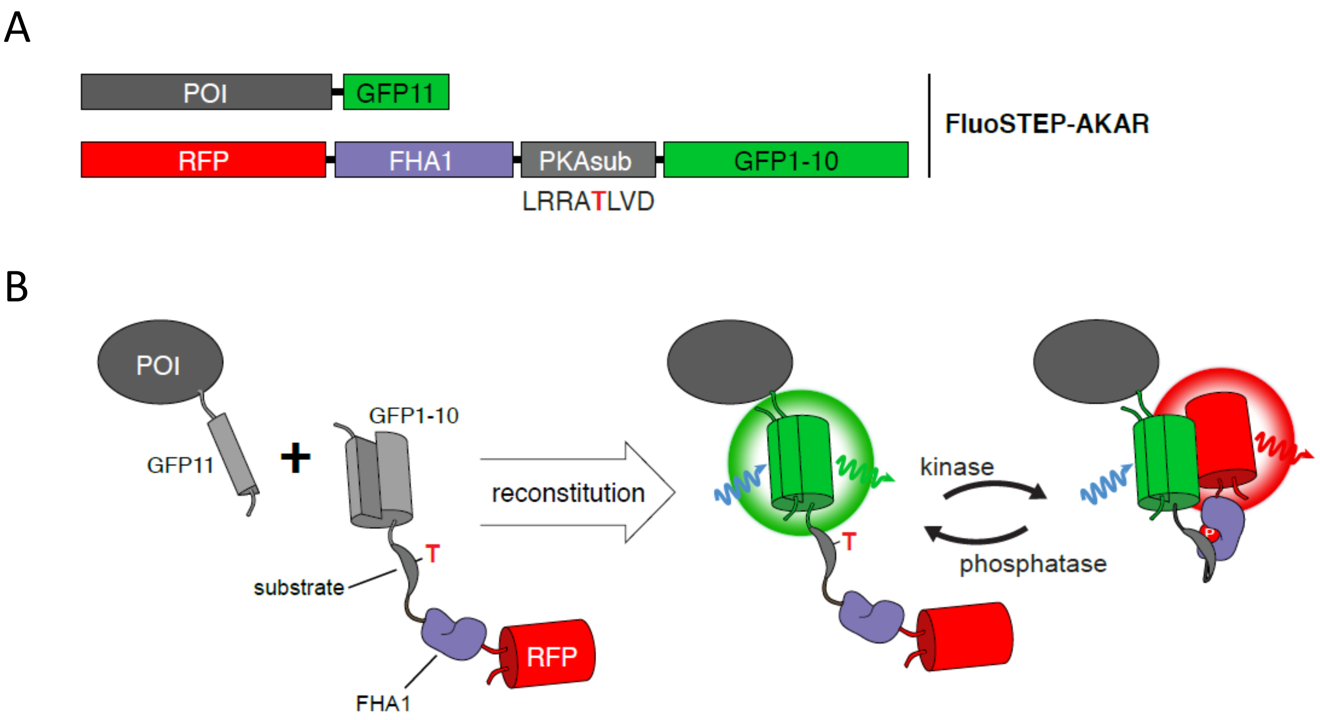

Figure 3.1 General design for the FluoSTEP platform for sensing PKA activity. (A) Two constructs comprising the FluoSTEP-AKAR design where the POI is tagged with the short GFP_{11} tag and the AKAR sensor is made from $GFP_{1\text{-}10}$, RFP, and the conformational switch (PKA substrate and phosphor-amino acid binding domain FHA1). The phosphorylation site on the PKA substrate domain is highlighted in red. (B) FluoSTEPs work by reconstituting the donor FP, in this case the split GFP, at a POI. Reconstitution of the GFP gives rise a functional FRET-based sensor so that localized kinase and phosphatase activities are translated into changes in the FRET between the donor GFP and an RFP acceptor.

To test this design, we took AKAR4 and exchanged Cerulean for GFP_{1-10} and cpVenus for mRuby2 to make a complementation-dependent green-red (GR) FRET probe (G_{1-10}-R-FluoSTEP-AKAR) (Lam et al. 2012). We also made a second version in parallel by swapping the order of GFP_{1-10} and mRuby2 (R-G_{1-10}-FluoSTEP-AKAR) due to the difference in termini locations of GFP_{1-10} and in an attempt to preserve the original, relative orientations of AKAR4's fluorescence transition dipoles' moments (Lakowicz 2006). In the presence of transiently transfected GFP_{11}-fused actin (actin-GFP_{11}) in HEK293T cells, GFP fluorescence was spontaneously reconstituted for both versions at actin (Figure 3.2a). However, only the second sensor (R-G_{1-10}-FluoSTEP-AKAR) produced a robust, inducible PKA response after the addition of forskolin (fsk, 50μM) and IBMX (100μM) (8.3% ± 0.4% change in FRET ratio, n=12), as measured by the change in the FRET ratio (RFP FRET / GFP direct) (Figure 3.2b,c). The G_{1-10}-R-FluoSTEP-AKAR sensor was noisy and did not produce a clean, monotonic PKA-induced response (n=12), so we continued to characterize the R-G_{1-10}-FluoSTEP-AKAR sensor, termed FluoSTEP-AKAR. As a negative control, the phosphorylated threonine in the PKA substrate domain was mutated to an alanine, rendering the FluoSTEP-AKAR in a perpetual "OFF" state and unresponsive to stimulation (Figure 3.3a). To test recruitment and functioning at another POI, we co-expressed clathrin-tagged GFP_{11} and FluoSTEP-AKAR and observed GFP reconstitution (Figure 3.3b). Sensor functionality was again tested with fsk/IBMX treatment, and then PKA specificity and sensor reversibility was also checked by acute addition of H89 (10μM), a potent PKA inhibitor, post-fsk/IBMX stimulation. We observed a robust PKA response to fsk/IBMX (10.5% ± 1.6% increase), followed by a return to baseline after H89, as measured by the FRET ratio (n=6) (Figure 3.3b).

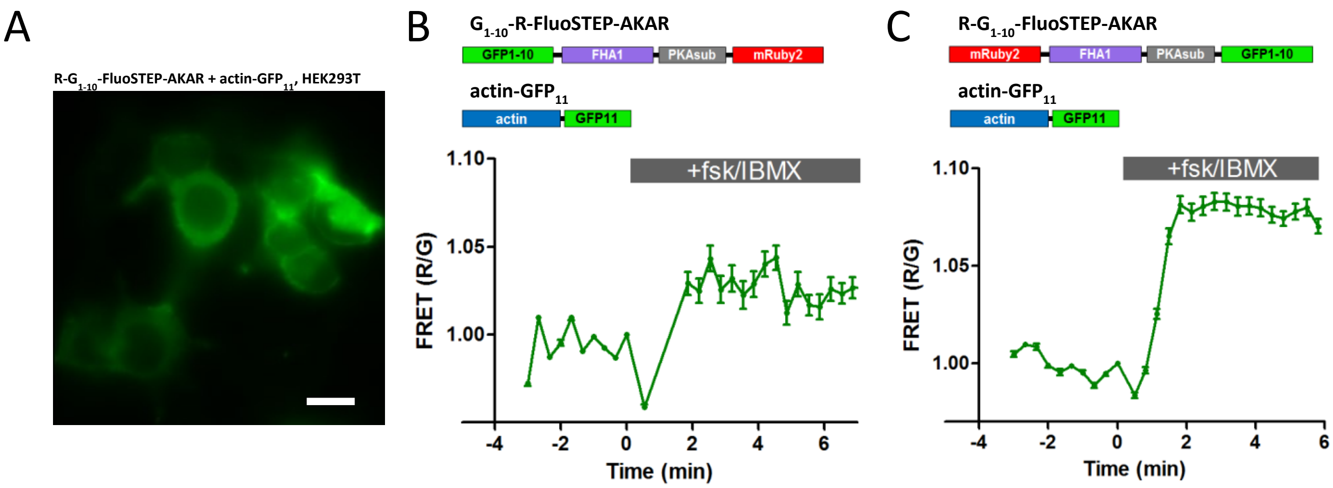

Figure 3.2 Testing of two versions of FluoSTEP-AKAR where the split GFP and mRuby2 are on different termini. (A) Image of HEK293T cells with R-G$_{1\text{-}10}$-FluoSTEP-AKAR and actin-GFP$_{11}$ co-expressed. GFP channel is shown, reconstitution is observed. (scale 10μm) (B) Schematic depicting G$_{1\text{-}10}$-R-FluoSTEP-AKAR with the split GFP on the N terminus and mRuby2 at the C terminus. Co-expression with actin-GFP$_{11}$ reconstitutes the GFP but fails to yield a clean, monotonic response to fsk (50uM, adenylyl cyclase activator) and IBMX (100uM, phosphodiesterase inhibitor) added at 0min (n=12). (C) Schematic depicting R-G$_{1\text{-}10}$-FluoSTEP-AKAR with the split GFP on the C terminus and mRuby2 at the N terminus. Co-expression with actin-GFP$_{11}$ reconstitutes the GFP yields a response to fsk (50uM) and IBMX (100uM) added at 0min (8.3% ± 0.4%, n=12). FRET (R/G) is the FRET ratio defined as the RFP FRET channel / GFP direct channel.

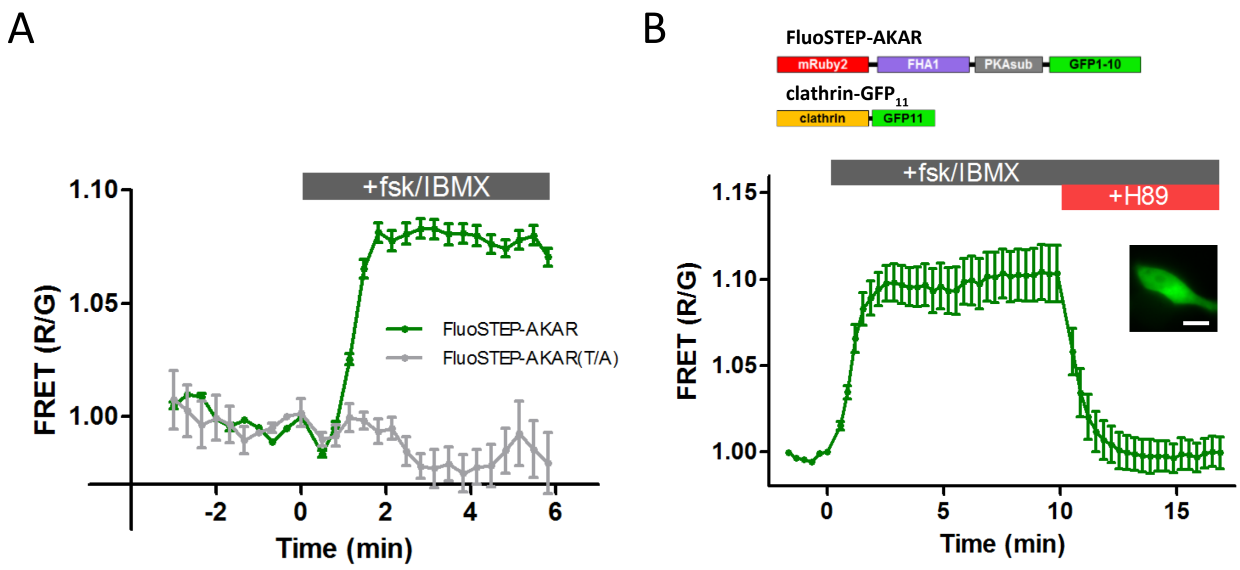

Figure 3.3 FluoSTEP-AKAR is PKA specific and reversible. (A) FluoSTEP-AKAR with the T/A phosphorylation mutation at the PKA substrate domain (gray trace) is unresponsive to PKA stimulation, compared to the wild type FluoSTEP-AKAR (green trace). (B) FluoSTEP-AKAR is functional at co-expressed GFP_{11}-tagged clathrin (inset, HEK293T, GFP channel, scale 10um). Fsk/IBMX elicited a 10.5% ± 1.6% increase in FRET, and H89 (10uM) addition to inhibit PKA returned the trace to baseline, highlighting the reversibility of the sensor (n=6).

We next attempted to increase the dynamic range of the FluoSTEP-AKAR probe in order to improve the signal-to-noise ratio (SNR). We first tried exchanging the split donor for a brighter, split version of mNeonGreen with an orthogonal FP11 tag attached to clathrin (Feng et al. 2017); however, we observed a smaller dynamic range (4.0% ± 0.3%, n=9) (Figure 3.4a), potentially due to the slightly more red-shifted spectra of mNeonGreen and thus an enhanced overlap of both fluorescent proteins' (FPs) emission spectra and a dampened change in the FRET ratio (Lam et al. 2012). GR-FRET sensors can sometimes possess smaller dynamic ranges compared to equivalent yellow-red (YR) or cyan-yellow (CY) variants (Depry et al. 2011; Ni et al. 2011; Lam et al. 2012) and so we next exchanged the donor GFP_{1-10} for two color variants derived from single-residue mutations to split sfGFP: yellow $YFP_{1\text{-}10}$ and cyan $CFP_{1\text{-}10}$ (Kamiyama et al. 2016). We created R-$Y_{1\text{-}10}$-FluoSTEP-AKAR with the $YFP_{1\text{-}10}$ as donor and mRuby2 as acceptor; co-expressed with actin-GFP_{11}, this construct yielded a small response (~4%, n=3) after fsk/IBMX addition, but suffered from drift (Figure 3.5a). For testing $CFP_{1\text{-}10}$, we instead used the yellow cpVenus from AKAR4 as the acceptor and $CFP_{1\text{-}10}$ as the donor to create a Y-$C_{1\text{-}10}$-FluoSTEP-AKAR, however, the sensor yielded a noisy response with a low dynamic range (~3%, n=3) after fsk/IBMX treatment and co-expressed with actin-GFP_{11} (Figure 3.5b). This is most likely due to the low inherent brightness of the reconstituted CFP. Future work with this construct could focus on improving the photophysical properties of the reconstituted CFP, in addition to the dynamic range, in order to expand the color palette of FluoSTEPs and promote multiplexed imaging. Lastly, we tried replacing mRuby2 with mRuby3 or mScarlet-I as an RFP acceptor for $GFP_{1\text{-}10}$ with co-expressed actin-GFP_{11} (Bajar et al. 2016; Bindels et al. 2017). While mRuby3 failed produce a discernable response (n=7) (Figure 3.6a), mScarlet-I did yield a sensor with an improved range (18.4% ± 0.4%, n=27), representing an approximate 2-fold increase over the mRuby2 version (Figure 3.6b). However, we observed that the sensor exhibited much higher direct excitation of mScarlet-I when exciting the split GFP. Further work will need to be done to validate this sensor's utility under different imaging conditions (for example by using different excitation filters), and we decided to continue with mRuby2 as the acceptor in FluoSTEP-AKAR.

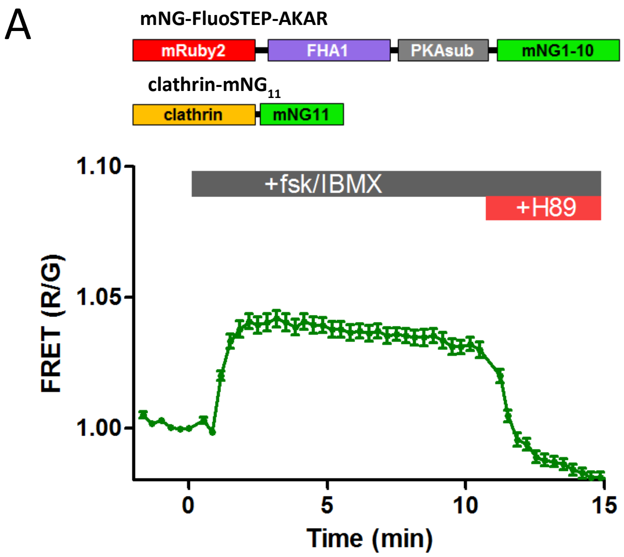

Figure 3.4 mNeonGreen-based FluoSTEP-AKAR does not improve the dynamic range of the sensor. (A) Schematic depicting mNG_{1-10} replacing GFP_{1-10} in FluoSTEP-AKAR. Fsk/IBMX triggered a modest 4.0% ± 0.3% response, H89 reversed the signal. (n=9)

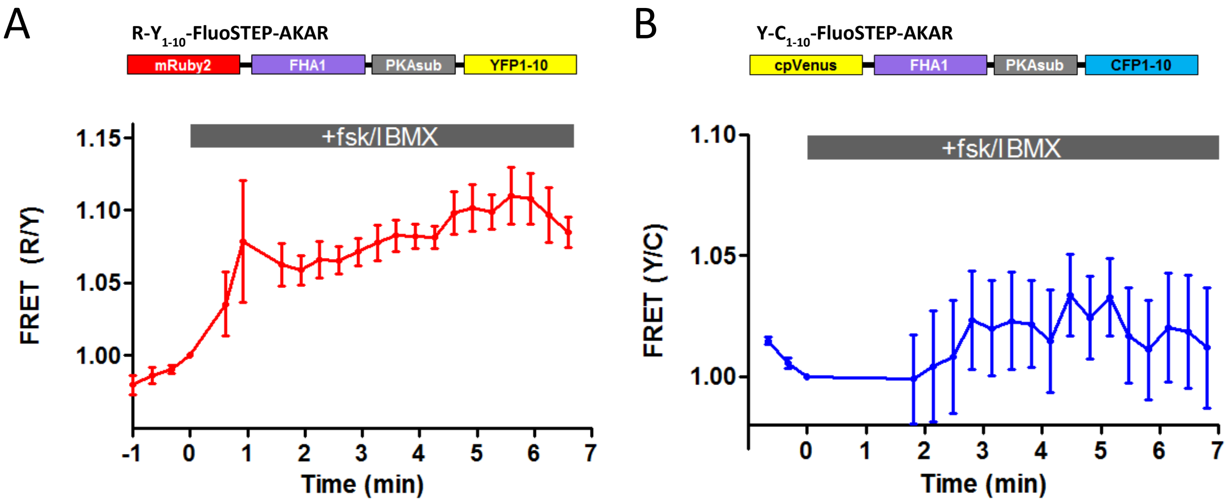

Figure 3.5 FluoSTEP-AKAR versions with split YFP or split CFP as donors do not work well. (A) Schematic of the $Y\text{-}C_{1-10}$-FluoSTEP-AKAR sensor. Fsk/IBMX failed to elicit a measurable response in the presence of actin-GFP11, further optimization will be needed. (n=3) (B) Schematic of the $R\text{-}Y_{1-10}$-FluoSTEP-AKAR sensor. Fsk/IBMX did trigger an inflection in the presence of actin-GFP11, but the baseline is drifting, preventing the sensor's utility in its current state. (n=3)

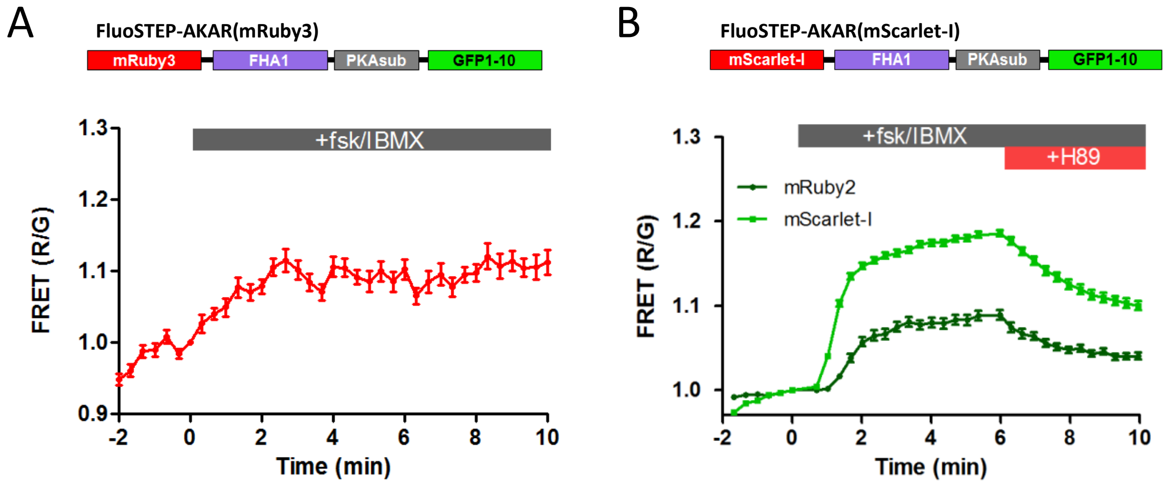

Figure 3.6 Optimizing the RFP acceptor for FluoSTEP-AKAR. (A) Schematic depicting mRuby3 in the FluoSTEP-AKAR. The FRET ratio displays drifting and fsk/IBMX fails to elicit a discernable response (. (B) Schematic depicting mScarlet-I in the FluoSTEP-AKAR Utilizing mScarlet-I does boost the dynamic range of the fsk/IBMX-induced response (18.4% ± 0.4%, n=27) (light green trace is mScarlet-I, dark green is and additional mRuby2 experiment for comparison), however, direct excitation of the RFP is extensive when exciting the split GFP, so further characterization is warranted. Actin-GFP11 is co-expressed in these comparisons.

Due to the small size of the GFP_{11} tag (16 amino acids) and the demonstration that an array of the tag could be harnessed to linearly boost the brightness of the fluorescent tag (Kamiyama et al. 2016), we hypothesized that a similar strategy could be utilized to recruit multiple copies of the FluoSTEP sensor and amplify the high-FRET state through increased intermolecular FRET (Klarenbeek et al. 2015). First, we co-expressed actin fused with an array of seven copies of GFP_{11} (actin-GFP_{11x7}) and FluoSTEP-AKAR in HeLa cells in order to see if the actin organization was affected by the interaction of many sensors. Recruitment of multiple sensors didn’t grossly alter the actin architecture (Figure 3.7a). To test the sensor’s functionality, we stimulated with fsk/IBMX. Although the brightness in the GFP channel was only 1.8x higher between co-expressed actin-GFP_{11x7} and actin-GFP_{11x1} (assessed in HeLa, n=19, 27) (Figure

3.7a), we observed an enhancement of the dynamic range by approximately 2x, indicating that an array could be used to amplify the dynamic range of the FluoSTEP (Figure 3.7b).

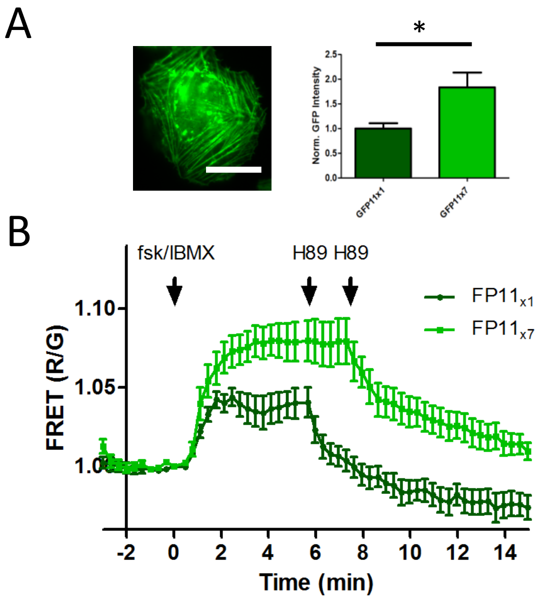

Figure 3.7 An array of GFP11 can be used to enhance the dynamic range of FluoSTEP-AKAR. (A) HeLa cell expressing actin-GFP$_{11x7}$ and FluoSTEP-AKAR. The recruitment of multiple sensors does not alter actin localization. (GFP channel, scale 10um). (B) Relative reconstituted GFP intensity (with FluoSTEP-AKAR) indicates GFP$_{11x7}$ is on average 1.8x brighter than GFP$_{11x1}$ cells (HEK293T, $p<0.05$, n=19, 27). (C) In HeLa cells, the dynamic range of FluoSTEP-AKAR was boosted in the presence of actin-GFP$_{11x7}$ vs. actin-GFP$_{11x1}$ (7.9% ± 1.2% vs. 3.9% ± 0.8%, an increase of 2-fold, n=4, 3).

FluoSTEP design can be generalized for multiple biosensors

Many FRET-based biosensors are generated based on a modular design where a signal-specific conformational switch is sandwiched between a FRET pair of FPs. This architecture facilitates the straightforward assembly of sensors for a suite of different biological activities by simply swapping out the signal-specific switch domain (Zhang et al. 2007). So next we sought to take advantage of this generalizable design and expand the arsenal of FluoSTEP sensors. In addition to PKA, many kinases are organized in macromolecular complexes or subcellularly-targeted in order to tune signaling kinetics and target specificity (Wang et al. 2011). For example, compartmentalization of Akt kinase and JNK, two kinases important within cellular survival and stress pathways, has been uncovered using FRET-based biosensors (Gao et al. 2008; Zeke et al. 2016; Zhou et al. 2015). By simply swapping out the PKA substrate domain for the phosphorylation target domains of Akt kinase and JNK, we created FluoSTEP versions of the previously published AktAR (Akt Activity Reporter) and JNKAR (JNK Activity Reporter), respectively, and tested these in the presence of actin-GFP$_{11x1}$. Upon activation of Akt via PDGF (50ng/mL), we observed a robust FRET ratio change with FluoSTEP-AktAR (7.9% ± 1.6%, n=21) (Figure 3.8a). Similarly, stimulation of JNK activity with anisomycin (5uM) yielded a delayed, stress-induced response in the FRET ratio from FluoSTEP-JNKAR (4.4% ± 1.7%, n=7) (Figure 3.8b). Other FRET-based kinase sensors utilize different sets of substrate domain and phospho-amino acid binding domain for the conformational switch. A FluoSTEP-EKAR for the Erk kinase (Erk Kinase Activity Reporter), a kinase essential in cell growth and differentiation, was also created by replacing the substrate domain (Erk substrate) and the phospho-amino acid binding domain (WW domain), as well as the addition of an extended linker (EV) in-between (Komatsu et al. 2011). A robust response was observed upon EGF (100ng/mL) addition, co-expressed with actin-GFP$_{11x1}$ (4.0% ± 0.4%, n=42) (Figure 3.8c). As negative controls, the phosphorylation mutant versions of these kinase sensors were also synthesized and were nonresponsive to stimulation (Figure 3.8a-c).

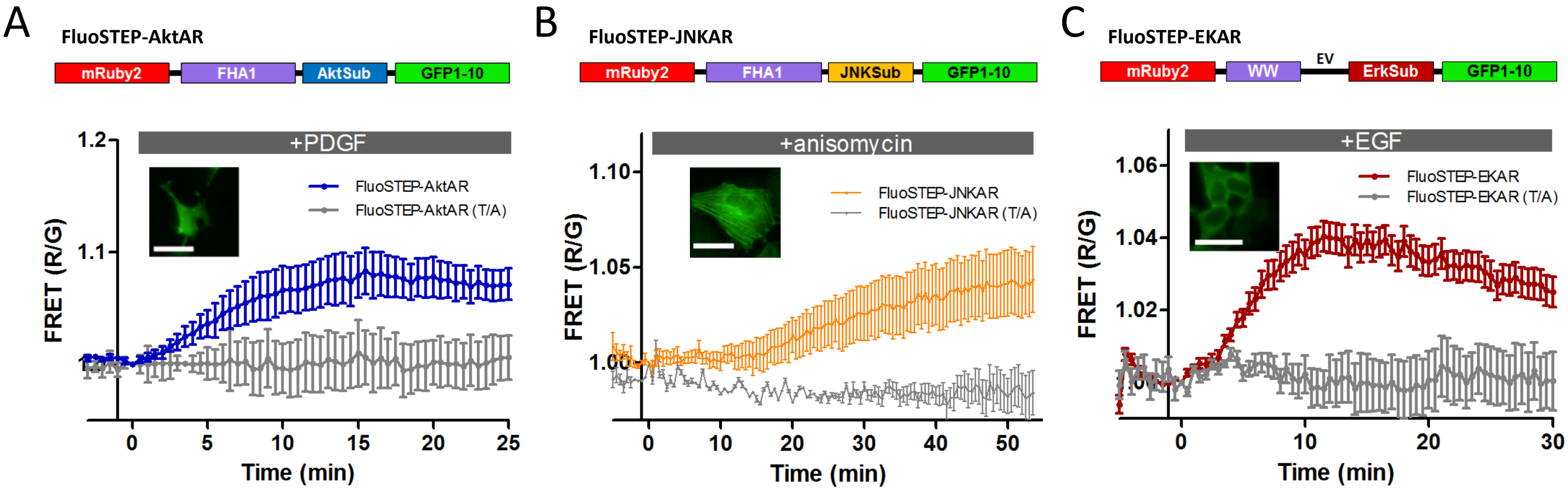

Figure 3.8 Kinase FluoSTEPs for Akt kinase, JNK, and Erk kinase. (A) Schematic of FluoSTEP-AktAR. Blue trace is FluoSTEP-AktAR, gray is phosph. mutant. FluoSTEP-AktAR responds with co-expressed actin-GFP_{11} upon PDGF (50ng/mL) stimulation (7.9% ± 1.6%, n=21, 3T3 cells, scale 10um). (B) Schematic of FluoSTEP-JNKAR. Orange trace is FluoSTEP-JNKAR, gray is phosph. mutant. FluoSTEP-JNKAR responds with co-expressed actin-GFP_{11} upon anisomycin (5uM) stimulation (4.4% ± 1.7%, n=7, HeLa cells, scale 10um). (C) Schematic of FluoSTEP-EKAR. Red trace is FluoSTEP-EKAR, gray is phosph. mutant. FluoSTEP-EKAR responds with co-expressed actin-GFP_{11} upon EGF (100ng/mL) stimulation (4.0% ± 0.4%, n=42, HEK293T cells, scale 10um).

As mentioned previously, some FRET-based biosensors incorporate enzymatic components within their design architecture. In many contexts, this is unfavorable due to unwanted effects from overexpression. Thus, we hypothesize FluoSTEPs could help untangle this dependence by uncoupling the expression of the enzymatic component from the rest of the sensor and produce functional sensors only when both parts are present. As a prototype, we turned our attention to the RhoA-DORA sensor which measures the activation of RhoA, a small GTPase important in cytoskeletal regulation, by transducing a binding event between GTP-bound RhoA and the interactor domain cpPKN into an increase in FRET (van Unen et al. 2015). We created our own FluoSTEP version by replacing the FPs with split GFP and mRuby2 so that RhoA was tagged with the small GFP$_{11}$ and the remainder of the sensor (cpPKN-mRuby2-EV-GFP$_{1\text{-}10}$) incorporated GFP$_{1\text{-}10}$, thus splitting the sensor into two separate parts (Figure 3.9a). By expressing both parts, we successfully reconstituted the donor GFP. Upon stimulating RhoA activity with histamine (dose), the activated FluoSTEP-RhoA-DORA sensor responded robustly (9.0% ± 1.5%, n=20), compared to an inactivated mutant version (Figure 3.9a). Interestingly, the FluoSTEP architecture for this sensor reversed the activity-induced FRET change (from a positive to a negative change in the FRET ratio), likely due to differences in dipole orientation between the original and our FluoSTEP version, and so we inversed the FRET ratio and plotted the GFP direct channel divided by the RFP FRET channel in order to observe a positive trace. The design for FluoSTEP-RhoA-DORA could potentially be adapted for endogenous tagging of RhoA with GFP$_{11}$ and thus offer a minimally-perturbative alternative for monitoring RhoA activity.

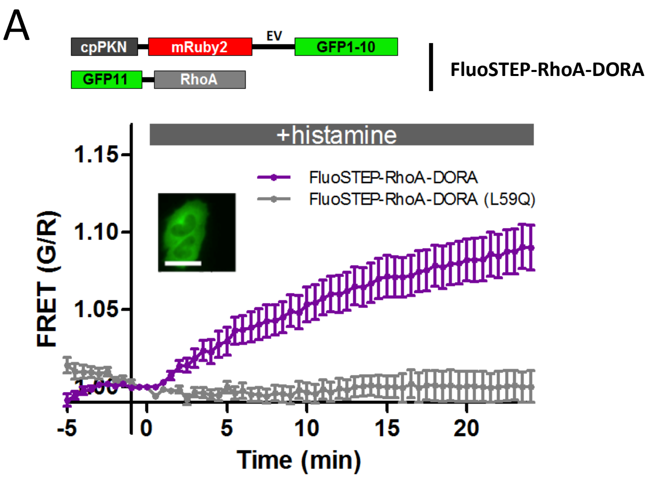

Figure 3.9 FluoSTEP for RhoA activity. (A) Schematic of FluoSTEP-RhoA-DORA. Purple trace is FluoSTEP-RhoA-DORA, gray is inactivated mutant. FluoSTEP-RhoA-DORA reconstitutes and responds to histamine (100uM) stimulation (9.0% ± 1.5%, n=20, HeLa cells, scale 10um).

Finally, we sought to extend the FluoSTEP framework to second messenger detection. Cyclic adenosine monophosphate (cAMP), the upstream regulator of PKA, is found to exert its diverse regulatory roles through compartmentalization (Calebiro et al. 2014). Most cAMP sensors work by translating a cAMP-binding event into a conformational change of a single domain (Violin et al. 2007; Klarenbeek et al. 2015), which modulates FRET between flanking FPs. We tested two different cAMP-binding switches between mRuby2 and GFP_{1-10} derived from the cAMP-binding domains of Epac isoforms ($Epac2B^{285-443}$ and $Epac1^{149-881}$), and found only the longer switch produced a response (5.9% ± 0.6%, n=10) upon fsk/IBMX addition and co-expressed actin-GFP_{11} (Violin et al. 2007; Nikolaev et al. 2004) (Figure 3.10a). The FluoSTEP version (FluoSTEP-ICUE: Indicator of cAMP Using Epac) retains its negative FRET reporter behavior from the previous cAMP sensor (binding of cAMP lead to a decrease in the FRET ratio and thus we plotted GFP direct over RFP FRET for a positive trace) and was utilized in the following experiments. In addition, we also demonstrated that amplification of the dynamic range could be achieved by again using an array of the GFP_{11} tag (1.7-fold improvement) (Figure 3.10b).

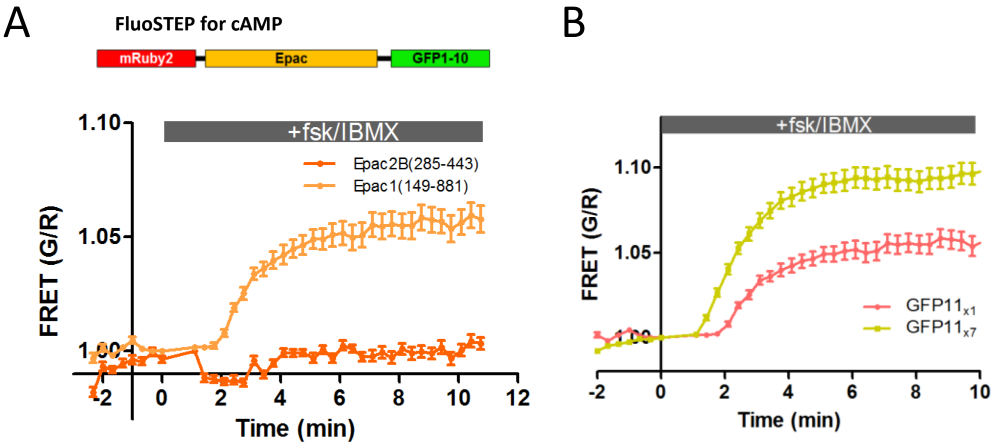

Figure 3.10 A FluoSTEP for cAMP. (A) Schematic of a generalized FluoSTEP for cAMP with single-chain conformational switch derived from the Epac family. Light orange trace is using Epac2B(285-443) and dark orange is using Epac1(149-881). Robust response from the Epac1-based FluoSTEP was observed in the presence of co-expressed actin-GFP$_{11}$ (5.9% ± 0.6%, n=10, HEK293T). (B) Amplification of the dynamic range was observed when using an array of seven repeats of the GFP$_{11}$ tag on actin for the FluoSTEP-ICUE probe, compared to a single copy (GFP$_{11x1}$) (10.0% ± 0.6% vs. 5.8% ± 0.6%; 1.7x improvement, n=17,10, HEK293T).

Endogenous signaling compartments are accessible by FluoSTEPs

In order to test the compartment-specific FluoSTEP sensors in an endogenous context, we sought to knock-in GFP$_{11}$ at specific genomic loci in HEK293T cells. Due to the small size of GFP$_{11}$, knock-in via CRISPR and HDR with a single-stranded oligonucleotide donor is efficient and versatile and can theoretically be extended to multiple genomic loci of interest (Kamiyama et al. 2016; Mali et al. 2013). In order to test the FluoSTEP platform with a POI at the endogenous level, we knocked-in GFP$_{11}$ into the SEC61B locus which codes for one of the subunits in the Sec61 protein translocon at the ER on the cytosolic face (Wiertz et al. 1996). By expressing the FluoSTEP-AKAR sensor, we observed perinuclear GFP fluorescence (Figure 3.11a). We monitored the FRET ratio and noticed a positive drift, possibly due to donor GFP photobleaching and/or photochromic behavior of mRuby2 (Bindels et al. 2017; Botman et al. 2019). However, fsk/IBMX addition triggered an inflection in the trace, indicating a response, albeit weak, which was reversed upon later H89 treatment (n=28) (Figure 3.11b). FluoSTEP-ICUE was also tested in this context and yielded a robust response to fsk/IBMX addition (Figure 3.11c). Taken together, this suggests that the FluoSTEP platform can be used for monitoring signaling dynamics at the native loci of a target protein at the endogenous level.

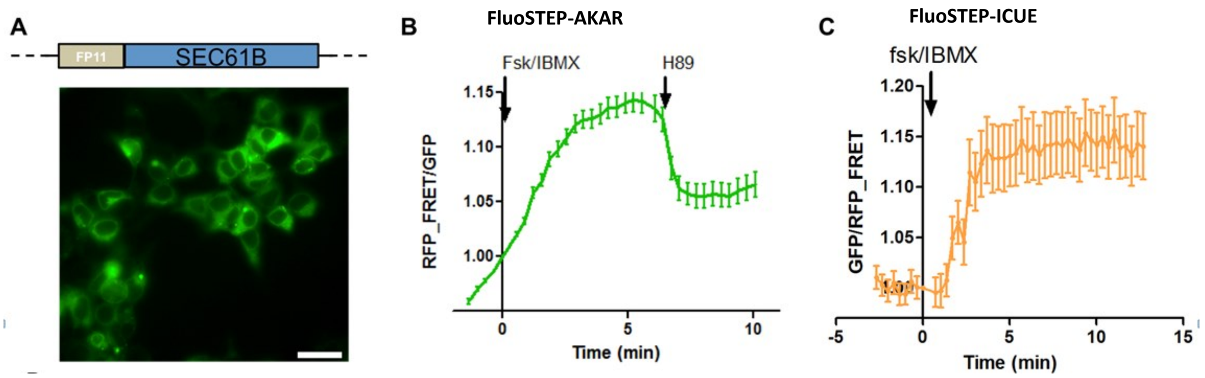

Figure 3.11 FluoSTEPs can monitor signaling at the endogenous Sec61 translocon at the ER. (A) Knock-in and reconstitution of GFP at Sec61B in HEK293T (scale 20um). (B) FluoSTEP-AKAR can monitor PKA signaling at Sec61B, as indicated by the inflection but suffers from drift, however, it maintains its reversibility (n=28). (C) FluoSTEP-ICUE can monitor cAMP signaling at Sec61B (n=10).

Transmembrane adenylyl cyclases regulate sustained cAMP production at clathrin

Clathrin, a scaffold protein important in the formation and endocytosis/exocytosis of vesicles, modulates cAMP signaling by promoting internalization of G-coupled receptors and mediating receptor recycling (Kaksonen et al. 2018). It has also been suggested that GPCR internalization arbitrates a distinct secondary phase of cAMP signaling from endosomes (Calebiro et al. 2010), and so we wished to take a closer look at compartmentalized cAMP dynamics at the clathrin microdomain. We knocked-in the GFP_{11} tag into the gene that encodes for the clathrin light chain A (CLTA) in HEK293T cells and found that the donor GFP was reconstituted when we expressed FluoSTEP-AKAR. Distinct clathrin-coated pits were observed, indicating correct localization of FluoSTEP-AKAR (Figure 3.12a). By treating cells with fsk/IBMX, we reliably detected a rapid increase in PKA activity within the clathrin microdomain (12.5% ± 0.7%, n=33) (Figure 3.12b). Sensor reversibility was checked with subsequent addition of H89 and we observed the FRET return to baseline. To monitor microdomain-specific cAMP, we utilized the FluoSTEP-ICUE sensor. Treatment with fsk/IBMX successfully triggered a rapid FRET change and demonstrated the utility of FluoSTEPs to measure cAMP at clathrin-coated pits (n=12) (Figure 3.12c).

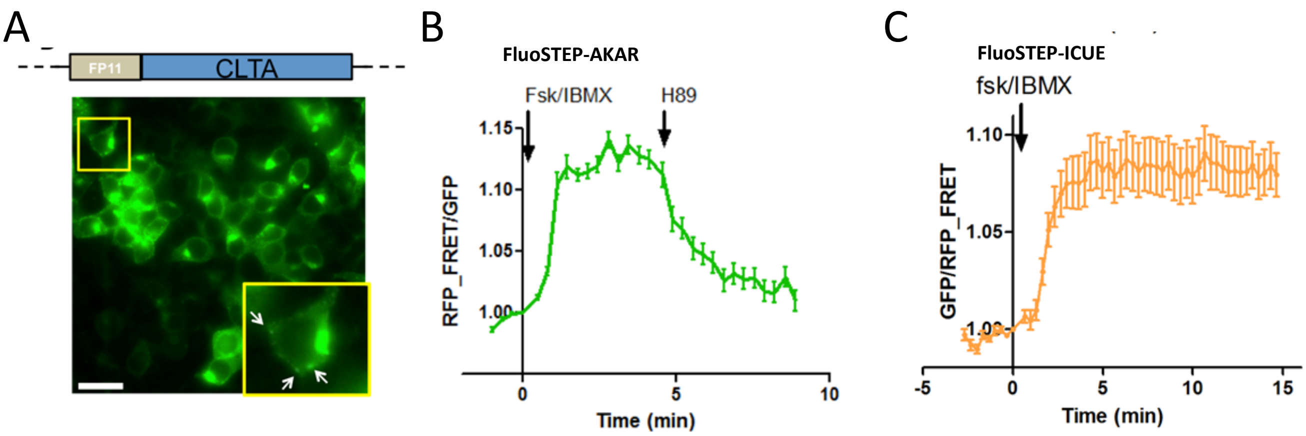

Figure 3.12 FluoSTEPs can monitor signaling at endogenous clathrin. (A) Knock-in and reconstitution of GFP at clathrin in HEK293T (scale 20um). Clathrin-coated pits are visible, see inset. (B) FluoSTEP-AKAR can monitor PKA signaling at clathrin as indicated by a robust response after fsk/IBMX, and maintains reversibility (12.5% ± 0.7%, n=33). (C) FluoSTEP-ICUE can monitor cAMP signaling at clathrin (n=12).

To probe the clathrin-specific cAMP dynamics under physiologically-relevant conditions, we expressed FluoSTEP-ICUE and stimulated the CLTA-FP11 cells with isoproterenol (iso, 10uM), a potent beta adrenergic receptor agonist, eventually followed by a maximizing dose of fsk/IBMX for normalization. Isoproterenol induced a robust, sustained response (approx. 30% of max, approx. SAM20 = 0.9, n=15; SAM20 = $(R_{20}-R_0) / (R_{max}-R_0)$ where R_{20} is ratio at 20min post stimulation, R_{max} is maximum ratio occurring within 20min, R_0 is ratio at time=0min) measured by whole-cell fluorescence, illustrating the sensitivity of FluoSTEPs under submaximal stimulation conditions (Figure 3.13a). We also detected internalization of clathrin-coated pits, demonstrating that the presence of FluoSTEP-ICUE does not block this process (Figure 3.13c) (Kaksonen et al. 2018). To compare the clathrin microdomain-specific cAMP dynamics with bulk cAMP signals, we expressed a CY-FRET cAMP probe with the same Epac-based switch domain (Violin et al. 2007) either untargeted or targeted to the general plasma membrane (PM) via the lyn kinase palmitoylation sequence (lyn-ICUE). Upon isoproterenol stimulation, the cAMP signal for both untargeted and PM-targeted ICUE rose sharply (approx. 50% of max, SAM20 = 0.45, n=25,28) before decreasing and setting at a sub-maximum steady-state (Figure 3.13a). This indicates that iso-stimulated cAMP in the cytoplasm and general PM is transient, supporting previous reports of cAMP clearance due to the desensitization of canonical beta adrenergic receptor signaling (Violin et al. 2007). To verify the sustained cAMP response at clathrin versus the transient dynamics at the PM wasn't due to an artifact of the FluoSTEP probe, we reconstituted FluoSTEP-ICUE at the PM by co-expressing FP11 tagged to a lyn-fused protein and observed an expected transient response upon iso treatment (n=8, SAM20 = 0.45).

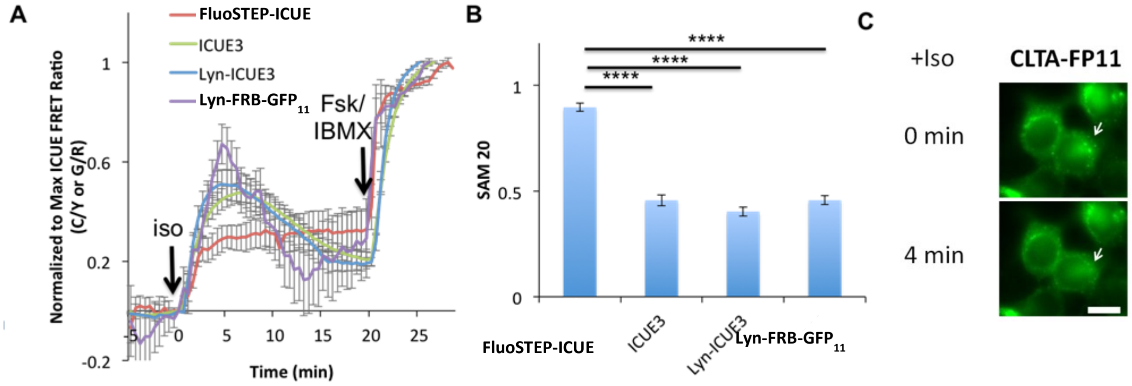

Figure 3.13 cAMP at endogenous clathrin is sustained upon beta adrenergic stimulation. (A) Traces showing cAMP generation upon iso stimulation, normalized to a maximizing dose of fsk/IBMX. Red trace is FluoSTEP-ICUE, green is untargeted ICUE, blue is plasma membrane-targeted ICUE, and purple is the FluoSTEP control at the PM. (B) SAM20 (ratio measurement of sustainability) for the traces in A. FluoSTEP-ICUE displays a more sustained cAMP response at endogenous clathrin, compared to the other targeted sensors. (n=15, 25, 28, 8) ($p<0.05$) (C) Iso stimulation triggers internalization of clathrin-coated pits, indicating that the FluoSTEP does not disrupt the physiology (scale 10um).

We hypothesized that sustained cAMP signaling at the clathrin microdomain might be due to continuous signaling via the beta adrenergic receptor, and so we treated cells 35min post-stimulation with an acute dose of 2-propranolol, a beta adrenergic receptor antagonist (10uM). The general PM cAMP decreased and approached a pre-iso stimulated baseline (n=18), however, for the clathrin microdomain-specific signal, cAMP dynamics were unaffected (n=13), indicating that the sustained cAMP response in the clathrin microdomain is not dependent on the active receptor (Figure 3.14a). cAMP signaling can be compartmentalized by the organization of adenylyl cyclases (ACs) and phosphodiesterases (PDEs) within the cell (Calebiro et al. 2014). To test the regulatory role of these enzymes, we acutely inhibited either PDEs with IBMX (100uM) or transmembrane ACs (tmACs) with 2’,3’-dideoxyadenosine (ddAdo, 100uM) post-iso stimulation. Interestingly, we found that PDE inhibition potentiated cAMP at the general PM but had little effect at clathrin (n=23,21). On the other hand, tmAC inhibition sharply reduced cAMP levels back to a pre-stimulation baseline at clathrin but only had minimal effect on the general PM cAMP signal (Figure 3.14b) (n=25,25). Taken together, this suggests that active tmACs, in the absence of the active receptor, are responsible for the sustained, compartmentalized cAMP dynamics at clathrin while a shifted balance towards high PDE activity is responsible for the transient cAMP signal at the general PM.

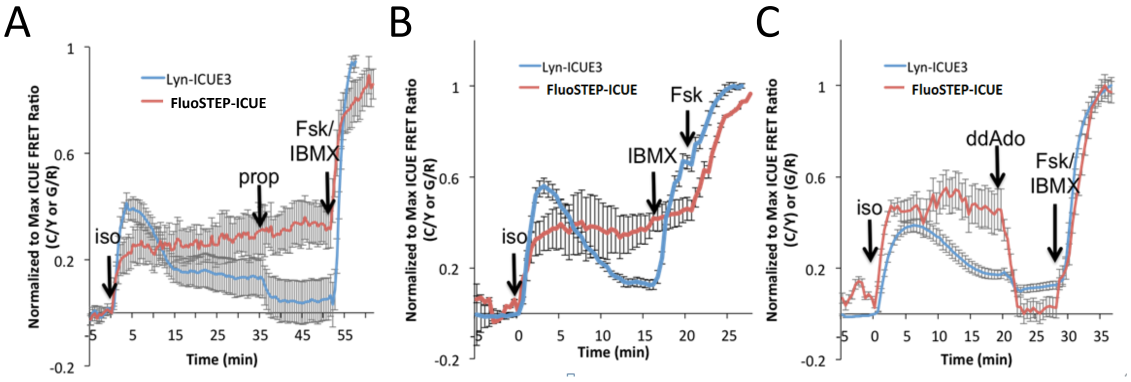

Figure 3.14 tmACs are responsible for the sustained cAMP at endogenous clathrin. (A) Traces comparing ICUE at the PM (lyn target, blue trace) vs. FluoSTEP-ICUE (shown here as the red trace) upon propranolol treatment. The clathrin cAMP microdomain is insensitive to the beta blocker. (B) FluoSTEP-ICUE also demonstrates that the clathrin cAMP microdomain is insensitive to general phosphodiesterase inhibition. (C) tmAC inhibition by ddAdo decreases the clathrin-specific cAMP microdomain signal.

PKA regulatory subunit RIα spatially modulates cAMP and PKA activity within cells

PKA signaling is compartmentalized via interactions between PKA's regulatory subunits and various scaffold proteins, such as A-Kinase Anchoring Proteins (AKAPs) (Greenwald et al. 2012). Although cooperation between the regulatory subunit RII isoforms and AKAPs have been extensively studied (Wong et al. 2004), much less is understood about the compartmentalizing role of RI isoforms. Recently it was demonstrated that the RIα isoform organizes into punctate structures in the cytoplasm, which possessed sensitivity to PKA activity (Day et al. 2011), and so we wished to deploy FluoSTEPs to study this localized signaling domain at the endogenous context. To start, we successfully knocked-in GFP$_{11x1}$ into the RIα locus in HEK293T, transiently transfected GFP$_{1-10}$, and observed endogenous RIα, both in puncta and diffuse, distributed throughout the cytoplasm (Figure 3.15a). In order to probe RIα-localized PKA activity, we transfected FluoSTEP-AKAR in the RIα-GFP11$_{x1}$ stable cells and stimulated AC activity with fsk. Interestingly, we found differential PKA sensitivity between punctate and diffusively-distributed RIα. While PKA activity modulation was observed in the diffuse RIα, PKA activity at the punctate structures did not respond to fsk treatment (Figure 3.15b). We then looked upstream at stimulated cAMP production in the two compartments with FluoSTEP-ICUE and observed a similar difference (Figure 3.15c). Taken together, this suggests that localized cAMP/PKA signaling at these RIα puncta is spatiotemporally regulated and further work needs to be done to elucidate the compartmentalization mechanism.

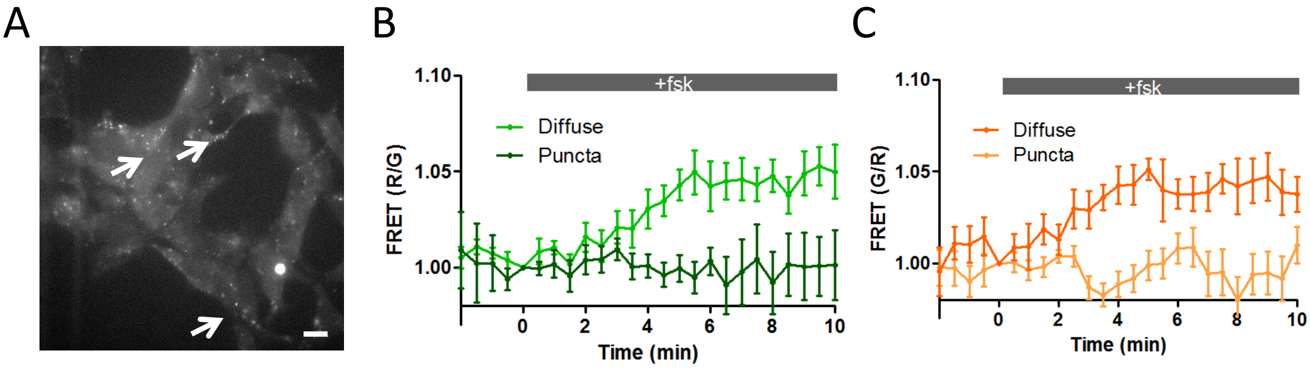

Figure 3.15 PKA regulatory subunit R1α spatially modulates cAMP and PKA. (A) Image of endogenous R1alpha in HEK293T (scale 10um). R1alpha exists in both puncta and diffuse regions about the cell. (B) Differential PKA activity at the R1alpha puncta and diffuse locations is seen in fsk stimulated conditions (dark green puncta, light green diffuse) (n=8,8). (C) The same insensitivity is seen with fsk-triggered cAMP production (light orange puncta, dark orange diffuse) (n=8,8).

Conclusion

Here we present FluoSTEP, an adaptable biosensor framework for monitoring compartmentalized signaling at endogenous cellular locations, and deploy it to study cAMP/PKA signaling microdomains. Complementation and functional reconstitution of the sensors at endogenously tagged proteins imparts a control logic, and thus domain specificity, while the ratiometric readout allows quantitative comparisons of localized signaling. Despite the demonstrated advantages of the platform, potential obstacles such as the low dynamic range of the sensors and the dependence on the endogenous expression must be considered. While enhanced FP reconstitution at endogenous POIs and an amplified dynamic range using an array of the GFP_{11} tag has been demonstrated, future development and optimization of FluoSTEPs will include linkers and additional FP screening. Furthermore, by extending the FluoSTEPS to utilize orthogonal, multicolored FP variants, several sensors may be multiplexed and simultaneously report differential compartmentalized signaling in the same cell. FluoSTEPs offers researchers a minimally perturbative method of observing microdomain-specific signaling at an endogenous level in order to better understand spatiotemporal regulation of biochemical networks.

Materials and Methods

Biosensor Construction

All assembly of constructs was performed using Gibson Assembly (NEB 2x High Fidelity Master Mix). To make FluoSTEP-AKAR, the PKA switch domain from AKAR4 and mRuby2 were PCR amplified and inserted into a pcDNA3.1+ (Invitrogen) vector containing GFP_{1-10}. Color variants of FluoSTEP-AKAR to optimize the dynamic range were made similarly by PCR amplification of the FP to swap in and the remainder of the FluoSTEP-AKAR minus FP to swap out. Assembly of other FluoSTEP versions was made by simply swapping out the switch domain between GFP_{1-10} and mRuby2 from FluoSTEP-AKAR for switch domains from CKAR to make FluoSTEP-CKAR, AktAR to make FluoSTEP-AktAR, and EKAR2.3 to make FluoSTEP-EKAR, via PCR amplification and Gibson Assembly. FluoSTEP-RhoA-DORA sensor parts were assembled by PCR amplification of RhoA with extension PCR to add GFP_{11} and cpPKN, mRuby2, and GFP_{1-10} for the other parts.

Cell Culture and Transfection

HeLa and HEK293T cells were cultured in Dulbecco modified Eagle medium (DMEM; Gibco) containing 1 g/L glucose and supplemented with 10% (v/v) fetal bovine serum (FBS, Sigma) and 1% (v/v) penicillin-streptomycin (Pen-Strep, Sigma-Aldrich). NIH3T3 cells were cultured in DMEM (Gibco) containing 1 g/L glucose and supplemented with 10% (v/v) fetal calf serum (FCS) and 1% (v/v) Pen-Strep (Sigma-Aldrich). All cells were maintained in a humidified incubator at 37°C with a 5% CO_2 atmosphere. Prior to transfection, cells were plated onto sterile 35-mm glass-bottomed dishes and grown to 50–70% confluence. Cells were then transfected using Lipofectamine 2000 (Invitrogen) or PolyJet (SignaGen Laboratories) and grown an additional 24 h (HeLa, HEK293T) before imaging. NIH3T3 cells were changed to serum-free DMEM immediately prior to transfection and serum-starved for 24 h before imaging.

CRISPR-mediated knock-in for stable GFP_{11} cell lines

For the knock-in experiments, 200 ng of Cas9+sgRNA vector (designed with px330 for SEC61B and CLTA, and px459 for RIα) and 400 ng of an oligonucleotide donor DNA were transfected to HEK293FT cells per 24-well plate (Eppendorf). For CLTA and SEC61B, transient transfection of $GFP_{1\text{-}10}$ and FACS enrichment for GFP+ cells were performed, followed by a negative sort two weeks later to select against stable incorporation of $GFP_{1\text{-}10}$. For RIα, single-cell deposition of transfected cells with Cas9+sgRNA into 96-well plates was performed. Genomic DNA was extracted from cells and sequenced to confirm knock-in.

Time-lapse fluorescence imaging

Cells were washed twice with Hank's balanced salt solution (HBSS, Gibco) and subsequently imaged in HBSS in the dark at 37°C. Forskolin (Fsk; Calbiochem), 3-isobutyl-1-methylxanthine (IBMX; Sigma), epidermal growth factor (EGF; Sigma-Aldrich), and histamine (Sigma-Aldrich) were added as indicated. Images were acquired on a Zeiss AxioObserver Z1 microscope (Carl Zeiss) equipped with a 40x/1.3 NA objective and a Photometrics Evolve 512 EMCCD (Photometrics, Tucson, AZ) controlled by METAFLUOR 7.7 software (Molecular Devices). GFP imaging was performed using a 480DF30 excitation filter and 505DRLP dichroic mirror and a 535DF45 emission filter; GFP-RFP FRET imaging was performed using a 480DF30 excitation filter and 600DRLP dichroic mirror and a 653DF95 emission filter; RFP intensity was imaged using a 568DF55 excitation filter, a 600DRLP dichroic mirror, and a 653DF95 emission filter; and YFP intensity was imaged using a 495DF40 excitation filter, a 515DRLP dichroic mirror, and a 535DF25 emission filter. All filter sets were alternated by a Lambda 10–2 filter-changer (Sutter Instruments). Exposure times ranged between 50 and 500 ms and images were acquired every 15–30 s.

References

Bajar, B. et al. (2016). “Improving brightness and photostability of green and red fluorescent proteins for live cell imaging and FRET reporting.” Scientific Reports. **6**: 20889.

Bindels, D. et al. (2017) “mScarlet: a bright monomeric red fluorescent protein for cellular imaging.” Nature Methods. **14**: 53-56.

Botman, D. et al. (2019). “In vivo characterization of fluorescent proteins in budding yeast.” Scientific Reports. **9**: 2234.

Cabantous, S. et al. (2005). “Protein tagging and detection with engineered self-assembling fragments of green fluorescent protein.” Nature Biotechnology. **23**(1): 102-7.

Calebiro, D. et al. (2010). “Signaling by internalized G-protein-coupled receptors.” Trends in Pharmacological Sciences. **31**(5): 221-228.

Calebiro, D. et al. (2014). “cAMP signaling microdomains and their observation by optical methods.” Front. Cell. Neurosci.

Day, M. et al. (2011). “Isoform-specific targeting of PKA to multivesicular bodies.” JCB. **193**(2): 347.

Depry, C. et al. (2011). “Visualization of PKA activity in plasma membrane microdomains.” Mol Biosyst. **7**(1): 52-8.

Feng, S. et al. (2017). “Improved split fluorescent proteins for endogenous protein labeling.” Nature Communications. **8**: 370.

Fernandez-Madarde, A. et al. (2011). “Ras in Cancer and Developmental Diseases.” Genes Cancer. **2**(3): 344-358.

Gao, X. et al. (2008). “Spatiotemporal Analysis of Differential Akt Regulation in Plasma Membrane Microdomains.” Mol Biol Cell. **19**(10): 4366-4373.

Greenwald, E. et al. (2012). “Bigger, better, faster: principles and models of AKAP signaling.” J Cardiovasc Pharmacology. **58**(5): 462-469.

Greenwald, E. et al. (2018). “Genetically Encoded Fluorescent Biosensors Illuminate Spatiotemporal Regulation of Signaling Networks.” Chemical Review. **118**(24): 11707-11794.

Irannejad, R. et al. (2013). “Conformation biosensors reveal adrenoceptor signalling from endosomes.” Nature. **495**(7442).

Kaksonen, M. et al. (2018). “Mechanisms of clathrin-mediated endocytosis.” Nature Reviews Molecular Cell Biology. **19**: 313-326.

Kamiyama, D. et al. (2016). “Versatile protein tagging in cells with split fluorescent protein.” Nature Communications. **7**: 11046.

Klarenbeek, J. et al. (2015). “Fourth-generation epac-based FRET sensors for cAMP feature exceptional brightness, photostability and dynamic range: characterization of dedicated sensors for FLIM, for ratiometry and with high affinity.” PLoS One. **10**(4): e0122513.

Komatsu, N. et al. (2011). “Development of an optimized backbone of FRET biosensors for kinases and GTPases.” Mol Biol Cell. **22**(23): 4647-4656.

Lakowicz, J. (2006). Principles of Fluorescence Spectroscopy.

Lam, A. et al. (2012). “Improving FRET dynamic range with bright green and red fluorescent proteins.” Nature Methods. **9**: 1005-1012.

Mali, P. et al. (2013). “RNA-guided human genome engineering via Cas9.” Science. **339**(6121): 823-6.

Mochizuki, N. et al. (2001). “Spatio-temporal images of growth-factor-induced activation of Ras and Rap1.” Nature. **411**: 1065-1068.

Ni, Q. et al. (2011) “Signaling Diversity of PKA Achieved Via a Ca^{2+}-cAMP-PKA Oscillatory Circuit.” Nat Chem Biol. **7**(1): 34-40.

Nikolaev, V. et al. (2004). “Novel Single Chain cAMP Sensors for Receptor-induced Signal Propagation.” JBC. 279: 37215-37218.

Pedelacq, J. et al. (2006). “Engineering and characterization of a superfolder green fluorescent protein.” Nature Biotechnology. **24**: 79-88.

Perez-Alvarez, A. et al. (2019). “Freeze-frame imaging of synaptic activity using SynTagMA.” bioRxiv.

Tenner, B. et al. (2016). “Optical sensors to gain mechanistic insights into signaling assemblies.” Current Opinion in Structural Biology. 203-210.

Van Unen, J. et al. (2015). “Plasma membrane restricted RhoGEF activity is sufficient for RhoA-mediated actin polymerization.” Scientific Reports. 5: 14693.

Violin, J. et al. (2007). “Beta2-Adrenergic Receptor Signaling and Desensitization Elucided by Quantitative Modeling of Real Time cAMP Dynamics.” JBC. 283: 2949-2961.

Wang, Y. et al. (2011). “Spatial Phosphoprotein Profiling Reveals a Compartmentalized Extracellular Signal-regulated Kinase Switch Governing Neurite Growth and Retraction.” JBC. **286**: 18190-18201.

Wiertz, E. et al. (1996). “Sec61-mediated transfer of a membrane protein from the endoplasmic reticulum to the proteasome for destruction.” Nature. **384**: 432-438.

Wong, W. et al. (2004). “AKAP signalling complexes: focal points in space and time.” Nat Rev Mol Cell Biol. **5**(12): 959-70.

Zeke, A. et al. (2016). “JNK Signaling: Regulation and Functions Based on Complex Protein-Protein Partnerships.” American Society for Microbiology Journals. Rev 80: 793-835.

Zhang, J. et al. (2007). “FRET-based biosensors for protein kinases: illuminated the kinome.” Molecular BioSystems. **3**: 759-765.

Zhou, X. et al. (2015). “Visualizing Dynamic Activities of Signaling Enzymes Using Genetically Encodable FRET-Based Biosensors: From Designs to Applications.” Methods Enzymology. 504: 317-340.

Chapter 4

“Design and optimization of genetically encoded biosensors for multiplexed signaling interrogation”

Parts of this chapter appear in:

B. Ross**, B. Tenner**, M. Markwardt, A. Zviman, G. Shi, J. Kerr, N. Snell, J. McFarland, J. Mauban, C. Ward, M. Rizzo, J. Zhang. Single-color, ratiometric biosensors for detecting signaling activities in live cells. **eLife** (2018) 7:e35458.

and

S. Mehta*, Y. Zhang*, R. Roth*, JF. Zhang, A. Mo, **B. Tenner**, R. Huganir, J. Zhang. Single-fluorophore Biosensors for Sensitive and Multiplexed Detection of Signaling Activities. **Nature Cell Biology** (2018) 20(10): 1215-1225.

Abstract

Dissecting the dynamic interplay within biochemical networks requires the simultaneous monitoring of many signaling activities. Although optically-based, genetically-encoded biosensors have proven indispensable for uncovering spatiotemporal regulation within specific signaling pathways, combining multiple sensors in a single experiment has been difficult due to limited spectral space. To help bridge this gap, we developed two new classes of biosensors suitable for multiplexed imaging. The modular architecture and single-color properties of these new sensors expands the toolset for interrogation of several signaling pathways in a single cell. In order to further broaden the utility of these sensors, we designed additional kinase sensors and color variants. We also constructed and applied higher-throughput screening platforms for optimizing these sensors and improve their sensitivity. The multiplexed biosensors and screening methodologies presented here will help researchers unravel the complex regulation within signaling networks and advance the engineering of specialized sensors.

Introduction

Cells utilize a multitude of signaling pathways in order to encode, transduce, and process information. These pathways are marked by complex interactions between specialized enzymes, such as kinases and phosphatases, in order to enable specialized functions. Genetically-encoded biosensors, such as the ones mentioned in previous chapters, have proven instrumental in dissecting the spatiotemporal organization of certain signaling cascades by transforming specific biochemical activities into changes in fluorescence, at a single-cell resolution. However, these interactions rarely operate independently from one other and it is the crosstalk between different pathways that create essential emergent phenomenon and complex behavior. In order to probe these intricate signaling networks, multiplexed biosensor measurements in which multiple signaling activities are monitored in parallel and in an individual cell become necessary.

The primary challenges for multiplexing FP-based, genetically-encoded biosensors include the limited spectral space available for imaging multiple sensors and dampened signals in multiplexing experiments, which could be overcome by the design and optimization of novel sensors (Mehta et al. 2011). To this end, much work has focused on development and optimization of single-color and single-FP sensors in order to minimize each sensor's spectral footprint (Mehta et al. 2018, Ross et al. 2018, Piatkevich et al. 2018). Here we highlight our recent contributions, which consist of two new classes of biosensors for multiplexed imaging and the development of a few screening techniques. This chapter is divided into two parts: Part 1 will introduce FLAREs (FLuorescence Anisotropy REporters) for ratiometric, single-color biosensing, and Part 2 will focus on screening efforts directed towards optimizing single-FP-based ExRais (Excitation Ratiometric sensors).

Part 1 – FLAREs: Single-color, ratiometric biosensors for detecting signaling activities in live cells

Introduction

Most FP-based, genetically-encoded biosensors fall into two categories: single-color or ratiometric. Single-color probes, such as the widely-used Ca^{2+}-sensitive CaMP reporters utilize a single FP with a single pair of excitation and emission wavelengths, and thus leave more spectral space available for additional sensors (Akerboom et al. 2013). However, this single emission-based readout can introduce unwanted measurement variation due to probe expression levels or imaging conditions. Ratiometric sensors, such as the FRET-based reporters mentioned earlier, can cancel these variations out at the expense of a larger spectral footprint (FRET channel divided by donor channel). Ideally, a class of sensors that could combine the robustness of ratiometric reporters with the smaller spectral occupancy of single-color probes could prove invaluable for multiplexed biosensing.

In order to design a requisite sensor, we turned to the under-utilized phenomenon of homoFRET, where the polarization of emitted fluorescence depends on FRET between two identical fluorophores (Lakowicz et al. 2006). To prototype a homoFRET-based sensor, we took our optimized heteroFRET-based PKA activity sensor, AKAR4 (Depry et al. 2011), and replaced the donor and acceptor FPs with FPs of a single color (Figure 4.1a). We tested the different color variants in HEK293T cells, under fsk/IBMX stimulation conditions, by exciting with polarized light and measuring the loss of anisotropy of the emitted fluorescence. We found that several FP combinations reported a PKA-dependent, robust decrease in anisotropy (Figure 4.1a-c). The use of a single excitation/emission wavelength validates the homoFRET-based sensor as single-color while the anisotropy parameter is inherently ratiometric, and thus we termed this type of sensor a FLARE (FLuorescence Anisotropy REporter). In this section, we describe extensions of the FLARE toolset to include reporters of other kinase activities and second messengers, and demonstrate the usefulness in multiplexed detection of several signals at single-cell resolution.

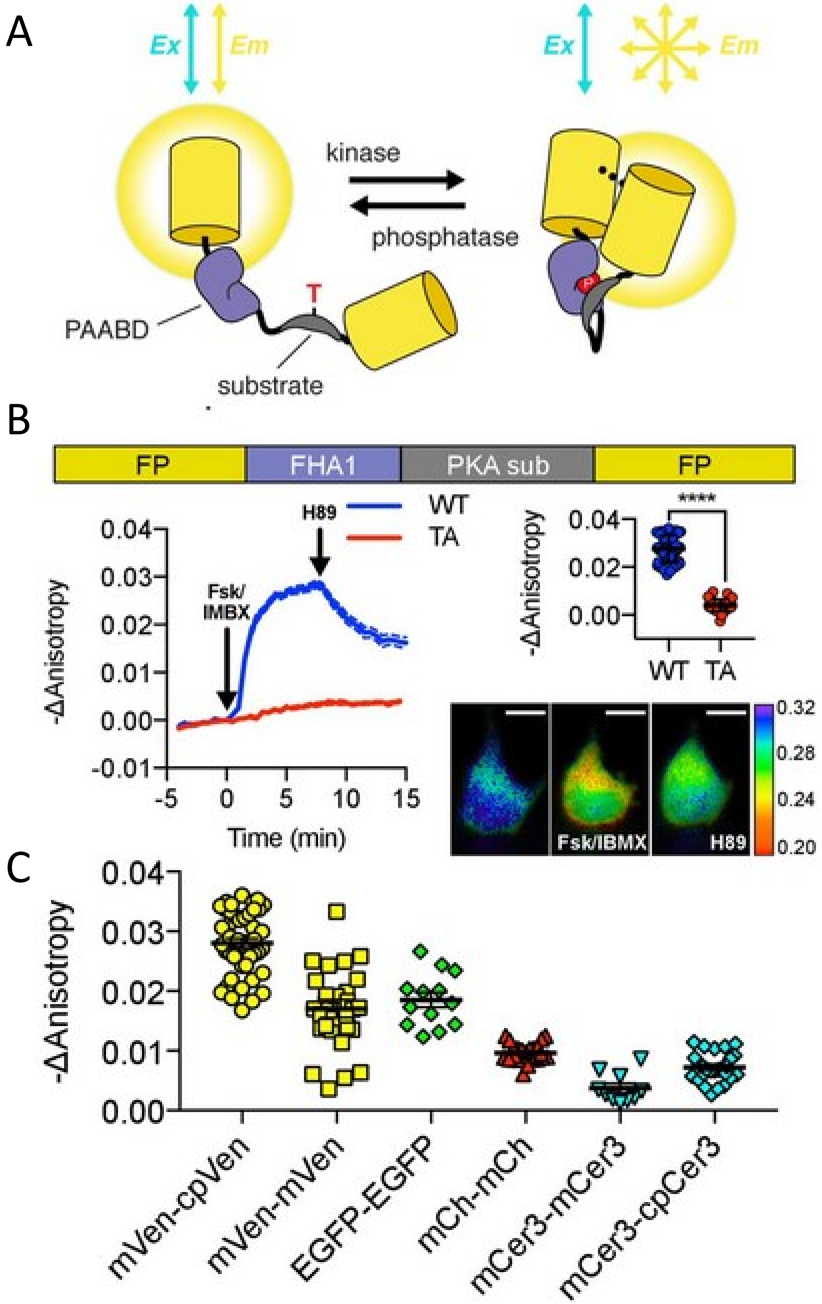

Figure 4.1 Design and characterization of FLARE AKAR. (A) Schematic of a kinase activity FLARE (B) Diagram illustrating domain structure of FLARE-AKAR (top). Time-course of mean fluorescence anisotropy of Venus-cp172Venus FLARE-AKAR wild type (blue, N = 44) and kinase insensitive T-to-A mutant (red, N = 38) expressed in HEK293T cell, stimulated with 50 µM forskolin and 100 µM IBMX at t = 0 min, and 20 µM H-89 at t = 24 min (left). Dashed lines above and below represent standard error of the mean. Changes in anisotropy upon Fsk/IBMX stimulation for both FLARE-AKAR WT and T-to-A mutant (upper right, two-tailed t-test, p<0.0001), calculated as the difference between the mean anisotropy from t = 5 min to t = 7.5 min and the mean anisotropy of the baseline before drug addition. The mean for each is shown, with the error reflecting the standard error of the mean. Representative anisotropy pseudocolor image before Fsk/IBMX stimulation (t = 0 min), after Fsk/IBMX stimulation (t = 7.5 min), and after inhibition of PKA with H-89 (t = 24 min) (lower right) (C) Comparison of the

magnitude of the anisotropy change for different color variants of FLARE-AKAR upon stimulation with Fsk/IBMX including Venus-cp172Venus AKAR (N = 44), Venus-Venus FLARE AKAR (N = 32), EGFP-EGFP FLARE AKAR (N = 13), mCh-mCh FLARE AKAR (N = 22), mCerulean3 FLARE-AKAR (N = 10), and mCerulean3-cp173Cerulean FLARE-AKAR (N = 26). The mean for each is shown, with the error reflecting the standard error of the mean.

Results and Discussion

A FLARE panel for kinases and second messengers

The molecular architecture of the FLARE AKAR prototype differs minimally from other heteroFRET-based reporters, some of which were covered earlier. To expand the toolset to include sensors for other important kinases, we took the top-performing FP pair from the FLARE AKAR prototypes, mVenus–cpVenus (circularly permuted at position 172), and swapped out the PKA conformational switch for switches used in other kinase sensors. First, we sought to design a FLARE for PKC activity, so we replaced the PKA substrate domain in FLARE AKAR with the PKC-specific substrate domain from CKAR (C Kinase Activity Reporter) (Figure 4.2) (Violin et al. 2003). We transfected HEK293T cells and upon stimulation with phorbol 12-myristate 13-acetate (PMA, 100ng/mL) to stimulate PKC activity, we observed a robust anisotropy decrease (-0.02 ± 0.001, n=26) (Figure 4.2a). Next, we wished to create a FLARE version of EKAR-EV, the genetically-encoded biosensor for Erk activity. We exchanged the conformational switch for the Erk substrate peptide, a flexible EV linker, and a WW domain (PAABD), and tested the sensor in HEK293T. Treatment with EGF (100ng/mL) triggered an anisotropy decrease (-0.02 ± 0.001) which could be reversed with the Erk inhibitor U0126 (20uM) (n=13) (Figure 4.2b). As negative controls, the phosphorylation mutants were also checked and failed to elicit stimulated responses. To further expand the toolset for multiplexed imaging, we also wanted to make different color variants of these kinase sensors, and so we swapped out the mVenus-cpVenus pair for other pairs of same-color FPs, including mCherry-mCherry for red sensors and mCerulean3-mCerulean3 for cyan sensors. Testing these sensors with appropriate stimulation conditions yielded many successful color variants with signal-to-noise ratios summarized in Table 4.1.

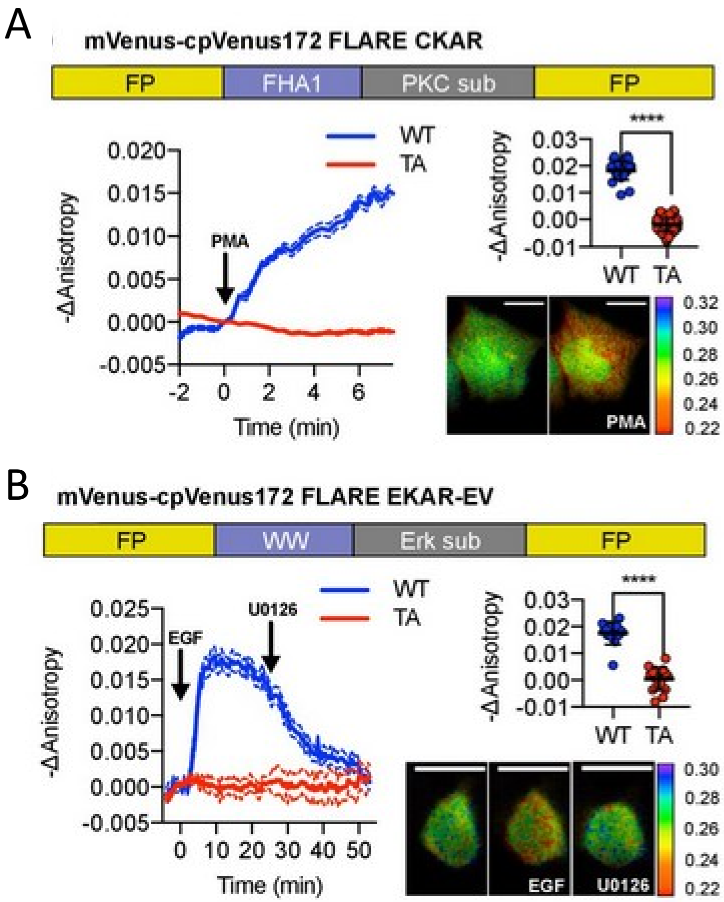

Figure 4.2 A panel of kinase activity biosensors (A) Domain structure of FLARE-CKAR (above). Time-course of fluorescence anisotropy of Venus-cp172Venus FLARE-CKAR WT (blue, N = 26) and kinase-insensitive mutant (red, N = 119) with addition of 100 ng/mL phorbol 12-myristate 13-acetate (PMA) at t = 0 min. Summary of response magnitudes (upper right, two-tailed t-test, $p<0.0001$), calculated as the difference between the mean anisotropy from t = 10 to t = 11.33 min and the mean anisotropy of the baseline before drug addition. The mean is shown, with the error reflecting the standard error of the mean. Representative anisotropy pseudocolor image before PMA addition (t = 0 min) and after PMA addition (t = 15 min). (B) Domain structure of FLARE-EKAR-EV (above). Time-course of mean fluorescence anisotropy of Venus-cp172Venus FLARE-EKAR-EV WT (blue, N = 13) and kinase-insensitive mutant (red, N = 16) expressed in HEK293T cell, with addition of 100 ng/mL EGF at t = 0 min and 20 µM U0126 at t = 25 min (left). Summary of anisotropy changes (upper right, two-tailed t-test, $p<0.0001$), calculated as the difference between the mean anisotropy from t = 10 min to t = 15 min and the mean anisotropy of the baseline before drug addition. The mean is shown, with the error reflecting the standard error of the mean. Representative anisotropy pseudocolor image before EGF stimulation (t = 0 min), after EGF stimulation (t = 25 min), and after inhibition of MEK with U0126 (t = 47.5 min) (lower right).

Table 4.1 SNRs of several color variants of FLARE AKAR, FLARE CKAR, and FLARE EKAR-EV sensors

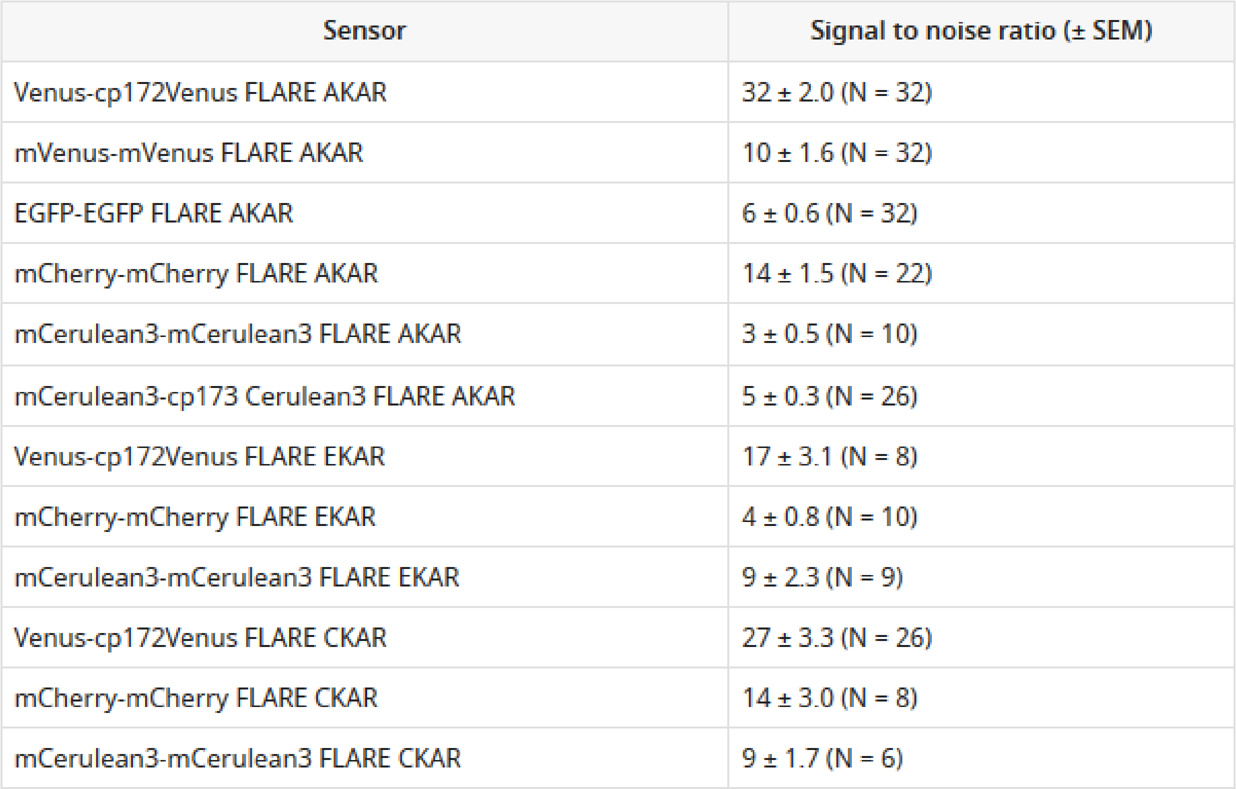

Sensor	Signal to noise ratio (± SEM)
Venus-cp172Venus FLARE AKAR	32 ± 2.0 (N = 32)
mVenus-mVenus FLARE AKAR	10 ± 1.6 (N = 32)
EGFP-EGFP FLARE AKAR	6 ± 0.6 (N = 32)
mCherry-mCherry FLARE AKAR	14 ± 1.5 (N = 22)
mCerulean3-mCerulean3 FLARE AKAR	3 ± 0.5 (N = 10)
mCerulean3-cp173 Cerulean3 FLARE AKAR	5 ± 0.3 (N = 26)
Venus-cp172Venus FLARE EKAR	17 ± 3.1 (N = 8)
mCherry-mCherry FLARE EKAR	4 ± 0.8 (N = 10)
mCerulean3-mCerulean3 FLARE EKAR	9 ± 2.3 (N = 9)
Venus-cp172Venus FLARE CKAR	27 ± 3.3 (N = 26)
mCherry-mCherry FLARE CKAR	14 ± 3.0 (N = 8)
mCerulean3-mCerulean3 FLARE CKAR	9 ± 1.7 (N = 6)

Similarly to the FluoSTEPS, we wished to grow the FLARE panel to include sensors for second messengers. In order to make a Ca^{2+} version, we sandwiched the conformational switch from the Cameleon family of probes (Nagai et al. 2004), composed of calmodulin (CaM) and the Ca^{2+}/CaM-binding peptide M13, between mVenus and cpVenus (Figure 4.3a). Transfecting the FLARE Cameleon into HEK293T and stimulating with ionomycin (1uM) and Ca^{2+} (5mM) elicited a robust change in anisotropy (-0.03 ± 0.002, n=10) (Figure 4.3b). For a cAMP sensor, we took the same cAMP binding domain/switch derived from Epac and from our ICUE probe (Violin et al. 2007) and inserted it between mVenus and cpVenus. Stimulating the sensor with fsk/IBMX produced a positive change in anisotropy, consistent with cAMP-induced FRET decreases in the original ICUE (+0.02 ± 0.001, n=40) (Figure 4.3c). The modular design of FLAREs establishes an easily-implementable strategy for generalizing the toolset to make additional sensors for other biochemical signals, and in a variety of different colors.

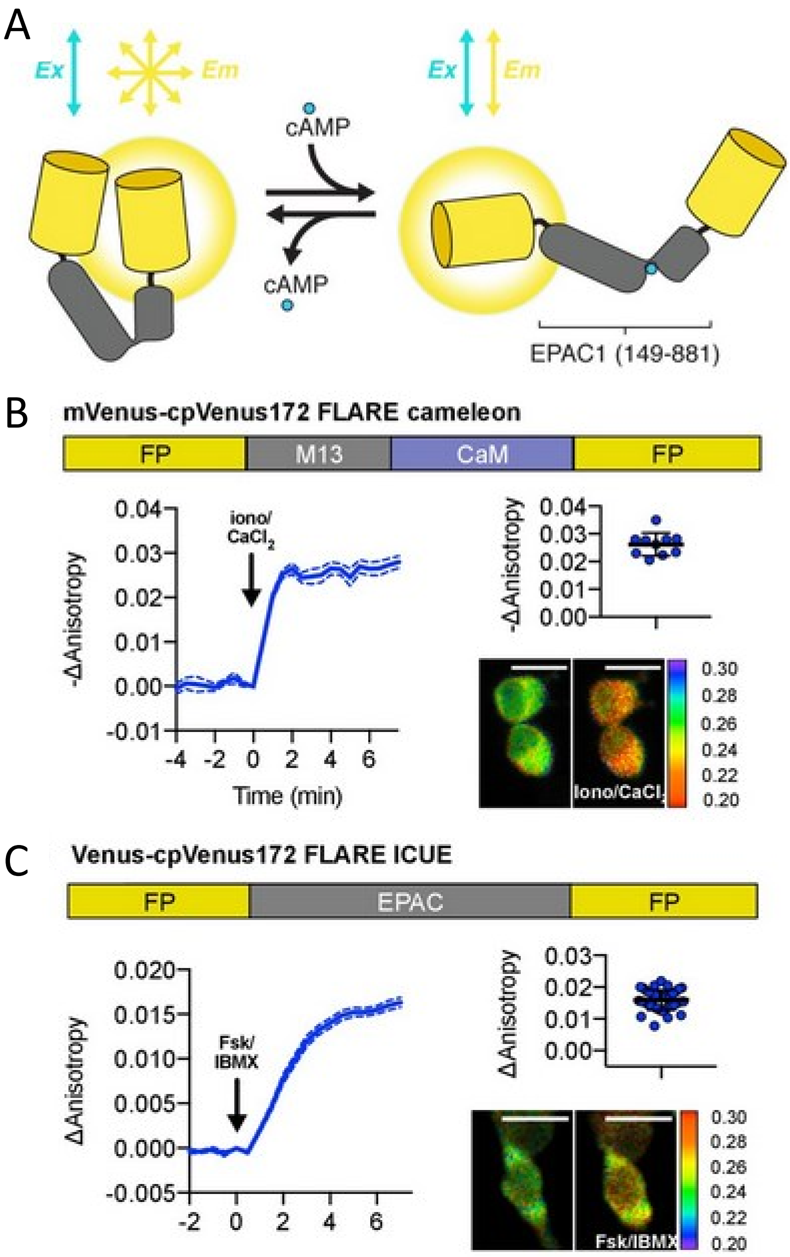

Figure 4.3 Design and characterization of FLARE second messenger sensors (A) Schematic of FLARE ICUE cAMP biosensor. (B) Domain structure of FLARE-Cameleon (top). Time-course of mean fluorescence anisotropy of Venus-cp172Venus FLARE-Cameleon (N = 10) with addition of 1 μM ionomycin and 5 mM $CaCl_2$. Summary of anisotropy changes after 1 μM ionomycin and 5 mM $CaCl_2$ (upper right) calculated as the difference between the mean anisotropy from t = 5 min to t = 7.5 min and the anisotropy of the baseline before drug addition Representative anisotropy pseudocolor image before and after 1 μM ionomycin and 5 mM $CaCl_2$ addition. (C) Domain structure of the cAMP biosensor FLARE-ICUE (top). Time-course of mean fluorescence anisotropy of Venus-cp172Venus FLARE-ICUE (N = 40) with addition of 50 μM forskolin and 100 μM IBMX at t = 0 (left). Summary of anisotropy changes after 50 μM forskolin and 100 μM IBMX with respect to baseline (upper right), calculated as the difference between the mean anisotropy from t = 5 min to t = 7.5 min and the anisotropy of the baseline before drug addition. Representative anisotropy pseudocolor image before (t = 0 min) and after (t = 7.5) stimulation with Fsk/IBMX (lower right). Dashed lines above and below time course reflect standard error of the mean.

Multiplexed imaging of FLAREs in single cells

In order to demonstrate the utility of FLAREs, we chose to deploy multiple sensors at once for parallel monitoring of signaling pathways. Two-channel imaging is routinely done, but simultaneous imaging of three signaling events is much less common due to sensor limitations. First, we expressed red FLARE AKAR, yellow FLARE EKAR, and cyan FLARE Cameleon into HEK293T cells. Sequential addition of fsk/IBMX, EGF, and thapsigargin (1uM) at three different times within a time course to stimulate PKA, Erk, and Ca^{2+}, respectively, elicited appropriate responses in the FLAREs (n=17) (Figure 4.4a). Minimum crosstalk was observed between the three signals, highlighting the specificity and power of FLAREs for multiplexed interrogation.

To test the sensors under more physiological, submaximal stimulation conditions, we turned to signaling within the pancreatic beta cell. As previously mentioned, the complex interplay of Ca^{2+} and cAMP characterize an oscillatory circuit responsible for regulation of normal beta cell function (Ni et al. 2011). We wished to monitor these two signals in parallel, and so we transfected MIN6 beta cells with untargeted yellow FLARE ICUE and cyan FLARE Cameleon and stimulated with TEA. As expected, we observed Ca^{2+} and cAMP oscillating out-of-phase from one another (Figure 4.4b). Taken together, we envision the FLARE platform to serve as a powerful toolset for probing multiple signaling pathways through multiplexed imaging. Further development will include designing new FLAREs for other enzymes and second messengers, as well as sensor optimization to increase the SNR and dynamic range.

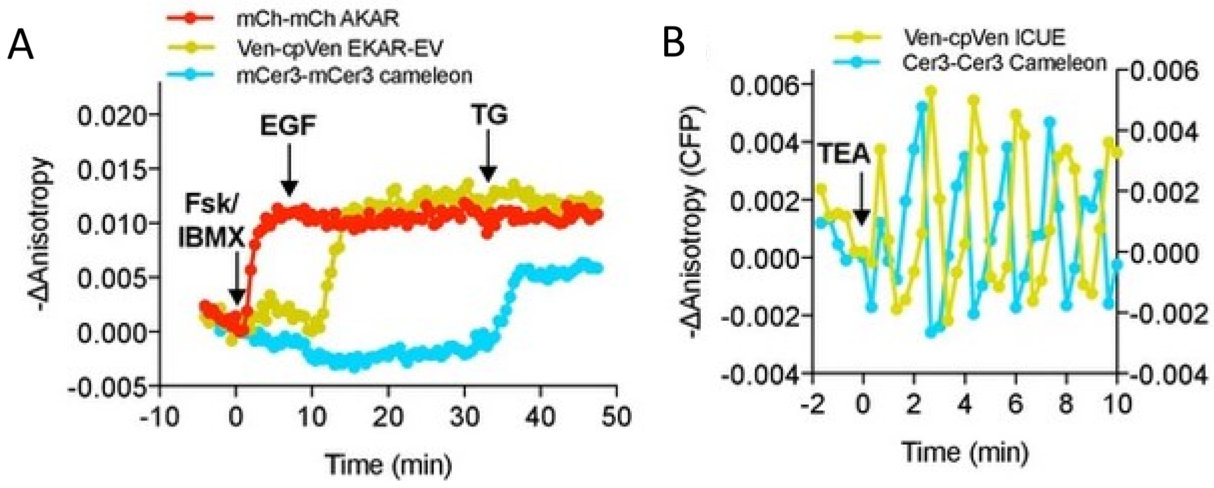

Figure 4.4 Multiparameter imaging with FLAREs (A) Time-course of a representative HEK293T cell co-expressing mCherry-mCherry FLARE-AKAR, mVenus-cp172Venus FLARE-EKAR-EV, and mCerulean3-mCerulean3 FLARE-Cameleon, with 50 µM forskolin and 100 µM IBMX added at t = 0 min, 100 ng/mL EGF at t = 7.5 min, and 1 µM thapsigargin added at t = 32.5 min (N = 17). (B) Anisotropy response of a representative MIN6 cell co-expressing Cerulean3-Cerulean3 FLARE-Cameleon and Venus-cp172Venus FLARE-ICUE, showing robust oscillations after stimulation with TEA at t = 0 min (N = 19).

Part 2 – Screening methodologies for developing and optimizing single-FP biosensors

Introduction

Single-FP biosensors, based on a single circularly-permuted fluorescent protein (cpFP), provide an alternative strategy for achieving multiplexed signaling interrogation. Recently, we designed and characterized a suite of single-FP sensors for monitoring PKA activity (Mehta et al. 2018) by sandwiching cpFP color variants (eg. cpGFP and cpBFP) between the PKA-specific substrate domain and the phosphoamino acid binding domain (PAABD) from the FRET-based PKA reporter AKAR4 (Depry et al. 2011). PKA-dependent phosphorylation of the substrate domain triggers a binding event with the PAABD, FHA1, which in turn modulates the protonation state of the cpFP's chromophore and thus the photophysical properties. This modular design allowed us to successfully generalize this color suite to include sensors for other important kinases (eg. PKC and Akt) by swapping out the substrate domain and the PAABD. By utilizing these reporters, including organelle-targeted versions, we successfully demonstrated simultaneous multiplexing of six sensors in single cells.

Despite the proven application of these first generation sensors, limitations include a relatively low signal-to-noise ratio compared to the Ca^{2+} biosensors and a color palette that can be further expanded. Here we introduce three single-FP biosensor screening methodologies and work to apply them for optimizing our first-generation of sensors. Although we demonstrate the screening function for PKA activity sensors in particular, similar approaches could be used for the design and optimization of sensors for other enzymes and second messengers.

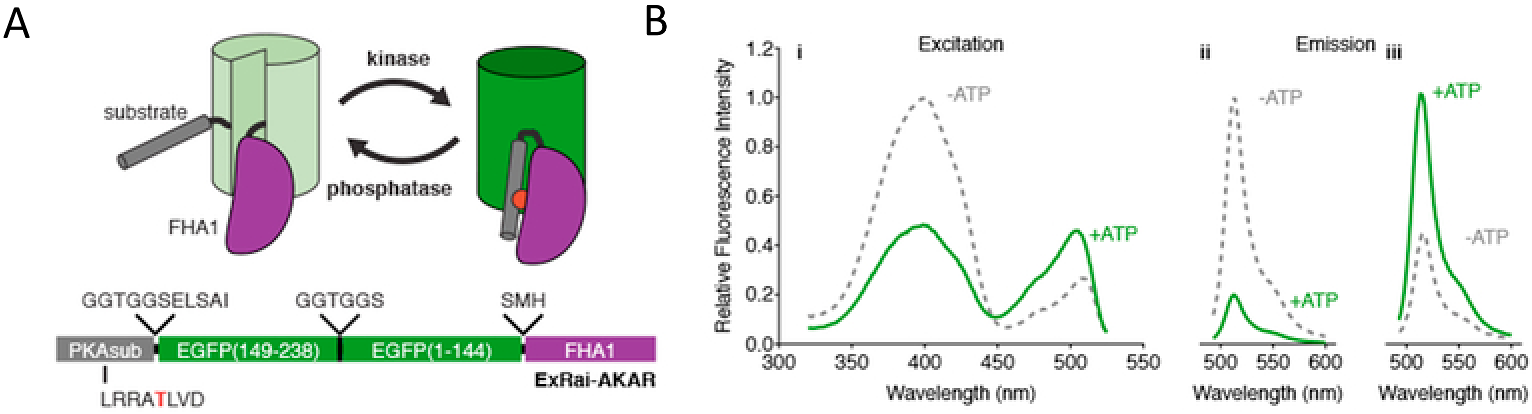

Figure 4.5 Design of ExRai-AKAR (A) Modulation of cpFP fluorescence by a phosphorylation-dependent molecular switch. ExRai-AKAR domain structure. (B) Representative ExRai-AKAR fluorescence spectra collected at (i) 530 nm emission and (ii) 380 nm or (iii) 488 nm excitation without (gray) or with (green) ATP in the presence of PKA catalytic subunit. *n*=3 independent experiments.

Results and Discussion

Improving the dynamic range for ExRai-AKAR and blueAKAR probes using a lysate screening approach

In one of the first generation single-FP sensors for PKA, ExRai-AKAR (Excitation Ratiometric Activity Reporter – A Kinase Activity Reporter), cpGFP was used as the reporting unit. The design for ExRai-AKAR closely resembles the popular calcium reporter GCaMP where a Ca^{2+}-induced conformational change modulates the emission intensity of the cpGFP from a single-peak excitation by altering the immediate electronic environment at the circularly-permuted site and chromophore (Chen et al. 2013). Interestingly, ExRai-AKAR displays two excitation peaks (ex: ~400nm and 509nm, em: 515nm) instead of the single excitation peak in GCaMP (509nm) and is reminiscent of the double-peaked wild-type GFP from A. victoria, despite having the mutations designed to simplify the excitation spectrum (Figure 4.5) (Tsien 1998; Cormack et al. 1996). Furthermore, phosphorylation by addition of purified catalytic subunit of PKA to purified sensor in the presence of ATP leads to a decrease in the 400nm excitation peak (approx. -50%) but an increase in the 509nm peak (approx. +100%). This unique behavior allows the ExRai-AKAR probe to function as a ratiometric sensor where the ratio between the emitted 515nm fluorescence intensity excited at 509nm and 400nm cancels out the probe's concentration-dependence and imaging condition variations. Despite the large dynamic range (DR) of ExRai-AKAR post fsk/IBMX stimulation (approx. 2-fold increase in excitation ratio), especially compared to the DR of previous FRET-based PKA reporters (Depry et al. 2011), some low-amplitude PKA signaling events, such as compartmentalized signals, might still evade detection. Thus, we sought to further improve the DR of the ExRai-AKAR sensor.

Crystal structures and previous work on the optimization of GCaMP and other cpGFP-based sensors suggested that the residues in the vicinity of the phenolate in the fluorophore were critical for the sensor properties (Tian et al. 2010). This included parts of the seventh beta strand in the FP, the site of circular permutation, and the linkers between the cpFP and the sensor-specific domains. For ExRai-AKAR, we decided to focus on optimizing the sensor by modifying the linkers between the PKA substrate domain and the cpGFP, and the cpGFP and FHA1. Unfortunately, lack of crystal structures of the sensor in the high- and low-PKA activity states precluded using a semi-rational design approach where replacing specific amino acids with specific residues within the linkers is followed by a small-scale screen. Instead, we designed an ExRai-AKAR sensor library where two randomized amino acids were inserted into each of the two linkers (originally SM/AI, now XX/XX) (Figure 4.6). However, the theoretical size of the library (20^4 = 160,000 variants) required a larger-scale/higher-throughput screening method for identifying sensor variants with an improved DR.

The screen we adopted consisted of three parts: 1) identification of promising sensor variants from E.coli colonies expressing the sensor on agar plates, 2) testing of selected variants using crude lysates and purified PKA catalytic subunit (PKA_{cat}), and 3) a follow-up validation in mammalian HEK293T cells (Figure 4.6). In the first part, we transformed and expressed the ExRai-AKAR linker library in BL-21 E.coli and measured the emitted green fluorescence from each bacterial colony during excitation at 390nm and 488nm using a home-built setup. The colonies displayed a wide variation in fluorescence under both excitation wavelengths. In order to maximize the change in the excitation ratio, we reasoned that colonies that displayed high intensity fluorescence under 380nm excitation but low intensity under 488nm could yield optimized ExRai probes due to the presence of the sensors in a low-PKA state in the bacteria. To test, we selected 480 such colonies and inoculated them in several 96-well plates for growth, induction, and finally lysis. For assessing the PKA sensitivity of the selected library variants, we measured the excitation ratio of the crude, clarified lysates containing in the presence and absence of purified PKA_{cat}. We identified 20 potentially improved sensors (>4-fold increase in the emission ratio $\Delta R/R$ upon PKA_{cat} addition) and subcloned them into mammalian expression vectors for follow-up testing in HeLa cells. From this work, we identified a second-generation ExRai-AKAR (ExRai-AKAR2) sensor with phenylalanine-cysteine (FC) in the first linker position and leucine-leucine (LL) in the second linker position. Upon fsk/IBMX stimulation, this optimized sensor displayed almost an approx. 9.5-fold increase in the excitation ratio (-80% decrease under 380nm excitation, 2-fold increase under 488nm excitation), improving the DR from the first-generation sensor by approx. 4-fold (Figure 4.7a). Further characterization of this sensor, for example its pH sensitivity and subcellular targeting effects, should be performed for validation. Additional optimization focusing on the phosphorylated substrate’s interaction with FHA1 might additionally improve properties of ExRai-AKAR.

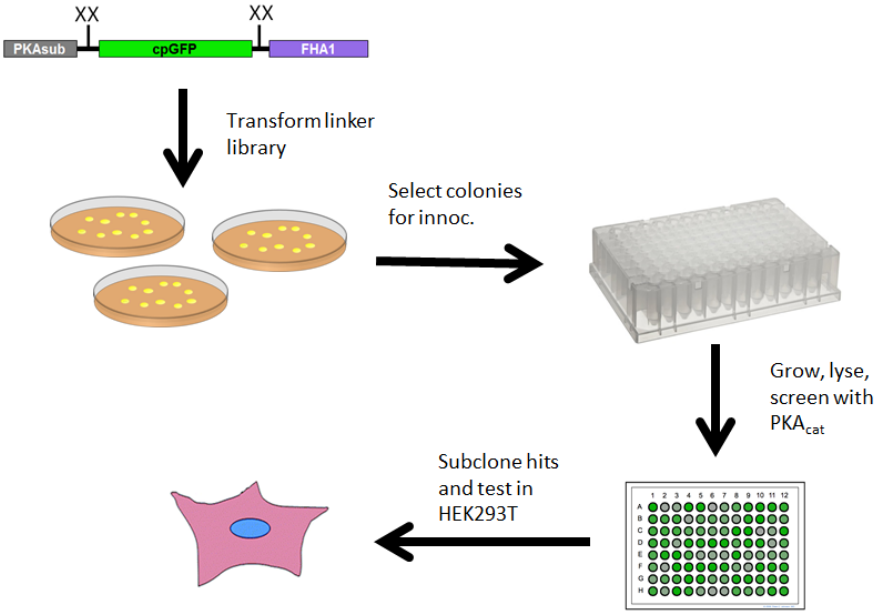

Figure 4.6 Schematic of the lysate screening setup.

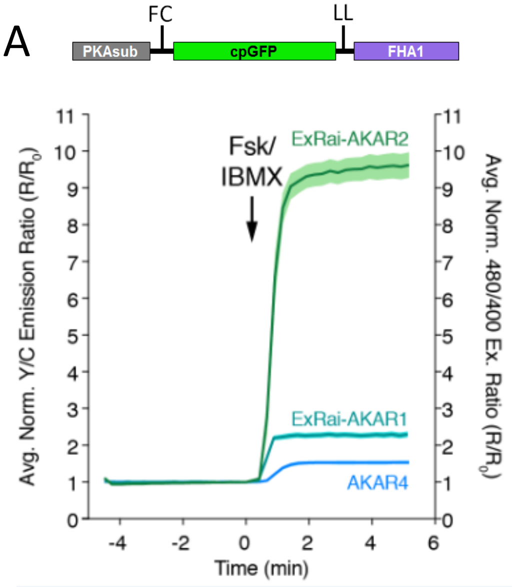

Figure 4.7 ExRai-AKAR2 optimized sensor (A) Schematic showing the ExRAI-AKAR2 sensor with the optimized FC/LL linkers. Fsk/IBMX treatment in HeLa cells elicit an approx. 9.5-fold change in the excitation ratio (green trace). ExRai-AKAR1 (teal) and AKAR4 (blue) are shown for comparison.

In parallel with ExRai-AKAR, we wished to improve the DR of the previously published blueAKAR probe (Mehta et al. 2018) for use in multiplexed imaging. Unlike the ExRai-AKAR sensor, blueAKAR is a negative probe and has only a single excitation peak; however, the cpBFP reporting moiety from blueAKAR shares sequence similarity with cpGFP, and so we hypothesized that a similar linker library design and screen could work here. Once again, we replaced amino acids in the two linker regions of blueAKAR with randomized amino acids ($Linker_1/Linker_2$: AI/SM → XX/XX) and expressed the library variants in E.coli colonies. Fluorescence overall from the colonies was weak (ex: 390nm, em: 440nm), but we still selected 96 of the brightest colonies, reasoning that these variants represented the low PKA state and might yield a larger decrease upon PKA phosphorylation. By screening the crude lysates, followed by testing potential hits in HEK293T, we identified a two linker variants (AI/HM, AI/HL) with a decrease -17.8% ± 0.4% and -19% ± 2.5% (n=5, 3) upon fsk/IBMX, representing an improvement of approx. 2-fold over the first-generation blueAKAR (Figure 4.8a). In parallel, we also decided to substitute blueAKAR's linkers with other winning linker variants from the screen for an improved ExRai-AKAR with the idea that the large PKA-dependent decrease in the 400nm excitation peak of ExRai-AKAR might function similarly to the decrease of the single excitation peak in blueAKAR. Surprisingly, we found a blueAKAR variant with LQ/LL for linkers displayed comparable fluorescence intensity and a -49.3% ± 2.9% response to fsk/IBMX, an approx. 5-fold improvement over the first-generation blueAKAR. This hints at not only a possible common mechanism for these single-FP sensors, but also potential drawbacks to our screening methodology. We might have missed the LQ/LL linker variant in our initial lysate screen for a few possible reasons, including a low-complexity library prep (inadequate coverage of all possible linker variants initially synthesized) or an inadequate sampling of linker variants at any screening/selection stage. For example, our selection criteria for sensors from the bacterial colonies might have been ill-guided, or our limited number of colonies for lysate screening prevented us from sampling a representative collection of linker variants. In any case, a platform that could improve the throughput of testing sensor variants would be valuable in combating this potential lysate screening "bottleneck" and provide a faster path with higher capacity for optimizing these biosensors.

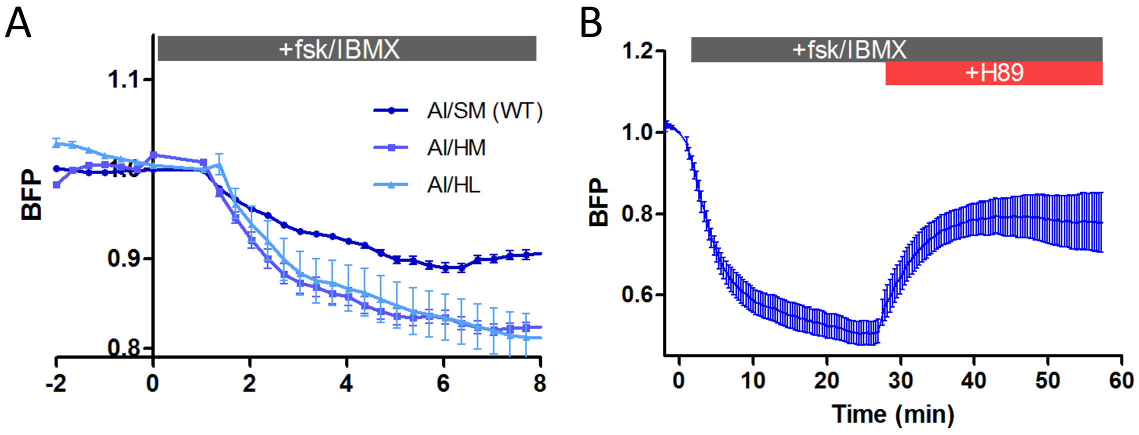

Figure 4.8 Optimized blueAKARs (A) Linker variants identified from the lysate & mammalian cell screen. Dark blue is the AI/SM original published linker for comparison. Medium blue is AI/HM linker variant. Light blue is AI/HL linker variant. Normalized blue fluorescence intensity was measured. Fsk/IBMX triggered decreasing responses (-9.6% ± 0.6%, -17.8% ± 0.4%, -19% ± 2.5%; n=5, 3, 6). (B) blueAKAR(LQ/LL) linker variant demonstrated a superior response to fsk/IBMX (-49.3% ± 2.9%, n=5) and was reversed with H89.

Optimizing a greenAKAR probe for single-color applications with a bacterial colony-based screen

Although the ratiometric readout is adventitious for quantification and canceling out probe-dependent effects, the ExRai sensors still suffer from limitations in multiplexing due to the need to excite at two wavelengths. Therefore, we next sought to design a "true" greenAKAR, a PKA sensor that still responded to PKA activity under 488nm excitation, but had minimum fluorescence under 380nm excitation. Initially, we utilized the same linker library from the previous ExRai-AKAR screen because of the observed variation in green fluorescence under both excitations. We hypothesized bacterial colonies expressing successful greenAKAR sensors would either be dim in both channels, or dim under 380nm excitation and bright under 488nm excitation, representative of the low-PKA state. However, subsequent lysate screening of selected colonies under both criteria failed to produce a greenAKAR sensor (data not shown). This can most likely be explained by the absence or low expression of fluorescent sensors in the dim/dim case, something the previous ExRai-AKAR screen didn't suffer from due to "self-normalization" from the bright 380nm excitation signal. The second selection criterion (dim/bright) was most likely inappropriate for finding a greenAKAR and also suffered from a lack of a good benchmark for the bright 488nm state.

In order to continue working with the ExRai-AKAR linker library for designing a greenAKAR, we decided to abandon the colony selection step for lysate screening and instead develop an alternative screening platform that tested PKA responsiveness of library variants *in situ*, within the bacterial colony on the agar plate. We figured that this strategy could eliminate the lysate screening "bottleneck," reduce the involved labor, and increase the overall throughput of a library screen. Our approach, inspired by a similar approach (Ibraheem et al. 2011), consisted of the design of a bacterial dual expression vector where one constitutive promoter drives expression of the biosensor library and an inducible promoter controls expression of a signaling enzyme. Imaging of the sensor library in colonies, first in the absence and then in the presence of the inducer, could theoretically allow researchers to capture the fluorescence of each variant's low and high signaling states while still on agar plates. To first test this strategy, we created a dual expression vector comprised of ExRai-AKAR2 under the control of a constitutively active T7 promoter. The gene for PKA_{cat}, tagged with an mScarlet RFP, was inserted after an arabinose-inducible promoter and determined not to need additional factors due to the abundance of ATP present in E.coli (data not shown). Spraying transformed E.coli colonies with arabinose induced robust expression of PKA_{cat} (approx. 6-fold change, from observed RFP intensity) over the span of several hours, which subsequently induced an excitation ratio change (approx. +60% fold, 488nm/390nm) in the colonies (Figure 4.9a,b). Aside from slight optimization of the agar plates (addition of glucose to inhibit leaky expression from the arabinose-inducible promoter), development and implementation of this strategy was straightforward.

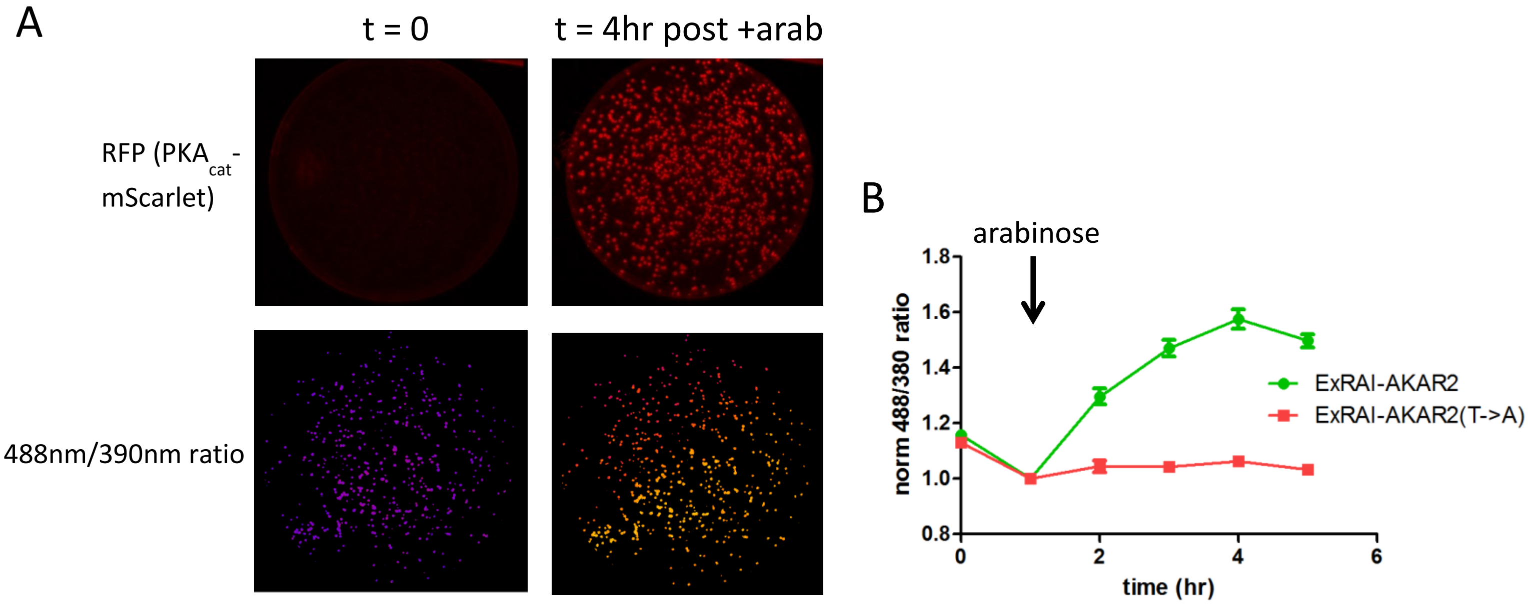

Figure 4.9 ExRai-AKAR2 in situ colony response to induced PKA$_{cat}$ expression. (A) Fluorescence images of bacterial colonies on petri plate with LB-agar. Spraying arabinose induces strong expression of mScarlet-tagged PKA$_{cat}$ after 4 hours, shown above. In a separate experiment/dish, we sprayed the bottom right half the plate and created a spatial gradient of arabinose. Constitutively-expressed ExRai-AKAR2 responds in the 488nm/380nm ex ratio shown below according to the spatial gradient. (B) The response of the ExRai-AKAR2 is approx. +60% in colonies. As a negative control, the phosphorylation mutant does not respond.

We then decided to apply this platform to screen for greenAKAR. We used the same linker library (XX/XX) from the previous ExRai-AKAR screen, but tagged the C-terminus of the sensor with a long, rigid linker ([EAAAK]$_5$ to prevent FRET) followed by mScarlet for normalization of sensor concentration (Figure 4.10a) (Chen et al. 2014). Once again, untagged PKA$_{cat}$ was placed under control of the arabinose-inducible promoter. For a small-scale demonstration of the technique, a total of 25 agar plates were screened and the three relevant fluorescence channels were monitored over the course of about six hours post arabinose induction. After applying analysis filters for the colonies, such as PKA-induced response in the

488nm excitation channel, normalized brightness in the 488nm excitation channel, and normalized brightness in the 390nm excitation channel, a select few linker variants were chosen for subcloning and testing in HEK293T cells. From these hits, one linker variant (FK/LS) was identified and briefly characterized (Figure 4.10b). In HEK293T cells, this variant showed a dim 400nm excitation fluorescence but still maintained a robust PKA-induced response under 488nm excitation (excitation increased approx.. 2-fold increase; GFP intensity increased +70.3% ± 4.4% in HEK293T, n=17) (Figure 4.10c). This greenAKAR candidate provides an excellent starting point for subsequent screens in order to increase the DR and further reduce the brightness of the 390nm state. Crystal structures could help guide a successful mutagenesis strategy, possibly by identifying the distributed UV-triggered excited state proton transfer (ESPT) network, the likely mechanism behind the 390nm excitation (Jung et al. 2005). However, some involved residues might also function in the maturation of the fluorophore, and so an untargeted mutagenesis approach in parallel might be appropriate. The colony-based screening methodology presented here increased the throughput at which we could functionally test sensor libraries and represents a generalizable strategy for optimizing other kinase sensors.

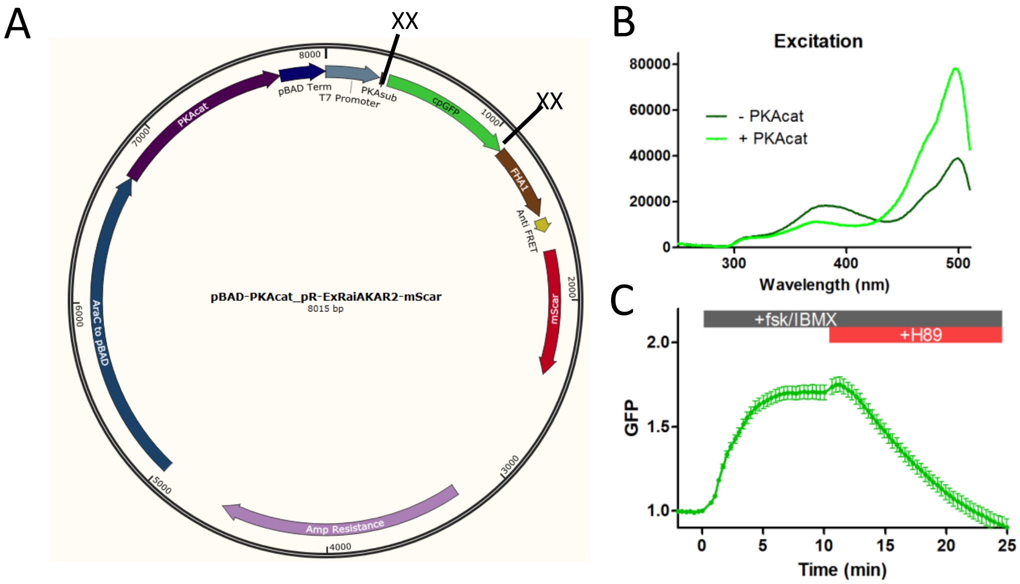

Figure 4.10 Screen for a greenAKAR. (A) Schematic of the dual expression screening vector. Arabinose-inducible promoter (within "AraC to pBAD" insert) drives the expression of PKA_{cat}. T7 promoter drives expression of a sensor library where randomized amino acids (XX/XX) are inserted at the linker sites between PKA_{sub} and cpGFP, and cpGFP and FHA1. The greenAKAR library variants are tagged with mScarlet for normalization. (B) Excitation spectra characterization of a greenAKAR library variant found (linker: FK/LS) with reduced 380nm excitation (compare with ExRai-AKAR in Figure 4.5b). PKA_{cat} addition triggers approx. 2-fold increase in the 488nm excitation peak (with E.coli lysate with expressed greenAKAR). (C) greenAKAR library variant (linker: FK/LS) transfected in HEK293T responds to fsk/IBMX stimulation (+70.3% ± 4.4%, n=17) and reverses upon H89 addition.

Assessing the use of FACS for high-throughput screening of single-color biosensor libraries in mammalian cells

Even with the increased throughput achieved by assessing PKA responsiveness in bacterial colonies, we were still unable to approach complete sampling of the entire ExRai-AKAR linker library. We also noted that many of the top hits from the ExRai-AKAR lysate screen failed to elicit a marked improvement when tested in mammalian HEK293T, possibly highlighting a sensor's dependence on redox environment or the presence/absence of extraneous factors. For these reasons, we sought to raise the throughput of our single-FP sensor screen once again and shift our testing to only mammalian cells.

Fluorescence Activated Cell Sorting (FACS) allows for the rapid, sensitive interrogation and selection of individual cells based on fluorescence intensity. With an assessment rate of thousands of mammalian cells per second, the potential increased throughput inspired us to test the technique’s ability to enrich/select for desired biosensor variants. To begin, we transfected ExRai-AKAR2 into HEK293T and passed the cells through the sorter, measuring green emission (530nm or 520nm) under 488nm and 405nm excitation. The fluorescent cells were highly correlated in both channels because of the ratiometric nature of the ExRai-AKAR2 sensor (Figure 4.11a). Variation along the regression line is primarily attributable to differences in the cell-to-cell expression of the sensor, while orthogonal variation is due in part to differences in the low, basal PKA activity state. Treating the entire population of cells with fsk/IBMX triggered a shift of the correlated population, indicating a sensor response (Figure 4.11b). To order to better evaluate the FACS procedure, we then collected a subsample of cells from within a range in both channels and stimulated PKA activity with fsk/IBMX addition. Re-sorting this subsample produced a large shift in approximately 80% of the population (approx. 2.5-fold in the 405nm ex channel and 5-fold in the 488nm channel), indicating a robust, high-SNR PKA response (Figure 4.11c,d). The other 20% of the re-sorted cells failed to respond to the fsk/IBMX treatment, likely because they died after the first sort. As a “purity” check and a PKA specificity check, we ran re-sorts on an unstimulated subsample and a subsample of ExRai-AKAR2 (T/A) phosphorylation mutant cells (data not shown), respectively, and observed no shift or response (Figure 4.11c). Satisfyingly, the relative spread in the ExRai-AKAR2 shifted population resembled the spread of the unstimulated sample, highlighting low cell-to-cell response variability and low distortion from noise. In order to demonstrate the ability to decouple the brightness in each channel from the sensor expression variability, we inserted mScarlet with a self-cleaving P2A peptide (Liu et al. 2017) behind the ExRai-AKAR2 for normalization and successfully repeated the experiments (data not shown). By collecting cells from a shifted population, the transfected plasmid DNA was recovered and could be used in additional rounds of mutagenesis for a directed evolution screen (Branon et al. 2018).

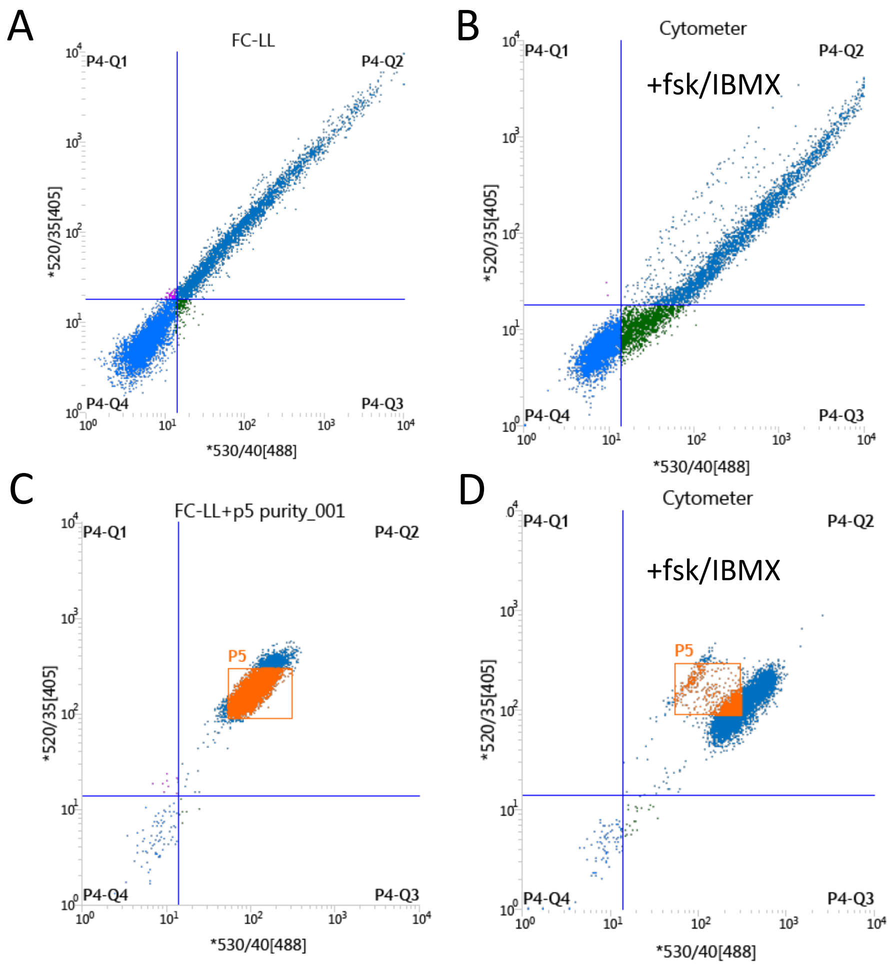

Figure 4.11 FACS on ExRai-AKAR2. (A) FACS profile on HEK293T cells transfected with ExRai-AKAR2. (y-axis: 405nm ex/520nm em; x-axis: 488nm ex/530nm em) (B) FACS profile on cells from A treated with fsk/IBMX. The shift of the entire population indicates a robust response of the ExRai-AKAR2 sensor. (C) Subpopulation of cells taken from A (gated inside orange box) and re-sorted as a "purity check." (D) Subpopulation of cells from C were treated with fsk/IBMX, approx. 80% of the cells responded robustly as seen in the subpopulation shift.

Prominent hurdles with the practical implementation of a FACS-based screening approach include 1) using the sorter to identify a single library variant at a time, and 2) assessing PKA activity responsiveness of the variant relative to other variants. Multiple plasmids can enter and express under transient transfection (sometimes up to 50,000 for current transfection protocols, Cohen et al. 2010); for a sensor library, this means that the response in each cell will be the expression-weighted average of all sensors present. In order to tackle this limitation, we decided to explore the use of a sparse transfection as a low-cost, easily implementable strategy. We reasoned that a mammalian expression plasmid library could be effectively diluted by including a bacterial expression plasmid (Piatkevich et al. 2018). Using cationic lipid-based transfection, this would allow delivery and expression of a small number of library variants per cell. To test this, we constructed a mock library with nuclear-targeted mCherry RFP and nuclear-targeted Venus YFP (1:1), and diluted it with a pRSETb bacterial expression vector (1:100). We transfected in HEK293T (containing large T antigen which can facilitate replication of mammalian expression vectors with an SV40 ori) but found the expression/brightness to be too low in most cells. In order to optimize, we transferred the cells to 33°C in order to slow the growth for 96hrs post transfection without impairing the protein expression. We then assessed the nuclear fluorescence and found approximately 65% of cells were nonfluorescent while about 20% were either yellow or red, divided in a 1:1 ratio, meaning that those single-color cells received/expressed primarily one tagged FP over the other (Figure 4.12a,b). Potential follow-up could include an antibiotic selection to enrich for cells with library variants. The separation of the fluorescent population and relatively high transfection efficiency/expression demonstrates the utility of performing a sparse transfection for sensor screening. To address the second hurdle, an alternative strategy for enriching a library, if the SNR of the desired variants relative to the entire library precludes selection, might encompass choosing and re-sorting several subsamples post stimulation within a range of normalized brightness. Additionally, if the cell-to-cell response variability muddles the ability to identify hits or a re-sort is impractical, fusing either a catalytically-active or inactive kinase to the sensor library might capture the sensor in either the high or low reporting states. Performing a single sort, collecting cells at normalized brightness extrema, and deep sequencing to find the overlapping sensor variants might embody a high-throughput screening approach. FACS-based screening methods hold promise for expanding the biosensor toolset and catapulting current efforts in the lab, specifically including optimizing single-color red sensors as well as unique photoconvertible reporters of second messengers.

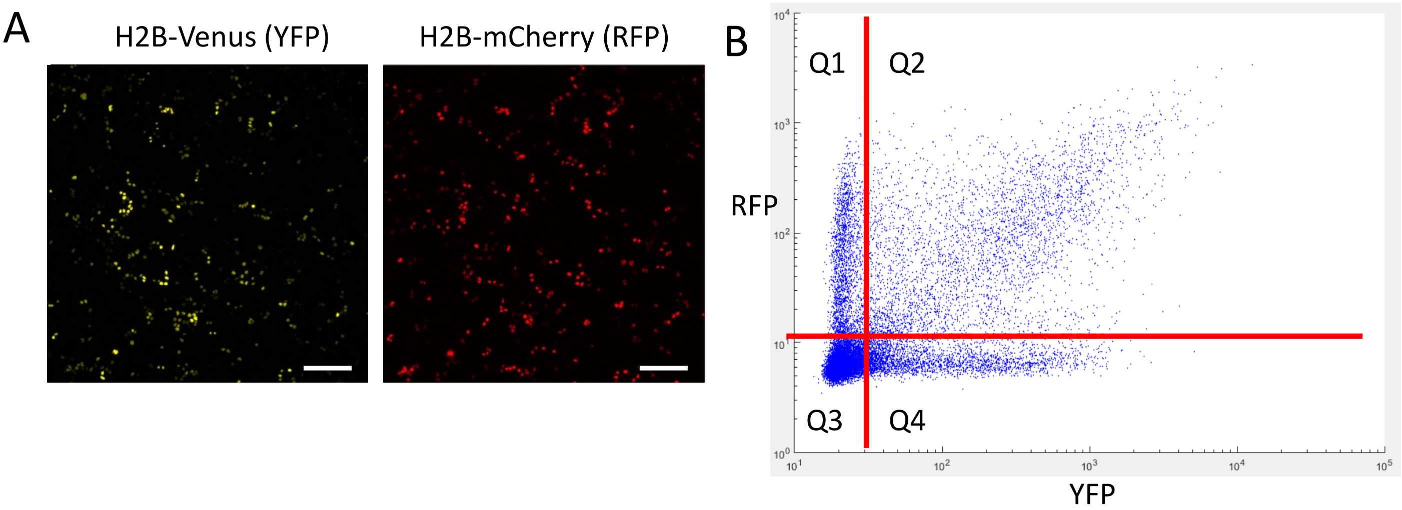

Figure 4.12 Sparse transfection testing in HEK293T. (A) Images of HEK293T cells sparsely transfected with nuclear-targeted Venus and mCherry (scale 250um). (B) Quantification of yellow and red fluorescence intensity for each cell in A. Q1: single red cells, Q2: both red and yellow (both constructs expressed), Q3: non-fluorescent cells, Q4: single yellow cells.

Conclusion

Complex biochemical processes shape the intricate signaling networks essential for life. Genetically-encoded biosensors capable of multiplexed imaging allow simultaneous reporting of many of these “molecular conversations” within individual cells. This information is indispensable in helping unravel the complicated interplay between signaling pathways. Here we highlighted two new families of sensors with suitable multiplexing properties. FLAREs are single-color, ratiometric probes for monitoring enzymatic activity or second messenger concentration. The sensors rely on changes in homoFRET, and the modular design facilitates development of color variants and sensors for other targets. The ExRai sensors are single-FP, excitation-ratiometric probes that detect biochemical processes through modulation of the electronic environment of a genetically-encoded fluorophore. Designing and optimizing biosensors, especially the single-FP family of sensors, can be difficult and time-consuming due to an inability to accurately predict molecular states and sensor responses. Thus, we designed and described a few screening platforms to rapidly assess and select changes to the single-FP sensors. Using these methodologies, we optimized ExRai-AKAR, a blueAKAR, and finally a greenAKAR. These screening platforms will likely continue to help design and develop better biosensors for multiplexed signaling interrogation.

Materials and Methods

Gene Construction

Color variants of the FLAREs were created by replacing the genes for the fluorescent proteins in other FLARE AKAR variants in pRSET-B, either between the BamHI and SphI sites for the N-terminal fluorescent protein, or SacI and EcoRI for C-terminal fluorescent proteins. Finalized constructs intended for mammalian expression were then sub-cloned into a modified pcDNA3 expression vector between the BamHI and EcoRI sites. FLARE variants of other sensors were created by amplifying the molecular switch from EKAR-EV, CKAR2, Cameleon and ICUE3 with primers encoding the SphI and SacI sites, digesting the PCR product with SphI and SacI enzymes, and ligating them to the relevant pRSET-B FLARE AKAR plasmid digested with SphI and SacI to remove the domains involved in the molecular switch for FLARE AKAR. The final constructs were then subcloned into a modified pCDNA3 expression vector between the BamHI and EcoRI sites. Targeted versions of the sensors were created either by PCR amplifying the sensor with primers containing the targeting sequence and ligating it to the pCDNA3 expression vector between BamHI and EcoRI, or by subcloning the construct into a plasmid already containing the targeting sequence. N-terminal targeting sequences were placed between HindIII and EcoRI, and C-terminal targeting sequences between EcoRI and XbaI. All cloning steps were performed using DH5α strain of *E. coli.*

The threonine to alanine mutants for Venus-cp172Venus FLARE AKAR and FLARE EKAR were created by performing site-directed mutagenesis using a standard single-primer PCR-based protocol. The threonine to alanine mutant for Venus-cp172Venus FLARE CKAR was created using Gibson assembly, amplifying the appropriate fragment with a primer containing the desired mutation.

For the ExRai-AKAR optimization, a randomized linker library was created by PCR amplifying cpGFP with flanking $(NNS)_3$ at linker positions for and dropping the insert into a PCR-amplified pRSETb construct already containing the remainder of the biosensor (PKAsub/FHA1). The dual expression construct was created by PCR amplifying the arabinose operon from the pBAD vector and inserting it into the backbone of pRSETb containing ExRai-AKAR2 using Gibson Assembly. The genes for PKAcat (S. Taylor) and mScarlet were then inserted into the pBAD operon using Gibson Assembly. For the dual expression linker library, mScarlet was moved downstream of the ExRai sensor and fused via a rigid linker $(EAAAK)_5$ to prevent FRET. The linker library for screening in the dual expression vector was constructed using PCR amplification, identical to above. For assessing sensor responses in HEK293T cells as well as for FACS, the selected linker variants and ExRai-AKAR2 were cloned into pcDNA3 mammalian expression vector (BamHI/EcoRI).

Cell Culture and Transfection

HEK293T cells were maintained using Dulbecco's Modified Eagle's Medium (DMEM) supplemented with 10% fetal bovine serum (FBS) and 1% penicillin/streptomycin. Cells were seeded onto a 35-mm glass-bottom imaging dish and incubated at 37°C with 5% ambient carbon dioxide. HEK293T and MIN6 cell lines were maintained separately from other cells and were screened regularly to confirm the absence of mycoplasma contamination using Hoechst staining. As the origin of the cells was not central to the nature of these experiments, we did not further validate the identity of the cell lines. Cells were transfected using Lipofectamine 2000

(Invitrogen), Polyjet (SignaGen) and incubated for 12–48 hr before imaging. The growth media was removed immediately before imaging, and the cells were washed two or more times with Hanks Balanced Salt Solution (HBSS) buffer with glucose at room temperature. The cells were imaged in HBSS buffer with glucose at either room temperature or 37°C.

Fluorescence Imaging

Fluorescence Polarization Microscopy

Widefield images were collected using a Zeiss AxioObserver equipped for fluorescence polarization microscopy, using one of two setups. In the first setup, a wire grid polarizer (Meadowlark Optics) was placed in the excitation pathway between the LED illuminators and reflector turret containing filter cubes specific for CFP (Zeiss), YFP (Zeiss), and mCherry (Semrock). Images were generally collected using a 20 × 0.75 NA objective lens. Polarizations parallel and perpendicular to the excitation polarizations were separated using Optical Insights Dual-View using their polarization splitting module. Both images were simultaneously collected in a single image collected by a water-cooled Orca-R2 (Hamamatsu). In the second setup, a polarizer (Chroma) was placed in the excitation pathway between the xenon arclamp and the excitation filters. Images were collected using a 20 × 0.45 NA objective lens. Polarizations were separated using an Opto-Split II LS image splitter, with two wire grid polarizers (Meadowlark) oriented parallel and perpendicular to the excitation polarizer. Images of both polarizations were collected using a Hamamatsu Flash 4.0 sCMOS camera. Two-photon imaging was performed using a Zeiss 7 MP with GaAsP non-descanned detectors housed at the University of Maryland School of Medicine confocal facility. Coherent Chameleon and OPO lasers were used for excitation. Fluorescence was filtered using an ET680 short pass filter for two-photon microscopy

(Chroma) prior to separating polarizations with a one inch broadband polarizing beamsplitter cube (Thorlabs) mounted using a custom 3D printed cube. Images were collected using a 10×, 0.3 NA Plan-apochromat objective lens. In vivo imaging was performed on C57Bl/6 mice under isoflurane anesthesia.

Epifluorescence Imaging

Cells were washed twice with Hank's balanced salt solution (HBSS, Gibco) and subsequently imaged in HBSS in the dark at 37°C. Images were acquired on a Zeiss AxioObserver Z1 microscope (Carl Zeiss) equipped with a 40x/1.3 NA objective and a Photometrics Evolve 512 EMCCD (Photometrics, Tucson, AZ) controlled by METAFLUOR 7.7 software (Molecular Devices). Dual GFP excitation ratio imaging was performed using a 480DF30 excitation filter and 505DRLP dichroic mirror, a 380DF10 excitation filter and 450DRLP dichroic mirror, and a 535DF45 emission filter; BFP intensity was imaged using a 380DF10 excitation filter, a 450DRLP dichroic mirror, and a 475DF40 emission filter; RFP intensity was imaged using a 568DF55 excitation filter, a 600DRLP dichroic mirror, and a 653DF95 emission filter; YFP intensity was imaged using a 495DF40 excitation filter, a 515DRLP dichroic mirror, and a 535DF25 emission filter. All filter sets were alternated by a Lambda 10–2 filter-changer (Sutter Instruments). Exposure times ranged between 50 and 500 ms and images were acquired every 15–30 s.

Image Analysis

Polarization Imaging

Image analysis was performed using Fiji (ImageJ) open-source image processing software. Polarization images were cropped and aligned using either the Zeiss Axiovision software or Fiji's built-in StackReg registration plugin. In Fiji, regions of interest (ROIs) were drawn around each cell, as well as one in the background. ROI intensities were background subtracted in each channel to estimate fluorescence emission intensity, and anisotropy was calculated as described (Lakowicz 2006). Anisotropies were calculated using the conventional equation:

$$r = (P - gS) / (P + 2gS)$$

where g is the correction factor that accounts for differences in polarization transmission efficiencies within the instrument. The g-factor was calculated using an isotropic fluorescein solution as described (Piston et al. 2008). Delta anisotropy was calculated by subtracting the anisotropy at each time point by the anisotropy at the time point right before drug addition. The magnitude of the anisotropy changes were calculated by taking the difference between the average anisotropy when the signal peaked or plateaued and the average anisotropy of the baseline time points before drug was added.

Epifluorescence Imaging

Raw fluorescence images were corrected by subtracting the background fluorescence intensity of a cell-free region from the emission intensities of biosensor-expressing cells. GFP excitation ratios (F480/F380) were then calculated at each time point. The resulting time-courses were normalized by dividing the ratio or intensity at each time point by the basal value at time zero (e.g., F/F_0 or R/R_0), which was defined as the time point immediately preceding drug addition. Analysis was performed in MATLAB. Graphs were plotted using GraphPad Prism 5 (GraphPad Software).

Linker Screening

Linker libraries were transformed into BL21 E.coli and plated on LB agar plates supplemented with ampicillin and glucose (20mM). Fluorescence from the bacterial colonies were measured using a broad-spectrum lamp source (MAX-303, Asahi Spectra) with excitation filters and monitored by a Thorlabs USB digital camera mounted behind a Thorlabs emission filter wheel. The images were analyzed using ImageJ (v. 1.47g). For the lysate screen, pellets in 96 well plates were lysed (B-PER, ThermoFisher) and fluorescence was monitored with Tecan Spark20M plate-reader. Purified PKAcat (gift from S. Taylor) (21ug/ml) and ATP (100uM) was added to the lysates to assess biosensor response. For the dual expression platform, 1M arabinose was sprayed onto the plates and incubated at 37C. Excitation spectra of clarified lysate was measured on a fluorimeter (Horiba). For FACS, a BD Influx was used (Sanford Consortium Embryonic Stem Cell Core).

References

Akerboom, J. et al. (2013). “Genetically encoded calcium indicators for multi-color neural activity imaging and combination with optogenetics.” Front. Mol. Neurosci. 6:2.

Branon, TC. et al. (2018). “Efficient proximity labeling in living cells and organisms with TurboID.” Nat Biotechnol. **36**(9): 880-887.

Chen, T. et al. (2013). “Ultrasensitive fluorescent proteins for imaging neuronal activity.” Nature. **499**: 295-300.

Chen, X. et al. (2014). “Fusion Protein Linkers: Property, Design and Functionality.” Adv Drug Deliv Rev. **65**(10): 1357-1369.

Cohen, R. et al. (2010). “Quantification of Plasmid DNA Copies in the Nucleus after Lipoplex and Polyplex Transfection.” J Control Release. **135**(2): 166-174.

Cormack, BP. et al. (1996). “FACS-optimized mutants of the green fluorescent protein (GFP).” Gene. **173**(1): 33-38.

Depry, C. et al. (2011). “Visualization of PKA activity in plasma membrane microdomains.” Mol Biosyst. **7**(1): 52-8.

Ibraheem, A. et al. (2011). “A bacteria colony-based screen for optimal linker combinations in genetically encoded biosensors.” BMC Biotechnol. 11: 105.

Jung, G. et al. (2005). “The Photophysics of Green Fluorescent Protein: Influence of the Key Amino Acids at Positions 65, 203, and 222.” Biophys J. **88**(3): 1932-1947.

Lakowicz, J. (2006). Principles of Fluorescence Spectroscopy.

Liu, Z. et al. (2017). “Systematic comparison of 2A peptides for cloning multi-genes in a polycistronic vector.” Scientific Reports. **7**:2193.

Mehta, S. et al. (2011). “Reporting from the Field: Genetically Encoded Fluorescent Reporters Uncover Signaling Dynamics in Living Biological Systems.” Annual Review of Biochemistry. **80**:375-401.

Mehta, S. et al. (2018). “Single-fluorophore Biosensors for Sensitive and Multiplexed Detection of Signaling Activities.” Nat Cell Biol. **20**(10): 1215-1225.

Nagai, T. et al. (2004). “Expanded dynamic range of fluorescent indicators for Ca^{2+} by circularly permuted yellow fluorescent proteins.” PNAS. **101**(29): 10554-10559.

Ni, Q. et al. (2011) “Signaling Diversity of PKA Achieved Bia a Ca^{2+}-cAMP-PKA Oscillatory Circuit.” Nat Chem Biol. **7**(1): 34-40.

Piatkevich, K. et al. (2018). “A robotic multidimensional directed evolution approach applied to fluorescent voltage reporters.” Nat Chem Biol. **14**(4): 352-360.

Piston, DW. et al. (2008). “FRET by fluorescence polarization microscopy.” Methods Cell Biol. **85**: 415-30.

Ross, BL. et al. (2018). “Single-color, ratiometric biosensors for detecting signaling activities in live cells.” eLife. 7:e35458.

Tian, L. et al. (2010). “Imaging neural activity in worms, flies and mice with improved GCaMP calcium indicators.” Nature Methods. **6**(12): 875-881.

Tsien, RY. (1998). “THE GREEN FLUORESCENT PROTEIN.” Annual Review of Biochemistry. **67**: 509-544.

Violin, J. et al. (2007). “Beta2-Adrenergic Receptor Signaling and Desensitization Elucided by Quantitative Modeling of Real Time cAMP Dynamics.” JBC. 283: 2949-2961.

Violin, JD. et al. (2003). “A genetically encoded fluorescent reporter reveals oscillatory phosphorylation by protein kinase C.” J Cell Biol. **161**(5): 899-909.

Chapter 5

Conclusions and Future Perspectives

Conclusions and Future Perspectives

Cellular signaling networks are spatiotemporally organized and feature a high degree of connectivity between many different biochemical pathways. Genetically encoded biosensors have been instrumental in helping researchers probe this organizational regulation. In this dissertation, we highlighted the utility of these reporters by employing them to study compartmentalized signaling as well as multiple signals within the same reference frame. Using a cAMP biosensor fused to a scaffold protein, we uncovered a novel mode of compartmentalized regulation within the Ca^{2+}-cAMP-PKA oscillatory circuit in pancreatic beta cells. We then extended the fusion-based approach for studying signaling microdomains by developing a suite of FRET-based biosensors that are amenable for monitoring endogenous compartments. Finally, we unveiled a new set of sensors that are suitable for multiplexed interrogation of multiple signaling pathways within the same live cell.

Within the biosensor field, future progress will most likely include the design and optimization of better, more robust reporters. For example, screening and development of sensors with enhanced sensitivity and that use longer wavelengths have allowed researchers to deploy these tools in vivo and observe single-cell activity within an organism (Piatkevich et al. 2018; Qian et al. 2019). Further progress will also include the development of more sensors that incorporate additional information into their output. For example, the innovative biosensor CaMPARI works as a coincidence detector and photoconverts from a green fluorescent state to a red fluorescent state only in the presence of both Ca^{2+} and UV light, and thus allows researchers to highlight active neural circuits during behavior (Fosque et al. 2015). Also, sensors that report biochemical activity in a format adaptable for super-resolution imaging has granted researchers a unique glimpse into a cell's nanoscale signaling architecture (Mo et al. 2017). Expanding the repertoire of these, and other sensors, and iteratively improving them will continue to advance our understanding of signaling networks.

Despite the advantages fluorescent protein-based biosensors have for monitoring biological activity in single cells, some areas of application remain currently out of reach. For example, enhancing our understanding of the connection between the brain and behavior requires knowledge of neuronal wiring and recording the activity of intact neural circuits in real-time. Although advances in microscopy, improved genetically encoded voltage and Ca^{2+} biosensors, and revolutionary techniques in genetic manipulation have spearheaded progress in this arena in the last decade, we are still only able to optically excite and monitor an extremely small subset of neurons from a complex organism's brain at a given time. Thus, future work focusing on "scaling-up" single-cell biosensors for an entire-brain/whole-organism recording might instead rely on a different informational medium than light, such as DNA or RNA (Farzadfard et al. 2018; Sheth et al. 2018).

Nevertheless, genetically encoded biosensors have revolutionized our knowledge of cell signaling and spatiotemporal organization by allowing researchers a privileged view of biochemical communication inside individual, living cells. The future of these biosensors and their applications is bright.

References

Farzadfard, F. et al. (2018). “Emerging applications for DNA writers and molecular recorders.” Science. **361**(6405): 870-875.

Fosque, BF. et al. (2015). “Neural circuits. Labeling of active neural circuits in vivo with designed calcium integrators.” Science. **347**(6223): 755-60.

Mo, GC. et al. (2017). “Genetically encoded biosensors for visualizing live-cell biochemical activity at super-resolution.” Nat Methods. **14**(4): 427-434.

Piatkevich, K. et al. (2018). “A robotic multidimensional directed evolution approach applied to fluorescent voltage reporters.” Nat Chem Biol. **14**(4): 352-360.

Qian, Y. et al. (2019). “A Genetically encoded near-infrared fluorescent calcium ion indicator.” Nat Methods. **16**(2): 171-174.

Sheth, R. et al. (2018). “DNA-based memory devices for recording cellular events.” Nature Reviews Genetics. **19**: 718-732.

Brian J. Tenner

EDUCATION

Sep. 2012 – present	**Ph.D. Molecular Biophysics**, Johns Hopkins School of Medicine (expected graduation May 2019)
Sep. 2008 – May 2012	**B.S. Biochemistry; B.S. Mathematics,** Southern Methodist University

RESEARCH EXPERIENCE

June 2013 – present	**Doctoral Candidate,** Probing spatially compartmentalized signaling circuits in pancreatic beta cells; Characterizing and optimizing single-color biosensors for multiplexed signal interrogation *with Dr. Jin Zhang, Johns Hopkins School of Medicine, Baltimore, MD*
Sep. 2015 – present	**Visiting Graduate Student,** Completing thesis research; relocated with lab *with Dr. Jin Zhang, University of California San Diego, San Diego, CA*
May 2012 – June 2013	**Rotating Graduate Student,** Characterized ribosome subassembly; Utilized super-resolution to study genetic switches; Built stochastic models to describe E.coli metabolism; Examined epimerization reactions of NRPS using NMR *with Drs. Sarah Woodson, Jie Xiao, Elijah Roberts, Dominique Frueh, Johns Hopkins University, Baltimore, MD*
Dec. 2010 – May 2012	**Undergraduate Researcher,** Investigated spatial instabilities in reaction-diffusive processes using random walk models *with Werner Horsthemke, PhD, Southern Methodist University, Dallas, TX*
June 2011 – Aug. 2011	**Summer Researcher,** Analyzed ion pair stability in proteins and ligand binding using ^{19}F NMR *with Dr. Jannette Carey, Princeton University, Princeton, NJ*
June 2010 – July 2010	**Summer Researcher,** Found DNA sequence variants in patients presenting severe diabetic ketoacidosis using SNP assays and NGS *with Dr. Michael Metzker, Baylor College of Medicine, Houston, TX*
Aug. 2009 – Dec. 2010	**Undergraduate Researcher,** Synthesized antibiotic precursors using novel reaction microwave technology *with Dr. Edward Biehl, Southern Methodist University, Dallas, TX*

AWARDS

Carlson Biophysics Graduate Fellowship

Zhang Lab Annual Design Contest 2017, 2018

SMU President's Scholar (full tuition)

SMU Honor Roll with Distinction 2008-2012

SMU Organic Chemistry Award ACS

SMU Inorganic Chemistry Award

TEACHING/WORK EXPERIENCE

2015 - present	**Mentor,** Mentored and trained undergraduates, technicians, rotation students, and graduate student colleagues in the Zhang Lab, UCSD
2014	**Teaching Assistant,** Methods in Biophysics: Graduate Level, JHU
2008 – 2012	**Private Tutor,** Mathematics, Biology, Chemistry, and Physics, SMU
2009 – 2010	**Teaching Assistant,** Organic Chemistry Lab, SMU
2009 – 2010	**Math and Science Tutor,** Altshuler Learning Enhancement Center, SMU

SKILLS/TECHNIQUES

Microscopy	Widefield, Confocal, TIRF, STORM/PALM, SOFI, FRET, Home-built plate screening
Other Instrumentation	FACS, NMR, GC/MS, IR
Molecular Biology	Molecular cloning (Gibson), CRISPR, PLA, ELISA, Cell Culture, Protein purification, qPCR, co-IP, Western
Software/Analysis/Lang.	MATLAB, Python, Metamorph, ImageJ/FIJI, PyMOL, NIS Elements, Snapgene, GraphPad PRISM, Swift – Apple Developer, Eagle CAD, SQL, Java, LaTeX, Gaussian09, Mathematica, Excel

SELECTED PRESENTATIONS/WORKSHOPS

Dec. 2017	Pharmacology Rounds, "Elucidating the Spatial Compartmentalization of cAMP/PKA Using Novel Biosensors," *University of California San Diego, San Diego, CA*
Feb. 2017	Biophysical Society Annual Meeting, "Monitoring Endogenous Signaling Microdomains Using a Novel Split Fluorescent Protein Biosensor Approach," *New Orleans, LA*
Oct. 2016	UCSD Biomedical Sciences Research Class, "A Primer on Proximity Biotinylation," *University of California San Diego, San Diego, CA*

May 2015	Pharmacology Research in Progress, "Investigating the Spatiotemporal Organization of the PKA-cAMP-Ca^{2+} Circuit by the AKAP79/150 Scaffold in MIN6 Beta Cells," *Johns Hopkins School of Medicine, Baltimore, MD*
Sept. 2014	Institute for Biophysical Research Retreat, "Localized Signaling Dynamics on the AKAP79/150 Scaffold in MIN6 Beta Cells," *Johns Hopkins University, Baltimore, MD*
July 2014	Workshop on Single Molecule Methods, Center for the Physics of Living Cells, *Laboratory of Dr. TJ Ha, University of Illinois Urbana-Champaign*
Feb. 2014	Biophysics Seminar Class, "Recognition and Reengineering of TAL Effectors*," Johns Hopkins School of Medicine, Baltimore, MD*

PUBLICATIONS

B. Tenner, M. Getz, B. Ross, S. Mehta, D. Ohadi, P. Rangamani, J. Zhang, Spatially compartmentalized phase regulation in an oscillatory, signaling circuit. *In preparation for submission*

B. Tenner*, JZ. Zhang*, S. Mehta, B. Huang, J. Zhang, FluoSTEPS: Fluorescent Sensors for Targeting Endogenous Proteins. *In preparation for submission*

S. Mehta, Y. Zhang, RH. Roth, JF. Zhang, A. Mo, **B. Tenner**, RL. Huganir, J. Zhang. (2018) Single-fluorophore biosensors for sensitive and multiplexed detection of signalling activities. *Nature Cell Biology*, 20(10), 1215-1225.

BL. Ross, **B. Tenner**, ML. Markwardt, A. Zviman, G. Shi, JP. Kerr, NE. Snell, JJ. McFarland, JR. Mauban, CW. Ward, MA. Rizzo, J. Zhang. (2018) Single-color, ratiometric biosensors for detecting signaling activities in live cells. *Elife*, 7. Pii: e35458.

GC. Mo, B. Ross, F. Hertel, P. Manna, X. Yang, E. Greenwald, C. Booth, AM. Plummer, **B. Tenner**, Z. Chen, Y. Wang, EJ. Kennedy, PA. Cole, KG. Fleming, A. Palmer, R. Jimenez, J. Xiao, P. Dedecker, J. Zhang. (2017) Genetically encoded biosensors for visualizing live-cell biochemical activity at super-resolution. *Nature Methods*, 14(4), 427-434.

B. Tenner, S. Mehta, J. Zhang. (2016) Optical sensors to gain mechanistic insights into signaling assemblies. *Current Opinion Structural Biology*, 41, 203-210.

I. Kishko, B. Harish, V. Zayats, D. Reha, **B. Tenner**, D. Beri, T. Gustavsson, R. Ettrich, J. Carey. (2012) Biphasic kinetic behavior of E. coli WrbA, an FMN-dependent NAD(P)H:quinone oxidoreductase. *PLoS One*, 7(8):e43902.

J. Mahdi, H. Ankati, J. Gregory, **B. Tenner**, ER. Biehl. (2011) Synthesis of (2-Chlorophenyl)(phenyl)methanones and 2-(2-Chlorophenyl)-1-phenylehtanones by Friedel Crafts Acylation of 2-Chlorobenzoic Acids and 2-(2-Chlorophenyl)acetic Acids Using Microwave Heating. *ChemInform*, 42.

*Authors contributed equally.